USGS
science for a changing world

Prepared in cooperation with the U.S. Department of Energy
DOE/ID-22192

Review of the Transport of Selected Radionuclides in the Interim Risk Assessment for the Radioactive Waste Management Complex, Waste Area Group 7 Operable Unit 7-13/14, Idaho National Engineering and Environmental Laboratory, Idaho

Volume II

USGS Scientific Investigations Report 2005-5026

U.S. Department of the Interior
U.S. Geological Survey

Review of the Transport of Selected Radionuclides in the Interim Risk Assessment for the Radioactive Waste Management Complex, Waste Area Group 7 Operable Unit 7-13/14, Idaho National Engineering and Environmental Laboratory, Idaho

Volume 2

By Joseph P. Rousseau, Edward R. Landa, John R. Nimmo, L. DeWayne Cecil, LeRoy L. Knobel, Pierre D. Glynn, Edward M. Kwicklis, Gary P. Curtis, Kenneth G. Stollenwerk, Steven R. Anderson, Roy C. Bartholomay, Clifford R. Bossong, and Brennon R. Orr

---

U.S. GEOLOGICAL SURVEY

Scientific Investigations Report 2005-5026

Prepared in cooperation with the

Idaho Operations Office
U.S. Department of Energy
under Interagency Agreement DE-AI07-97ID13556

Idaho Falls, Idaho
February 2005

U.S. DEPARTMENT OF THE INTERIOR
GALE A. NORTON, Secretary

U.S. GEOLOGICAL SURVEY
CHARLES G. GROAT, Director

Additional information can
be obtained from:
U.S. Geological Survey
INEEL, MS 1160
P.O. Box 2230
Idaho Falls, ID 83403

Copies of this report also
are available in PDF format
which can be viewed using
Adobe Acrobat Reader at URL:

http://pubs.water.usgs.gov/sir20055026

Figures

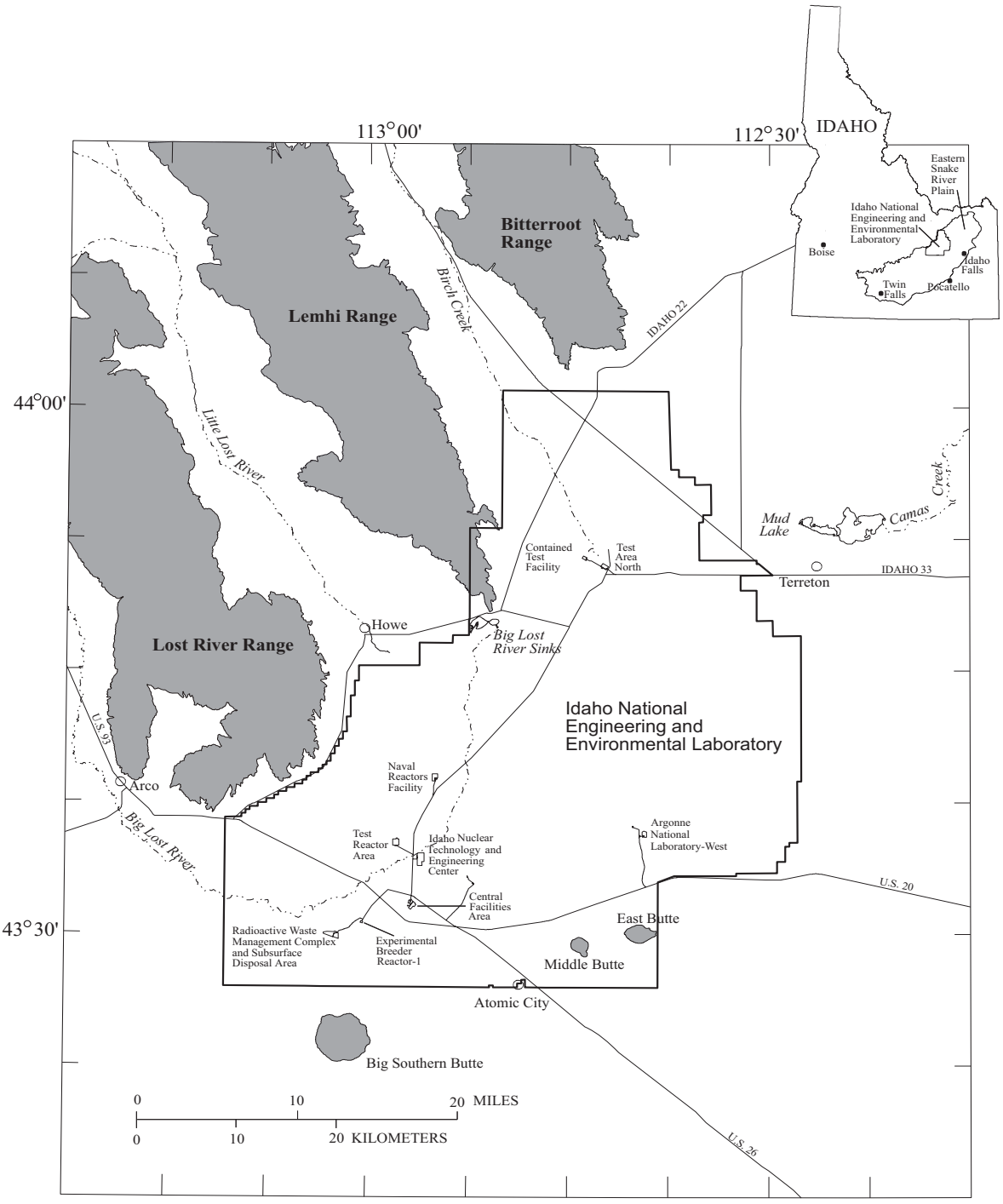

Figure 1-1. Location of the Radioactive Waste Management Complex, Idaho National Engineering and Environmental Laboratory, Idaho

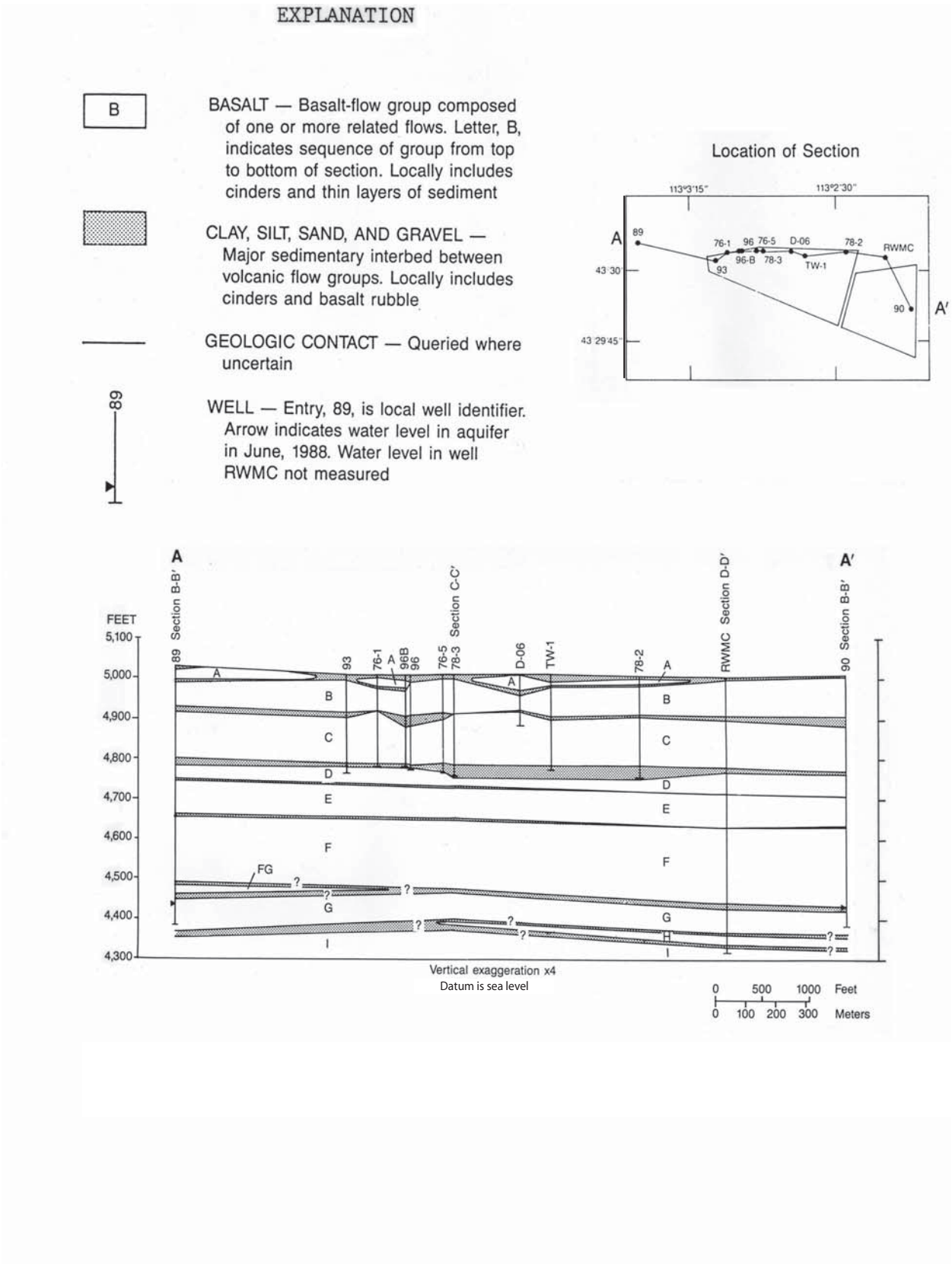

Figure 2-1. Geologic section A-A' at the Radioactive Waste Management Complex, Idaho National Engineering and Environmental Laboratory, Idaho (modified from Anderson and Lewis, 1989, p. 25).

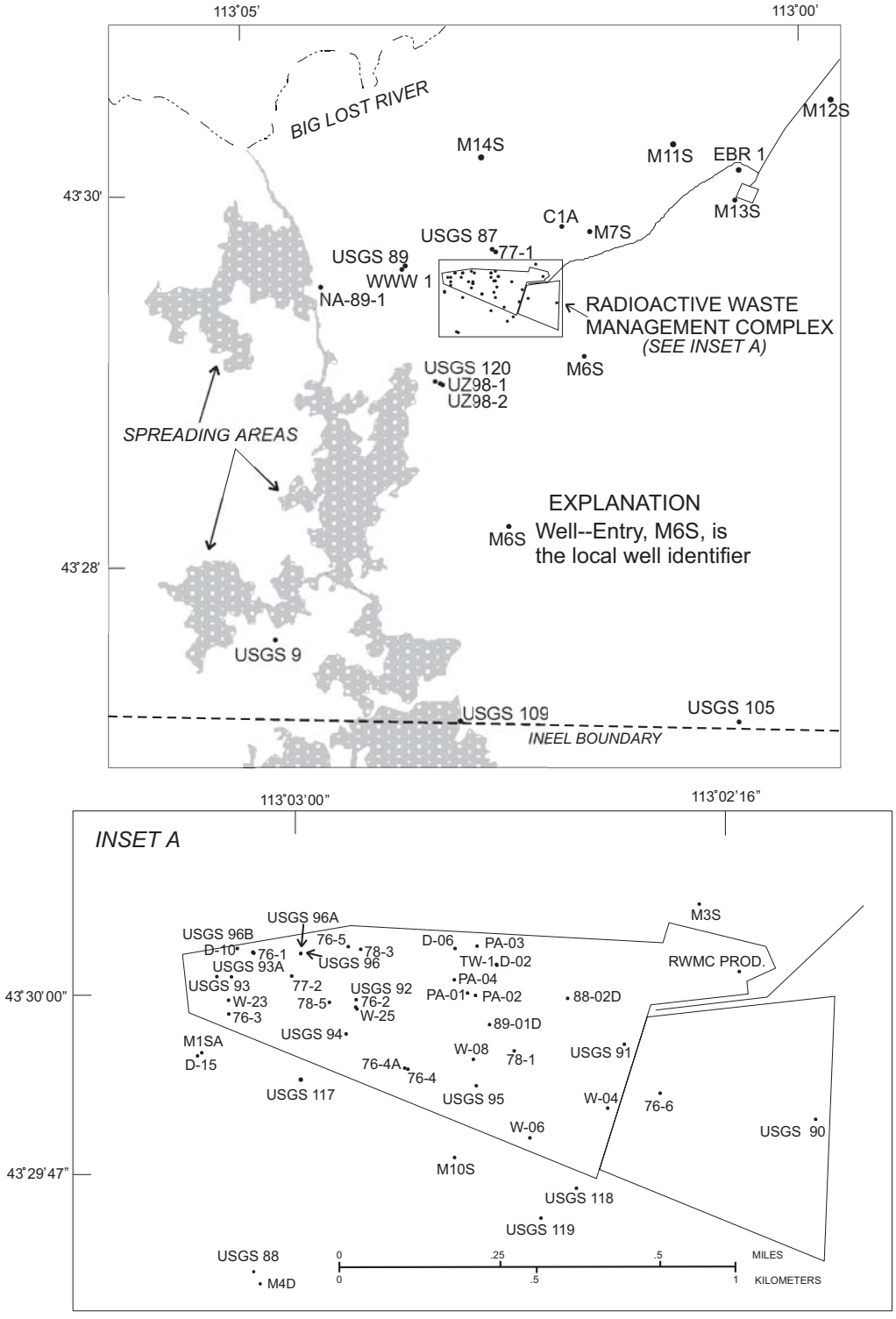

Figure 2-2. Location of sampling sites for the Waste Area Group 7 ground-water monitoring wells, perched-water wells, and lysimeters at and near the Radioactive Waste Management Complex and vicinity, Idaho National Engineering and Environmental Laboratory, Idaho.

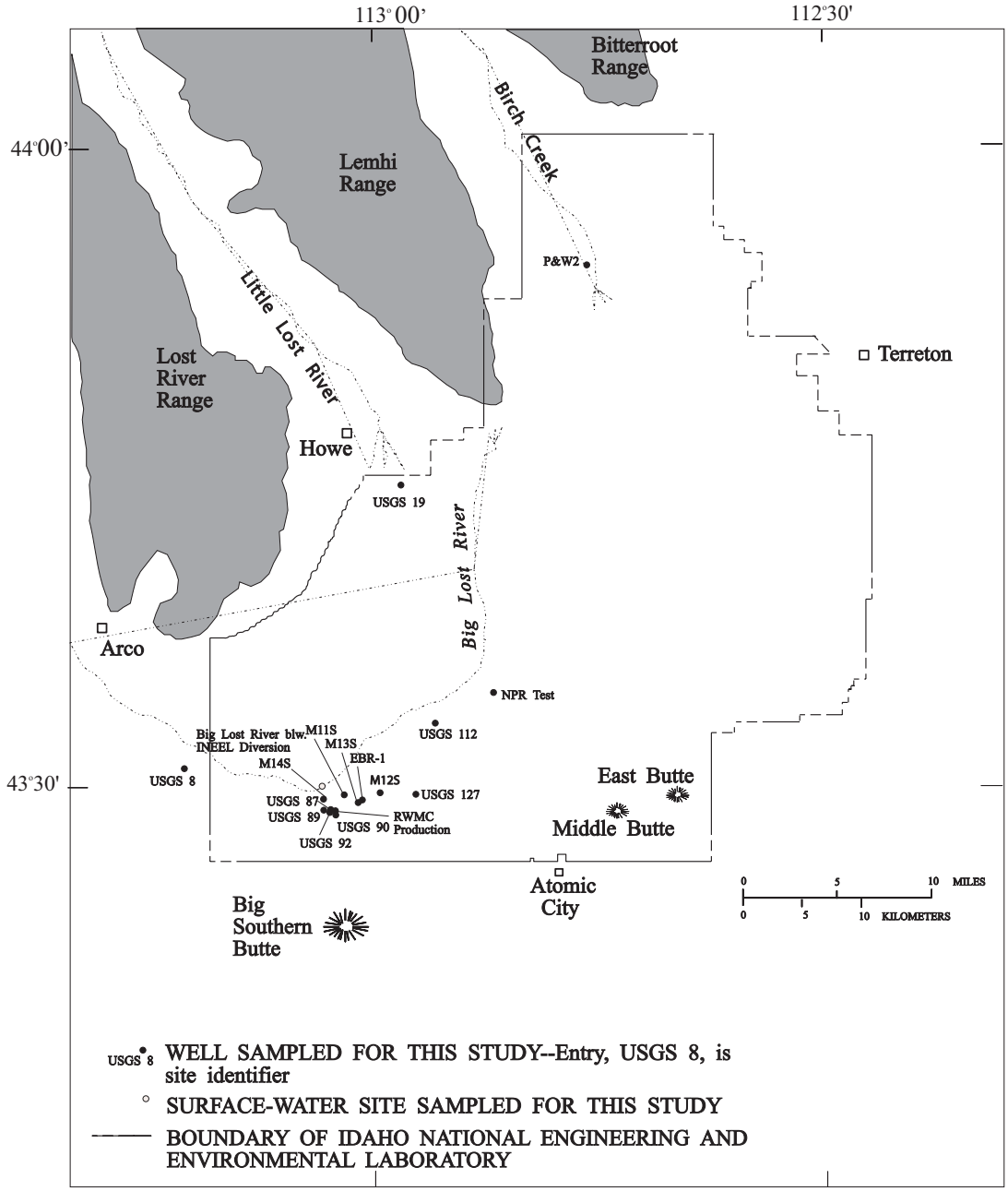

Figure 2-3. Location of selected wells, Idaho National Engineering and Environmental Laboratory and vicinity, Idaho.

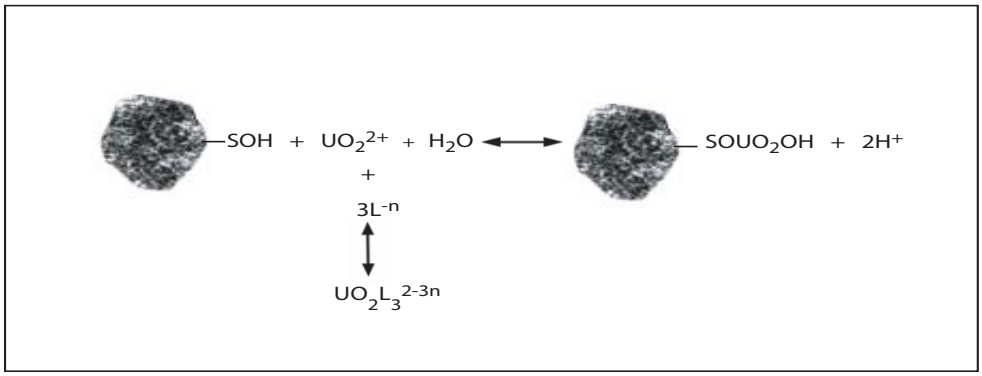

Figure 4-1. Reaction scheme illustrating the competition between the formation of dissolved species (UO_2^{2+} and $UO_2L_3^{2-3n}$) and surface species ($SOUO_2OH$).

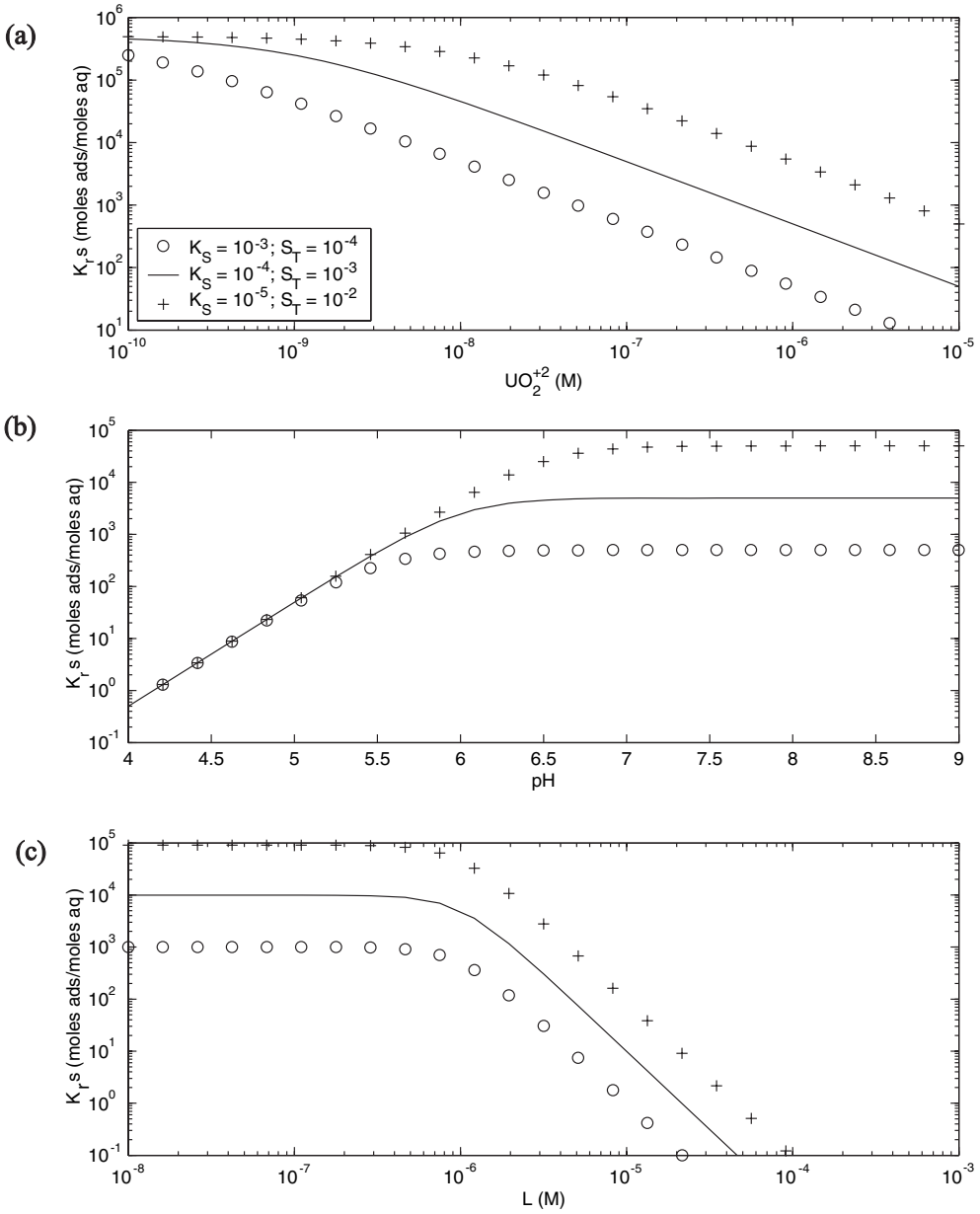

Figure 4-2. Dependence of K_rs on (a) total UO_2^{2+} concentration, (b) pH, and (c) ligand concentration (see text for solution conditions).

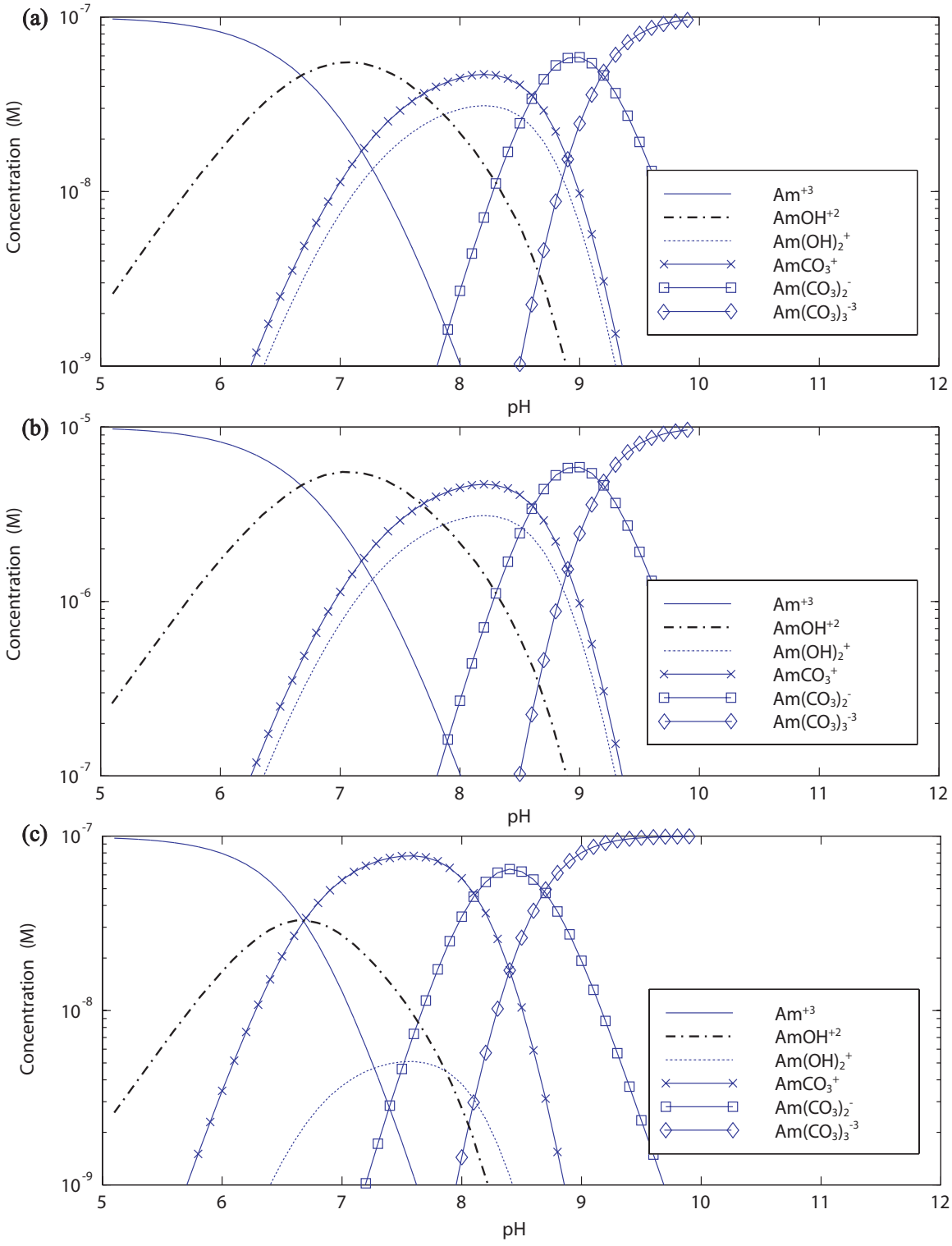

Figure 4-3. Aqueous speciation of Am(III) in the presence of CO_2 for (a) 10^{-7} M Am(III) and $10^{-3.5}$ atm CO_2 (g), (b) 10^{-5} M Am(III) and $10^{-3.5}$ atm CO_2 (g), and (c) 10^{-7} M Am(III) and $10^{-2.5}$ atm CO_2 (g) [M, molarity; g, gas; atm, standard atmosphere].

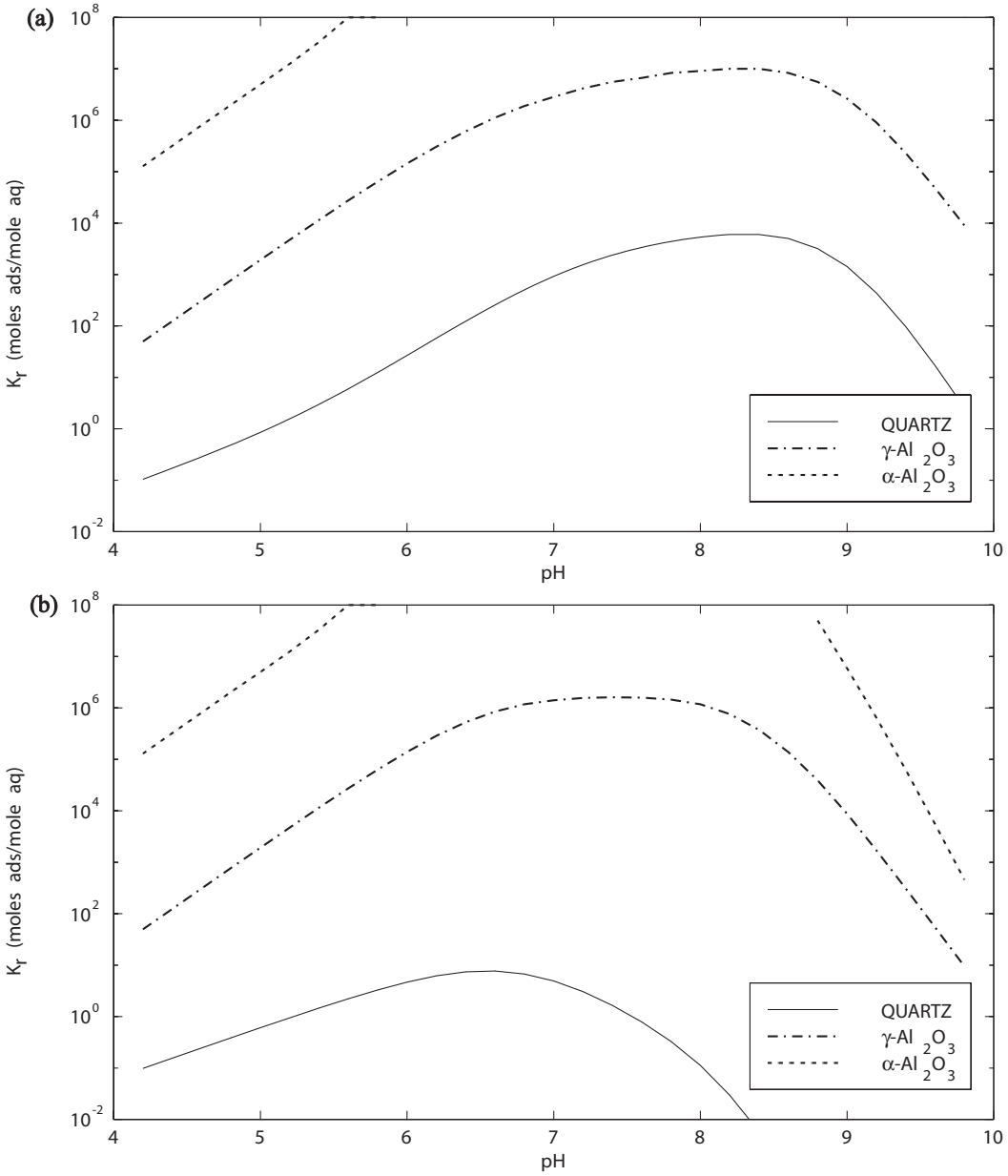

Figure 4-4. Computed surface-area-referenced distribution coefficient (K_r) values for adsorption of Am(III) by quartz, α-alumina, and γ-alumina at (a) $10^{-3.5}$ atm CO_2 (g), and (b) $10^{-2.5}$ atm CO_2(g). Calculated values are based on the surface complexation models described by Turner (1995) [atm, standard atmosphere; g, gas; ads, adsorbed; aq, aqueous].

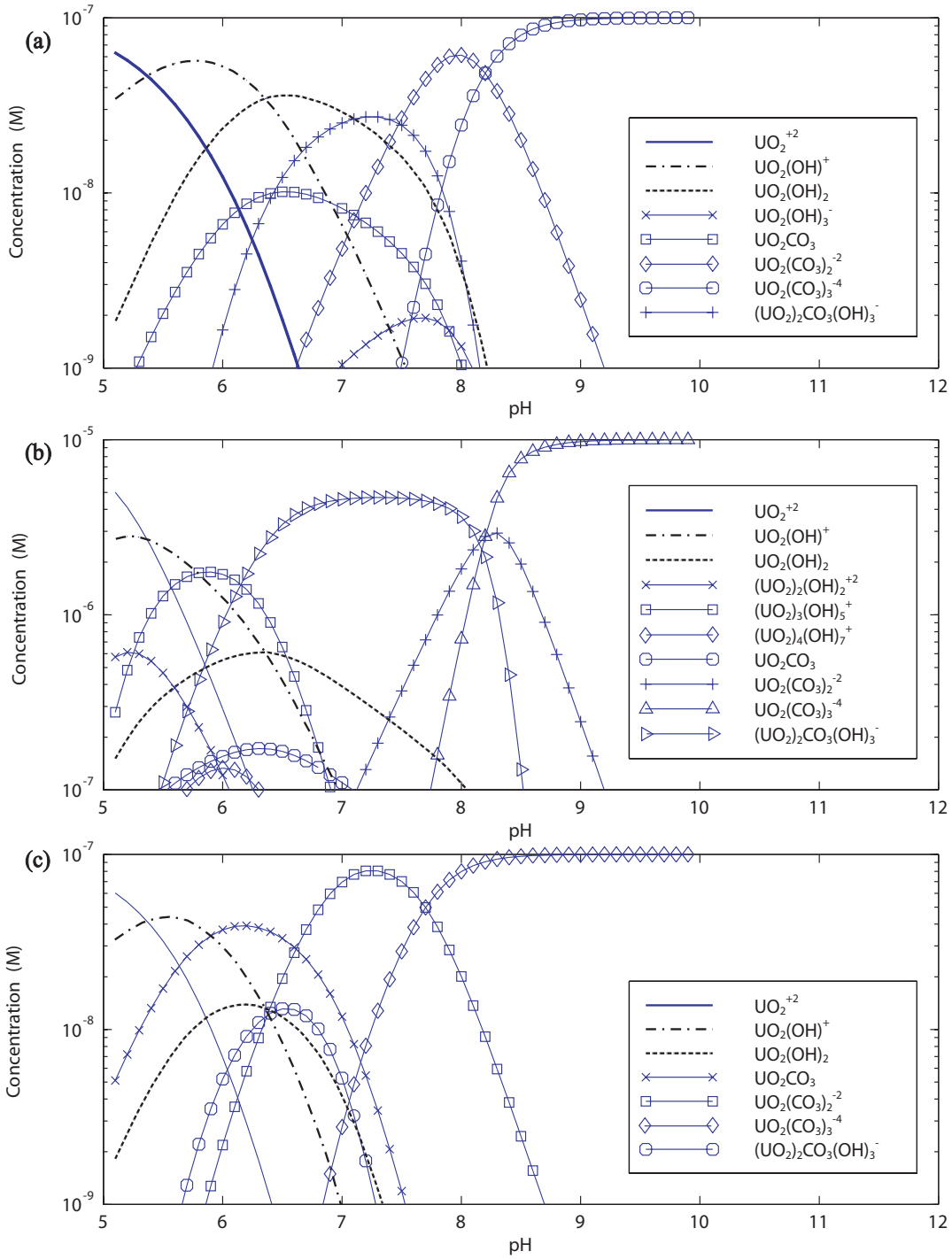

Figure 4-5. Aqueous speciation of U(VI) in the presence of CO_2 for (a) 10^{-7} M U(VI) and $10^{-3.5}$ atm CO_2 (g), (b) 10^{-5} M U(VI) and $10^{-3.5}$ atm CO_2 (g), and (c) 10^{-7} M U(VI) and $10^{-2.5}$ atm CO_2 (g) [M, molarity; g, gas; atm, standard atmosphere].

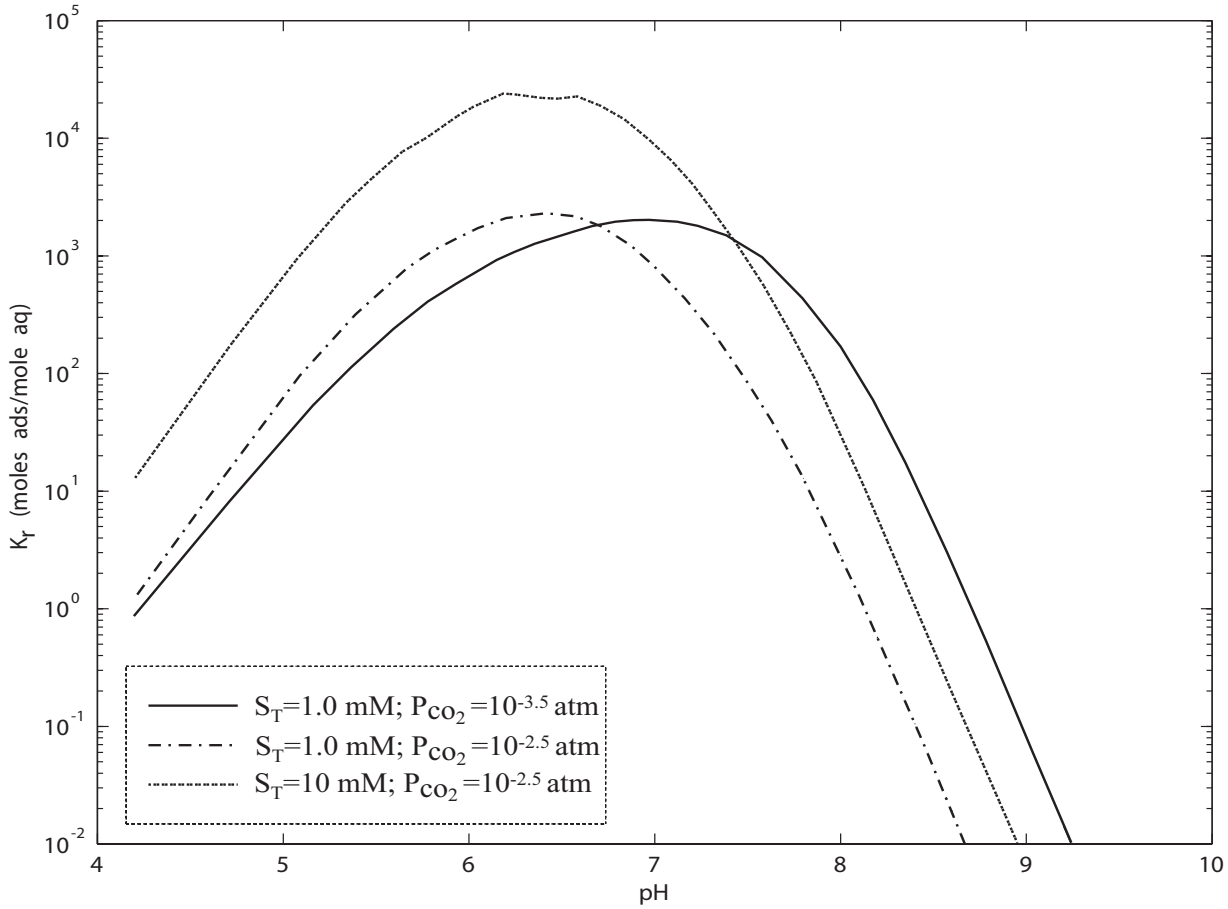

Figure 4-6. Computed surface-area-referenced distribution coefficient (K_r) values for adsorption of U(VI) by ferrihydrite at different partial pressures of CO_2 (g) and total adsorption site density (S_T). Calculated values are based on the surface complexation model for ferrihydrite in table 4-1 [mM, millimole per liter; g, gas; ads, adsorbed; aq, aqueous; atm, standard atmosphere].

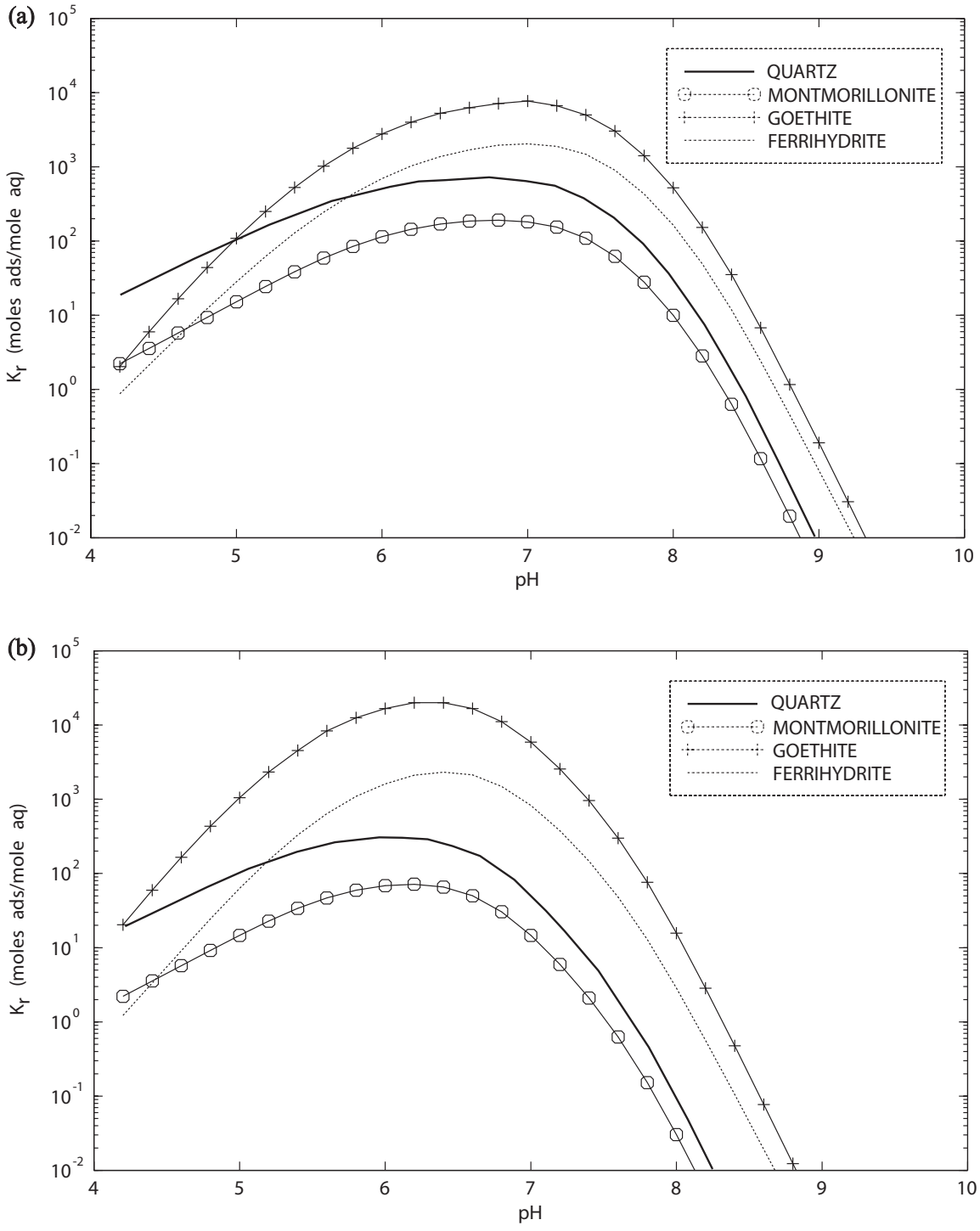

Figure 4-7. Computed surface-area-referenced distribution coefficient (K_r) values for adsorption of U(VI) by quartz, montmorillonite, goethite, and ferrihydrite at (a) $10^{-3.5}$ atm CO_2 (g), and (b) $10^{-2.5}$ atm CO_2 (g). Calculated values are based on the surface complexation models in table 4-1 [atm, standard atmosphere; g, gas; ads, adsorbed; aq, aqueous].

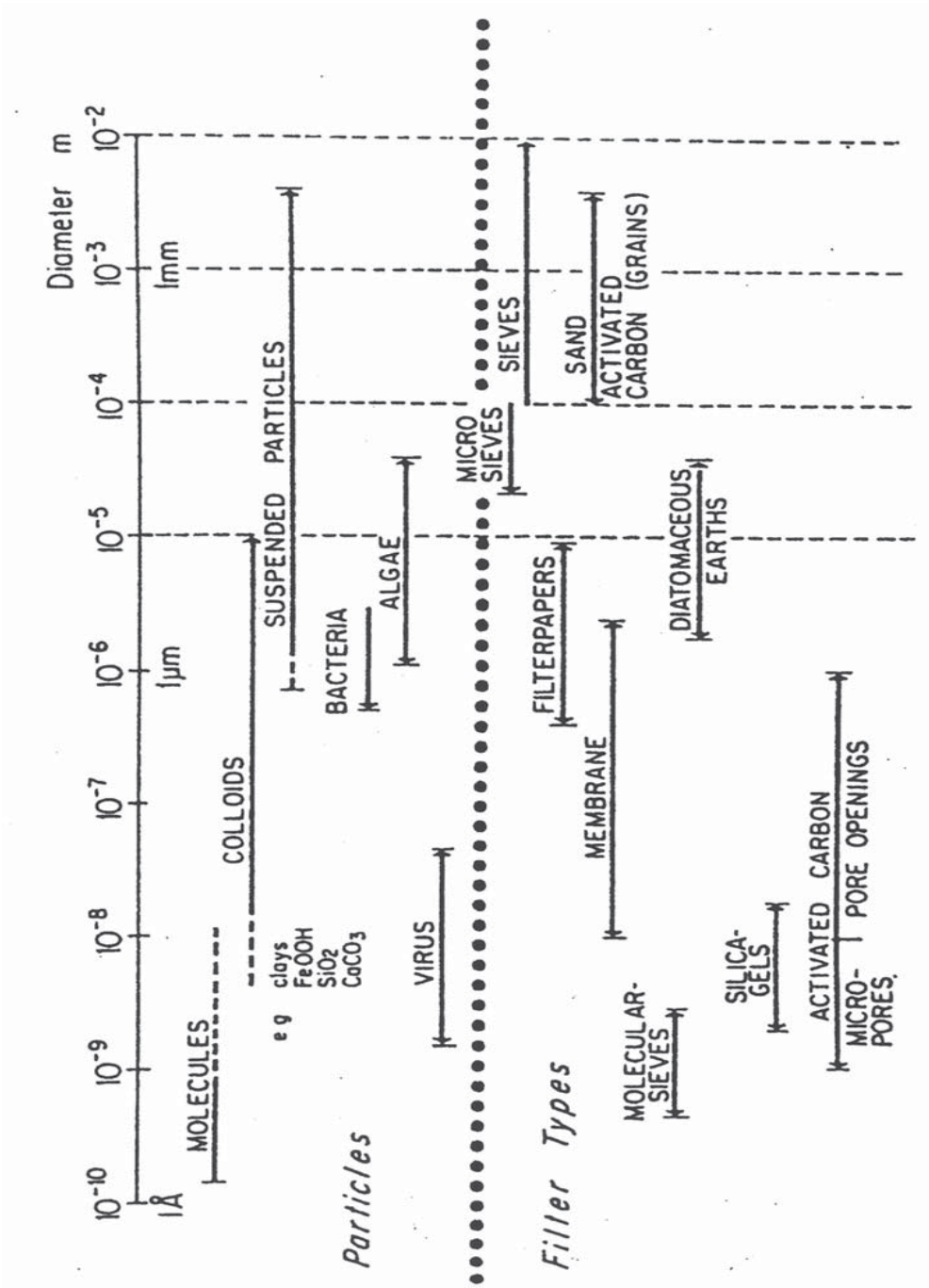

Figure 4-8. Size range of waterborne particles and filter pores (from Stumm and Morgan, 1981).

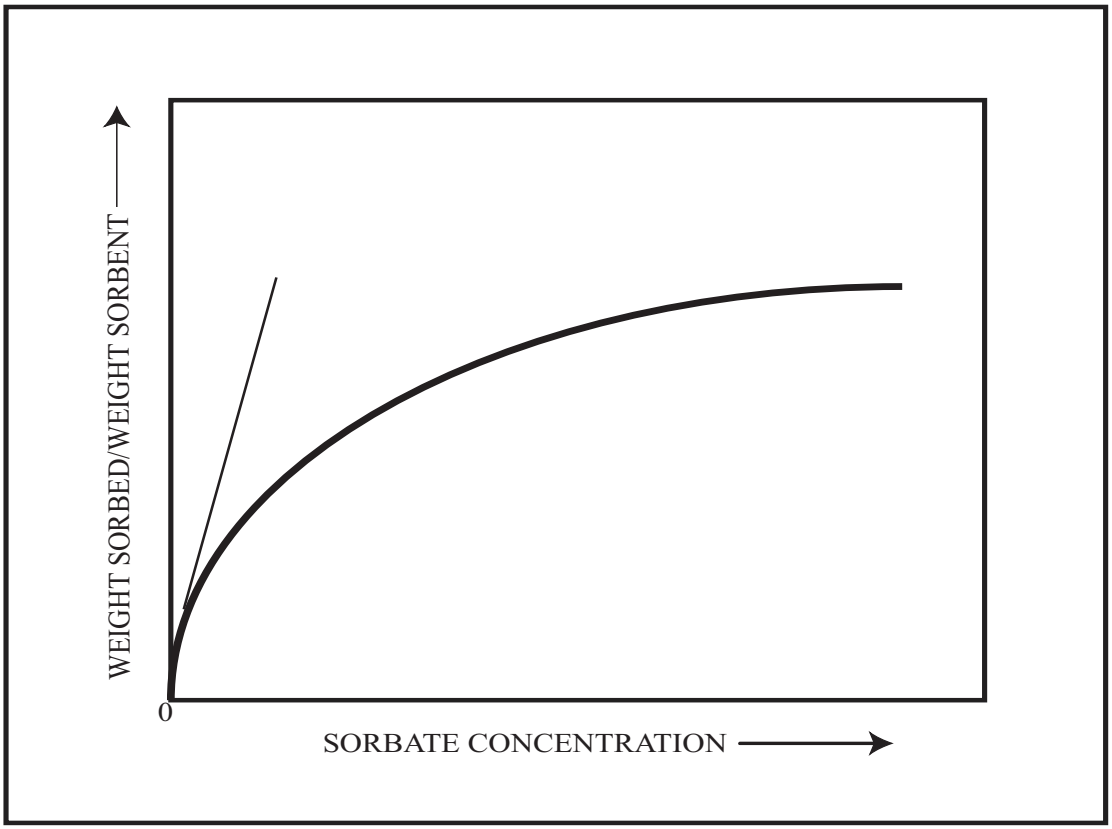

Figure 5-1. The appearance of a typical adsorption isotherm. The slope of the tangent to the isotherm at the origin equals the distribution coefficient, K_d (from Langmuir and Mahoney, 1984).

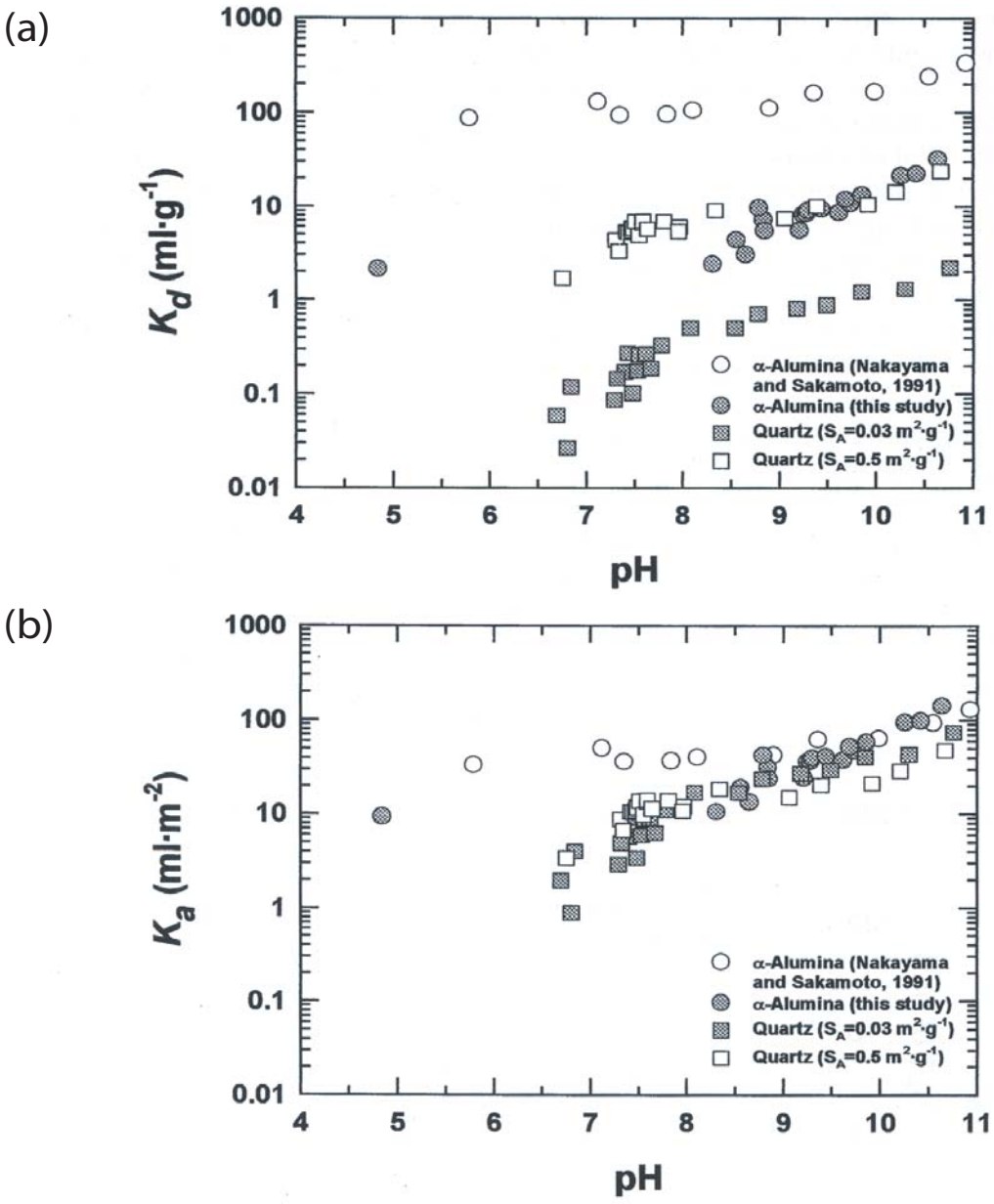

Figure 5-2. The effect of surface area and normalization on Np^{5+} sorption (from Bertetti and others, 1998): (a) K_d data from experiments by Bertetti and others using fine-grained quartz [specific surface area (SA) = 0.5 m^2/g], coarse-grained quartz [0.03 m^2/g], and α-alumina [0.23 m^2/g], and by Nakayama and Sakamoto using finer-grained α-alumina [2.5 m^2/g], and (b) sorption data in graph (a) normalized to the sorbent's specific surface area ($K_a = K_d/SA$) [ml-m^{-2}, milliliter per square meter; ml-g^{-1}, milliliter per gram].

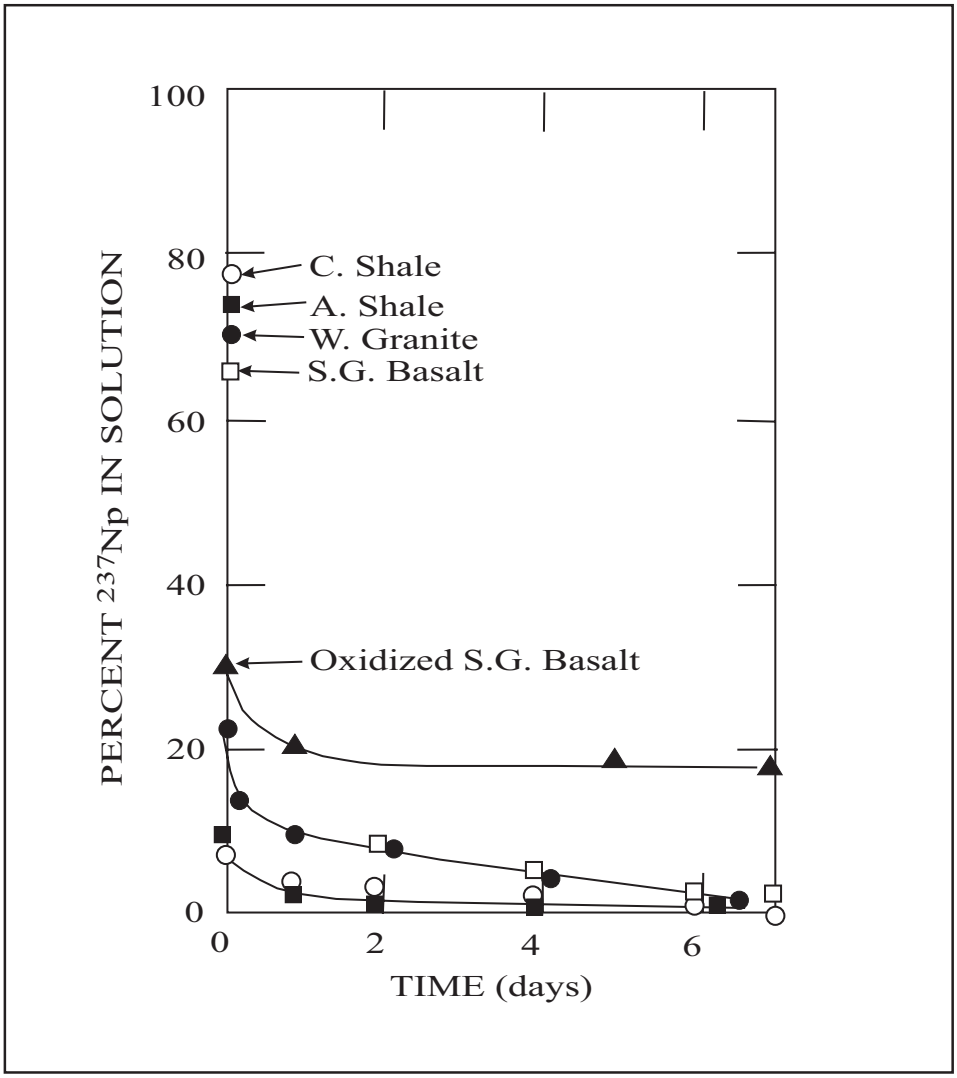

Figure 5-3. Behavior of ^{237}Np (initially NpO_2^+) in rock-water systems. Rocks studied include Conasauga (C.) Shale, argillaceous (A.) shale, Westerly (W.) Granite, Sentinel Gap (S.G.) Basalt, and oxidized S.G. Basalt (pretreated with sodium hypochlorite) (from Bondiette and Francis, 1979).

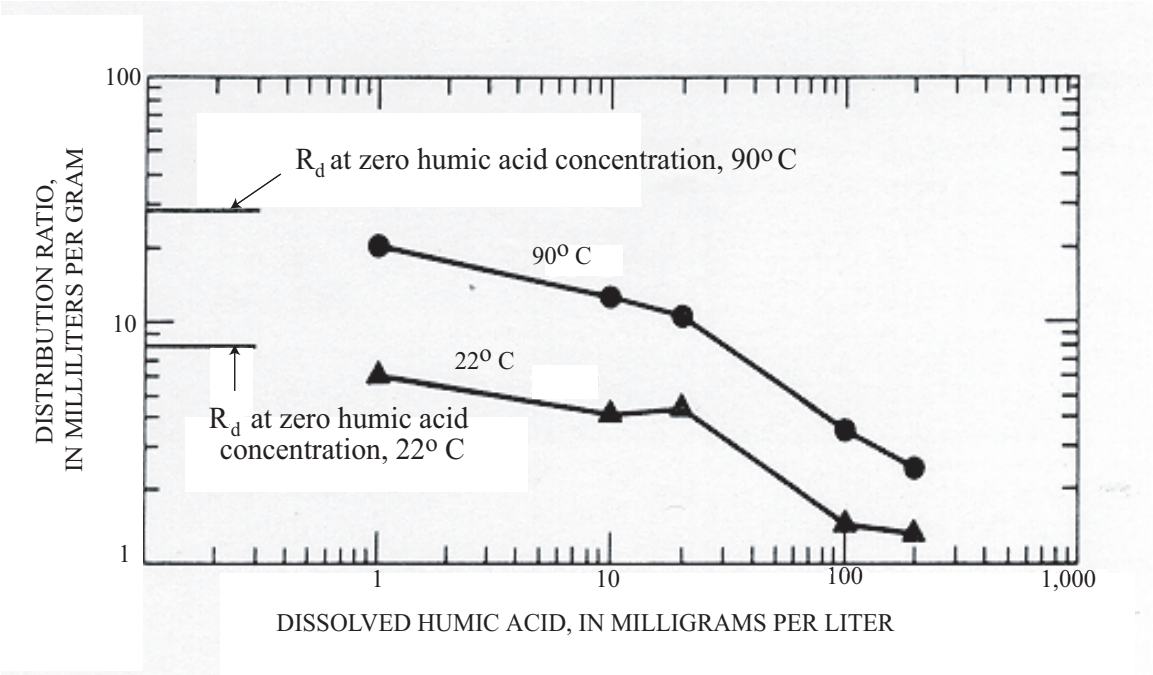

Figure 5-4. Distribution ratio (R_d, equivalent to K_d) for Np sorption onto Pomona Basalt from synthetic ground water in the presence of various concentrations of humic acid (from Boggs and others, 1985) [°C, degrees Celsius].

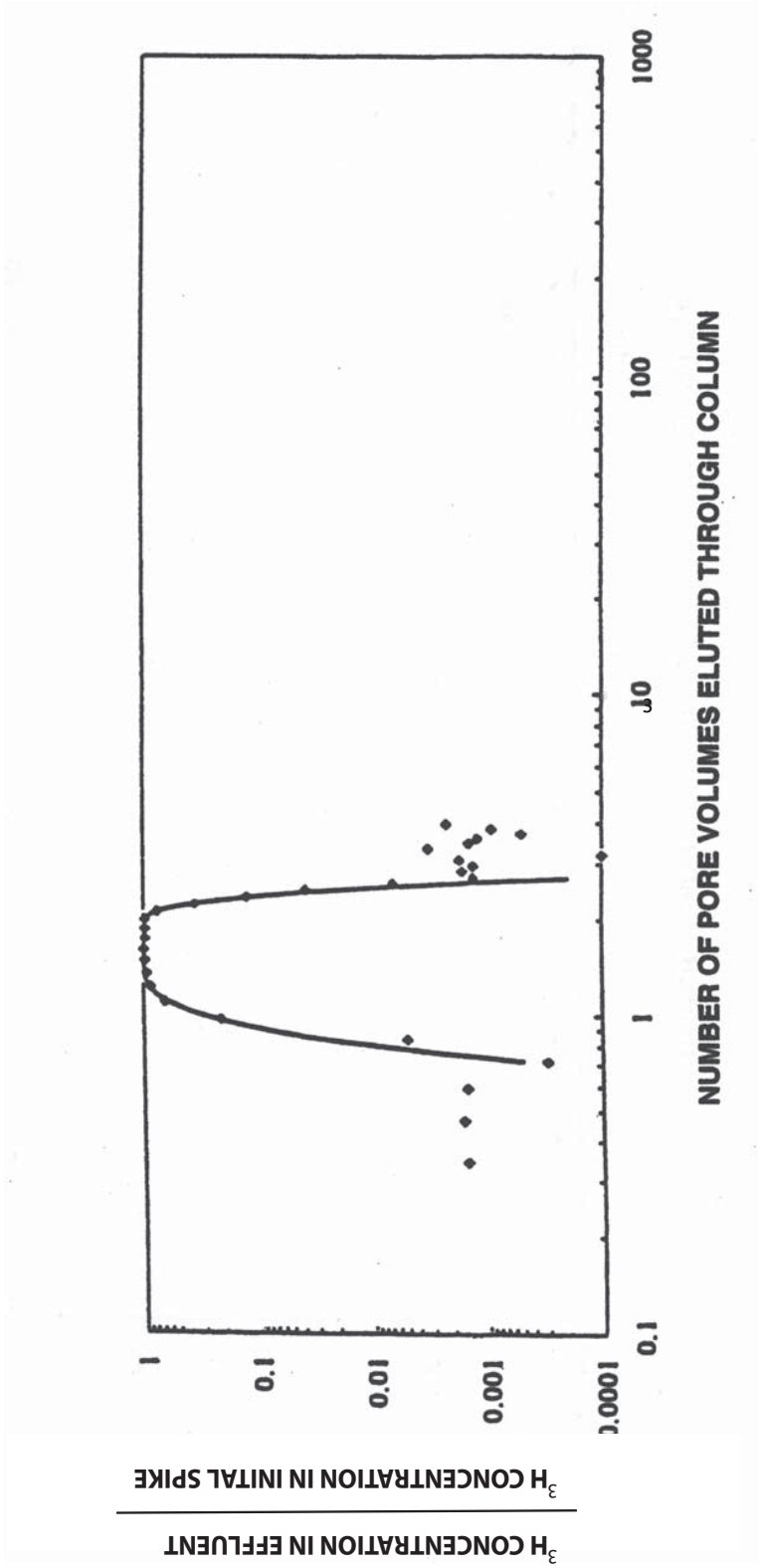

Figure 5-5. Breakthrough of ^{3}H from interbed packed column (solid diamonds represent data points and the line represents the model fit). Total ^{3}H recovery was 101.5 percent of the initial amount added to the column (from Newman and others, 1995).

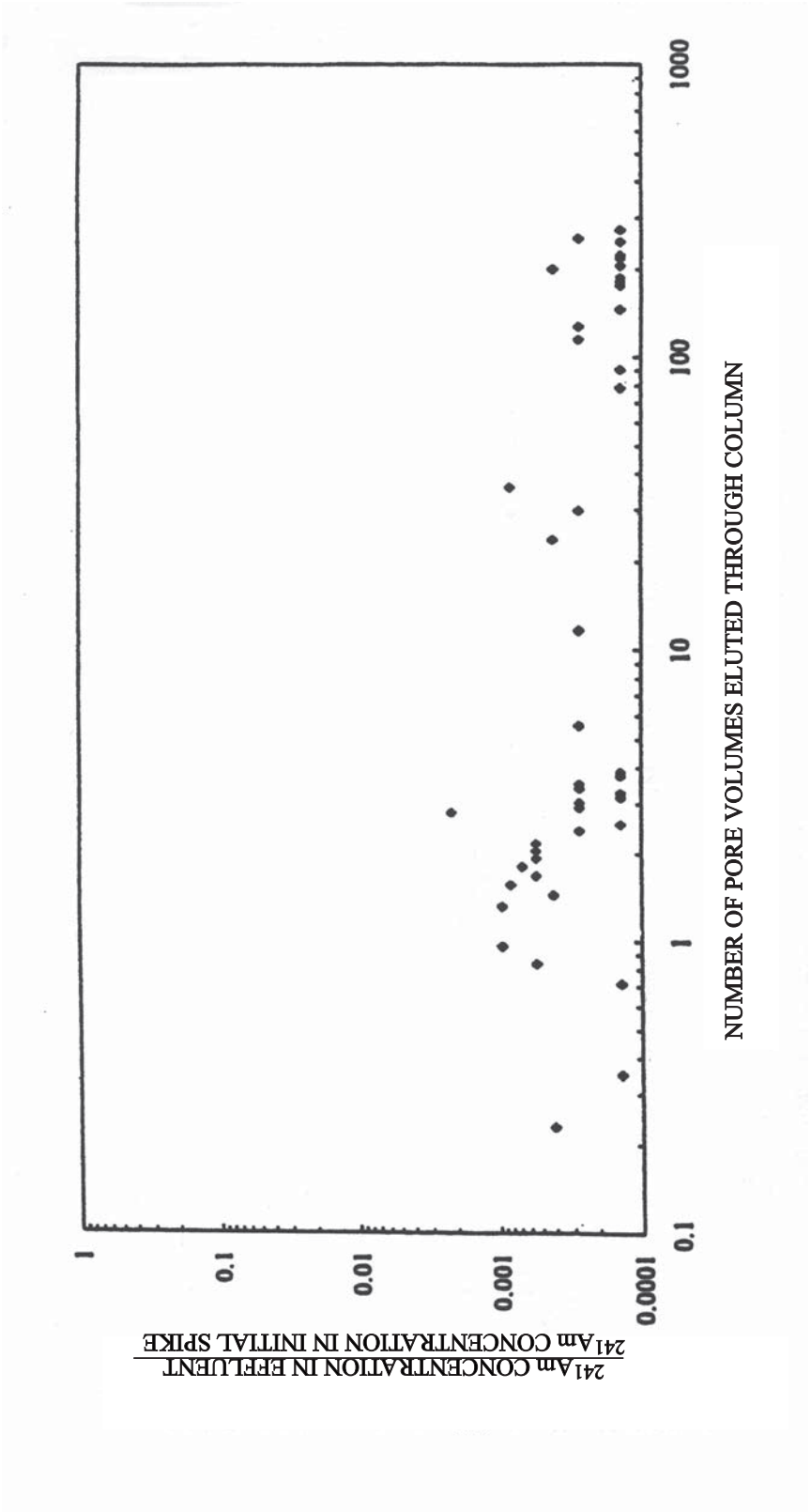

Figure 5-6. Breakthrough of ^{241}Am from interbed packed column (solid diamonds represent data points). Total ^{241}Am recovery was 1.9 percent of the initial amount added to the column (from Newman and others, 1995).

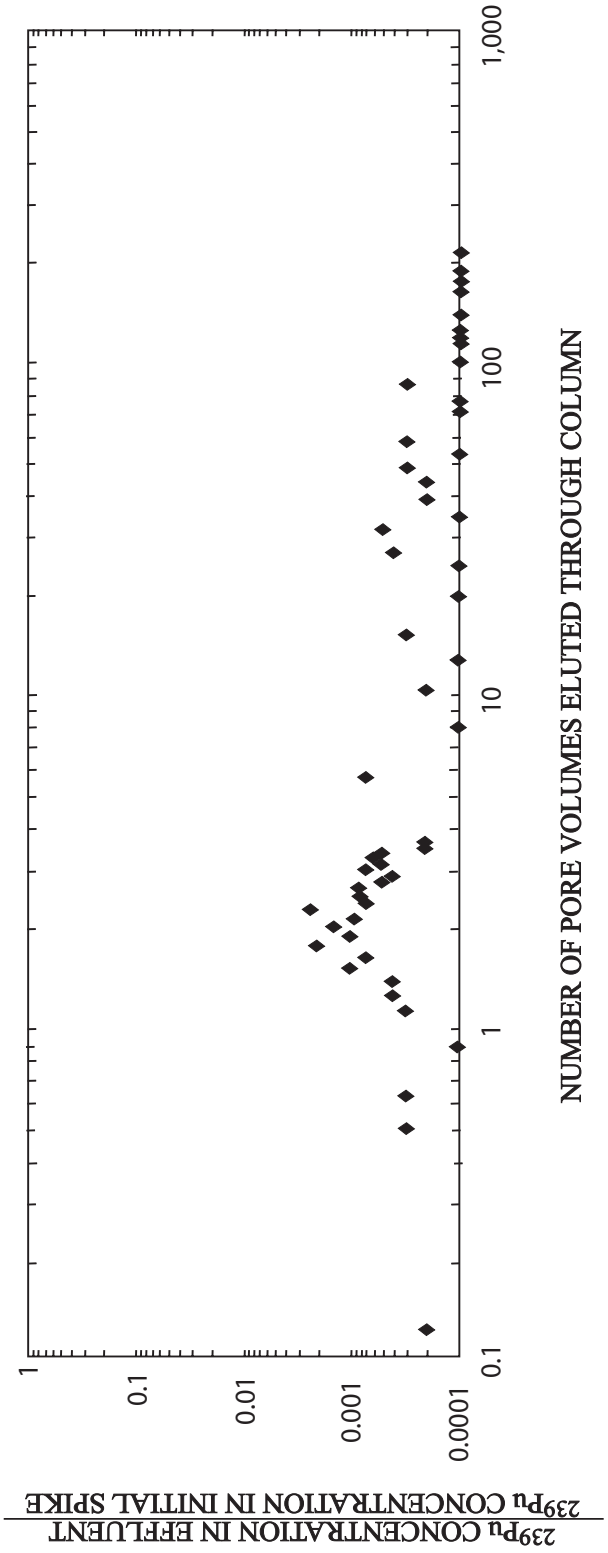

Figure 5-7. Breakthrough of ^{239}Pu from interbed packed column (solid diamonds represent data points). Total ^{239}Pu recovery was 0.1 percent of the initial amount added to the column (from Newman and others, 1995).

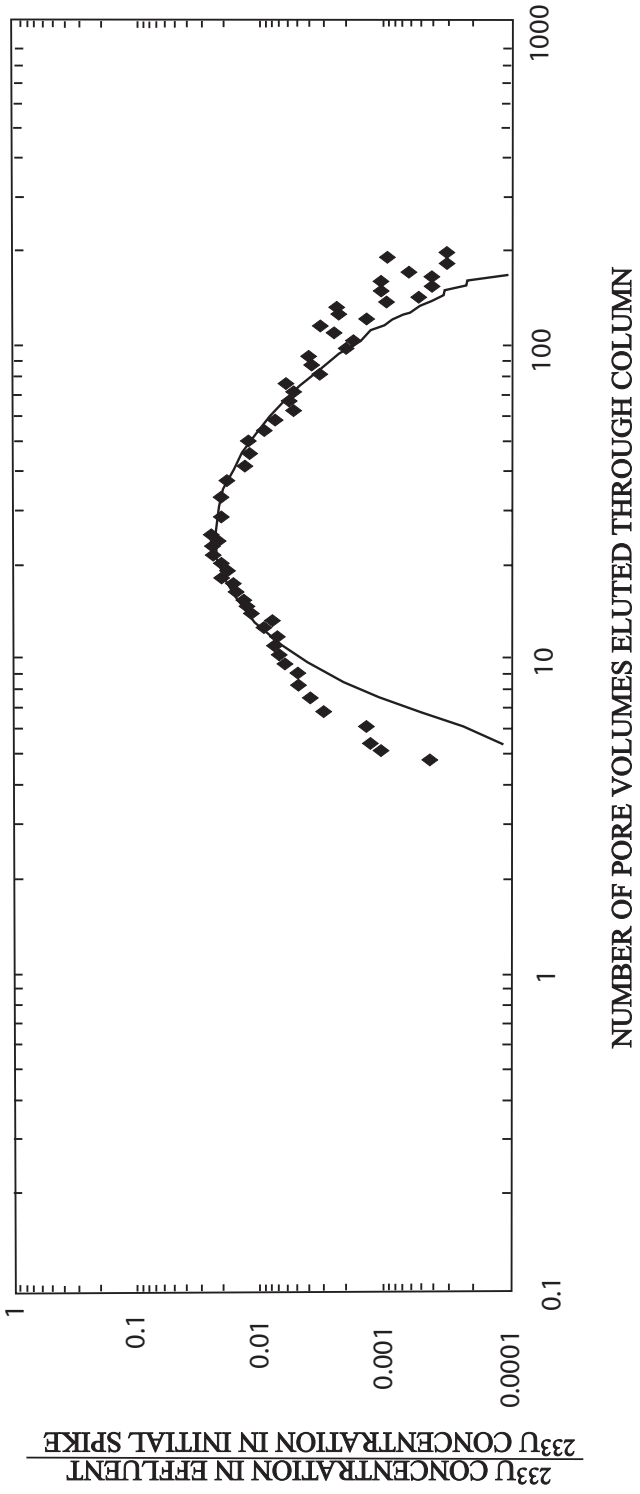

Figure 5-8. Breakthrough of ^{233}U from interbed packed column (solid diamonds represent data points and the line represents the model fit). Total ^{233}U recovery was 90.3 percent of the initial amount added to the column (from Newman and others, 1995).

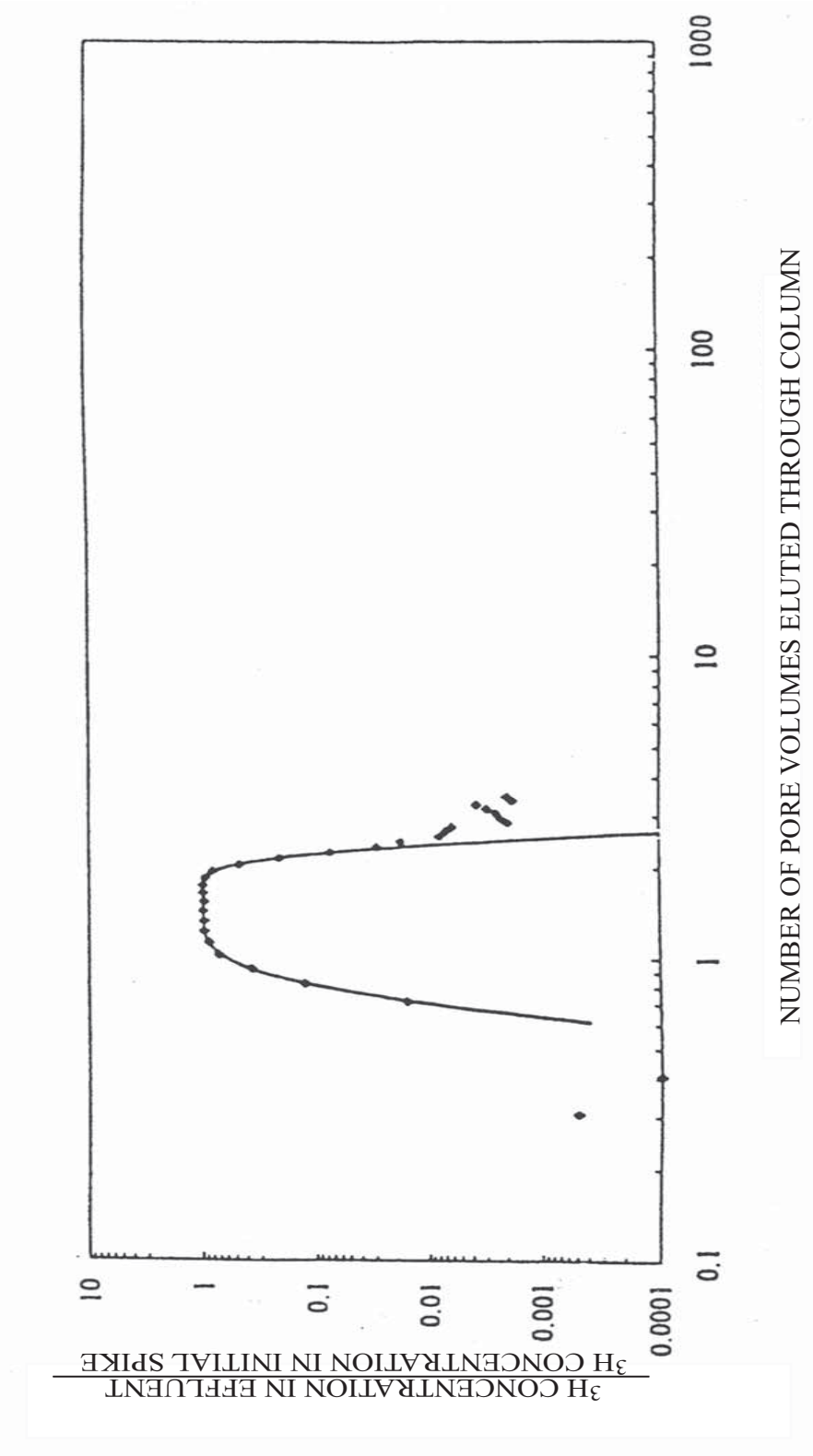

Figure 5-9. Breakthrough of ^{3}H from crushed-basalt packed column (solid diamonds represent data points and the line represents the model fit). Total ^{3}H recovery was 96.9 percent of the initial amount added to the column (from Newman and others, 1995).

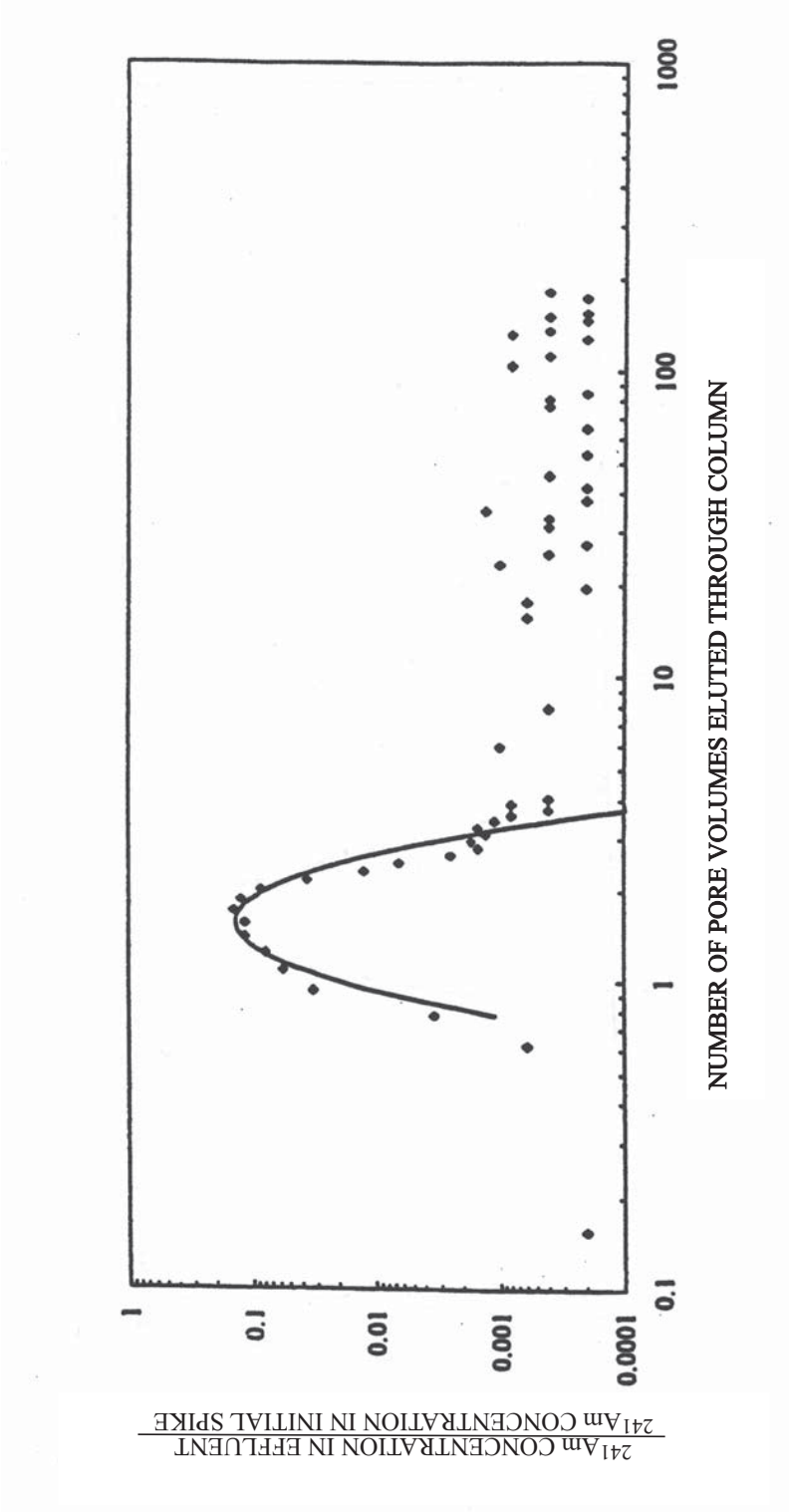

Figure 5-10. Breakthrough of ^{241}Am from crushed-basalt packed column (solid diamonds represent data points and the line represents the model fit). Total ^{241}Am recovery was 14 percent of the initial amount added to the column (from Newman and others, 1995).

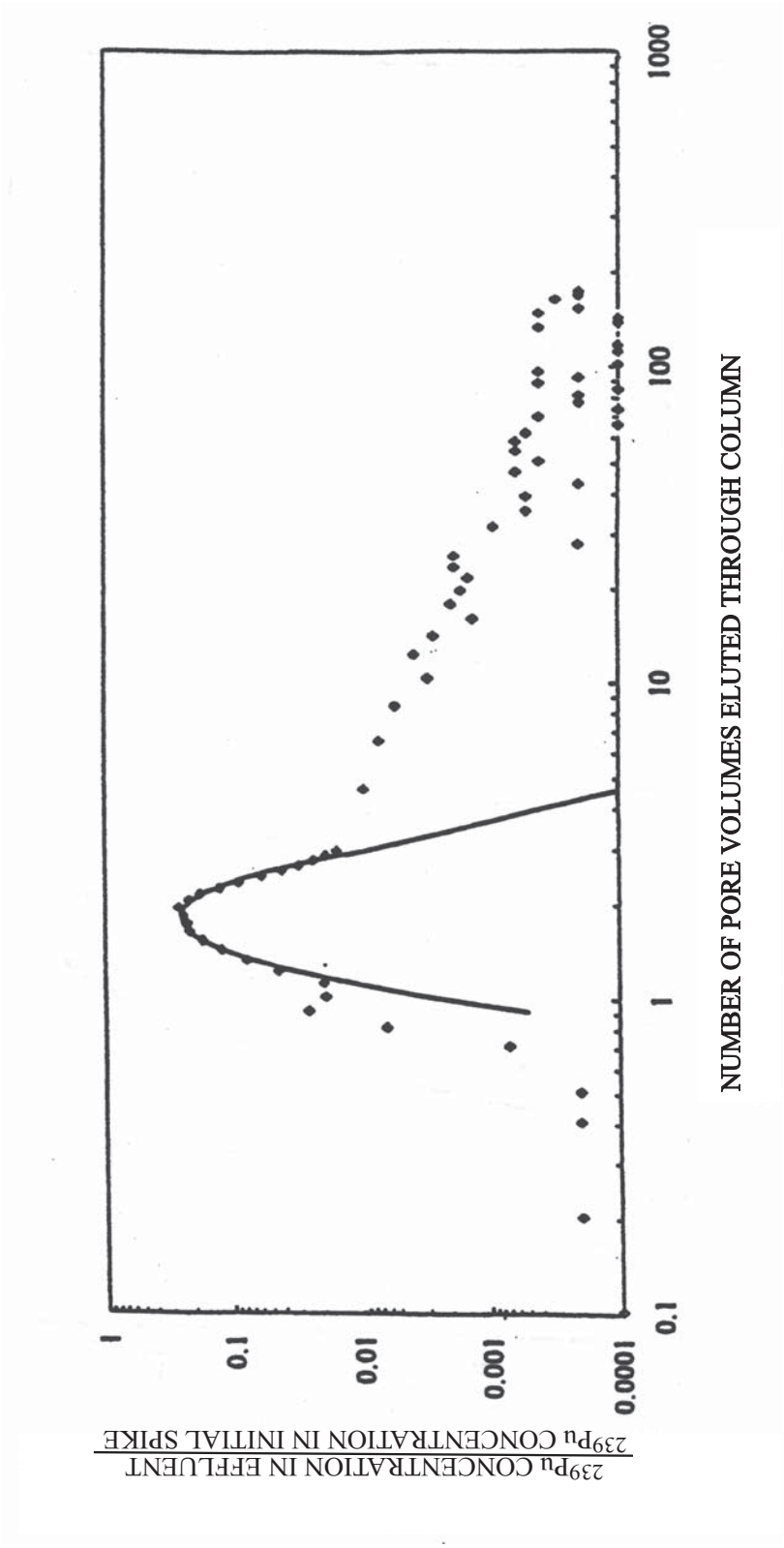

Figure 5-11. Breakthrough of ^{239}Pu from crushed-basalt packed column (solid diamonds represent data points and the line represents the model fit). Total ^{239}Pu recovery was 33.5 percent of the initial amount added to the column (from Newman and others, 1995).

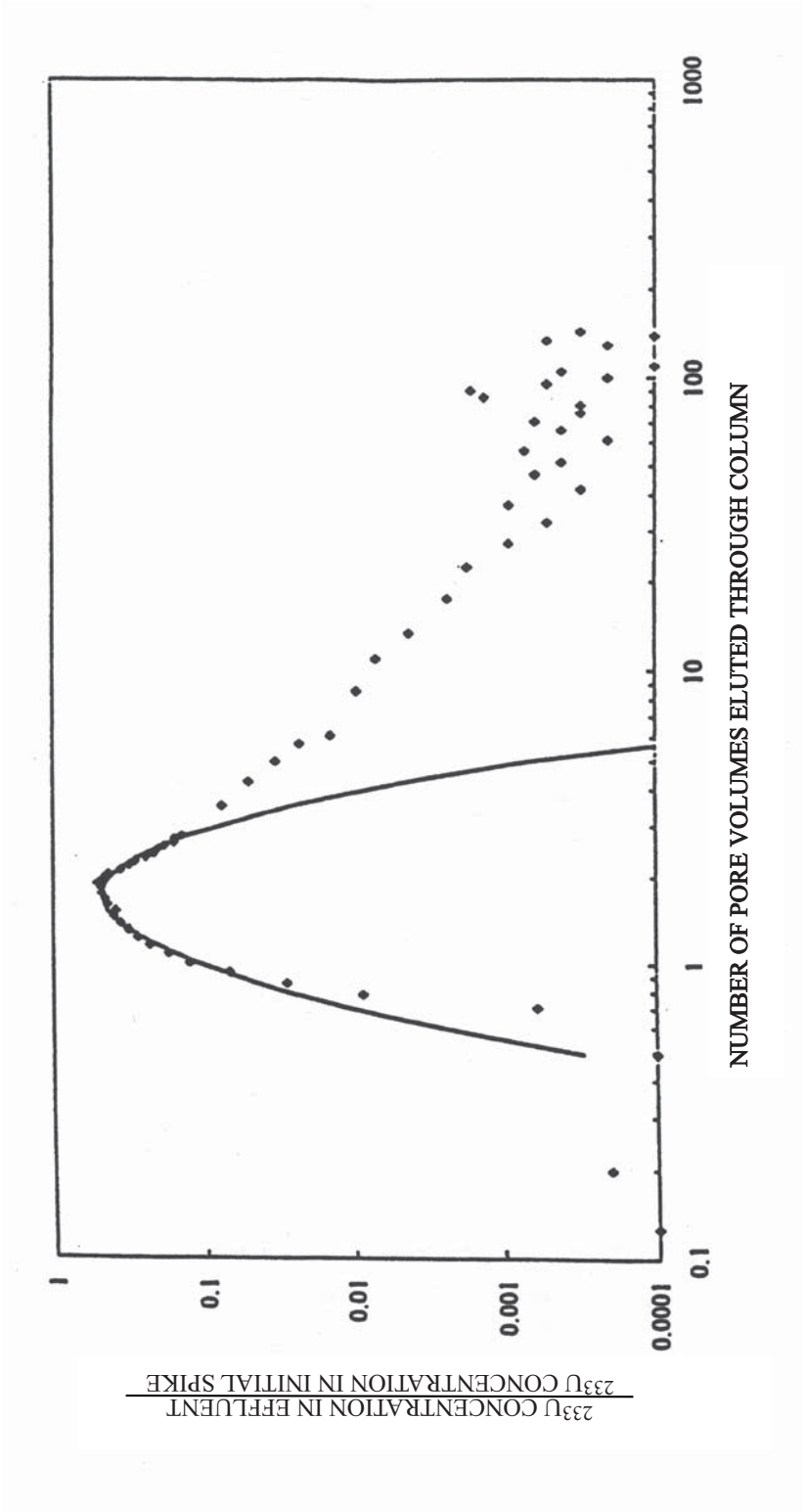

Figure 5-12. Breakthrough of ^{233}U from crushed-basalt packed column (solid diamonds represent data points and the line represents the model fit). Total ^{233}U recovery was 89.9 percent of the initial amount added to the column (from Newman and others, 1995).

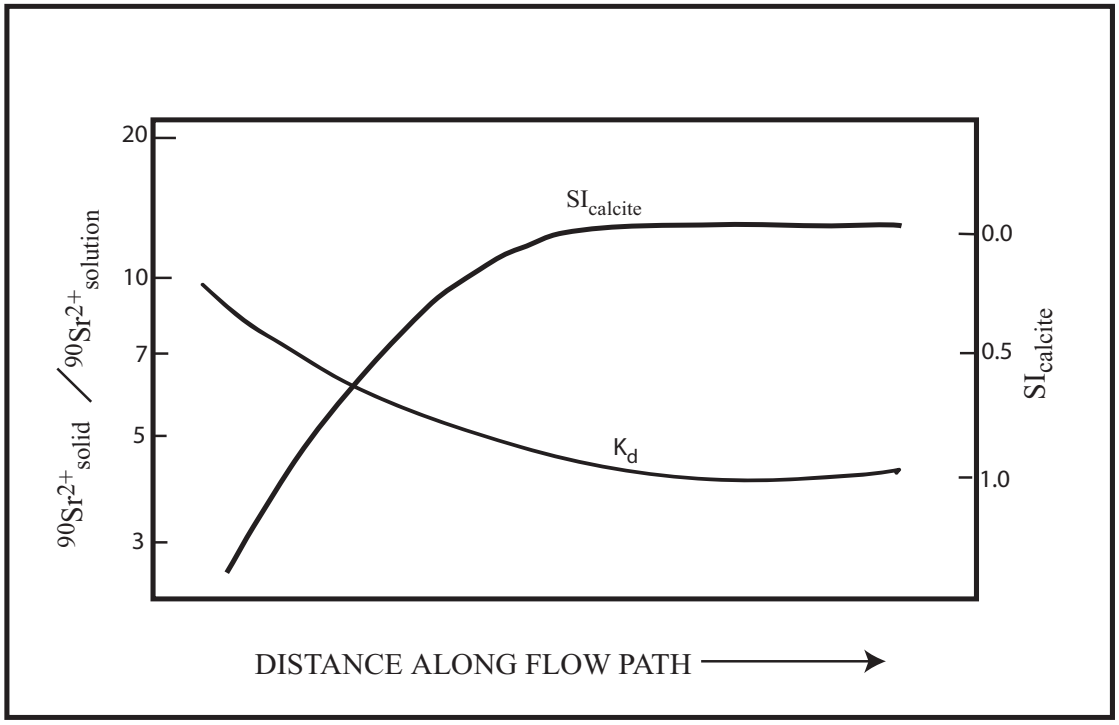

Figure 5-13. Variation of calcite saturation indices ($SI_{calcite}$) and ^{90}Sr partitioning (K_d) between the solution and an ion-exchange phase in a one-dimensional column at chemical steady state (from Reardon, 1981).

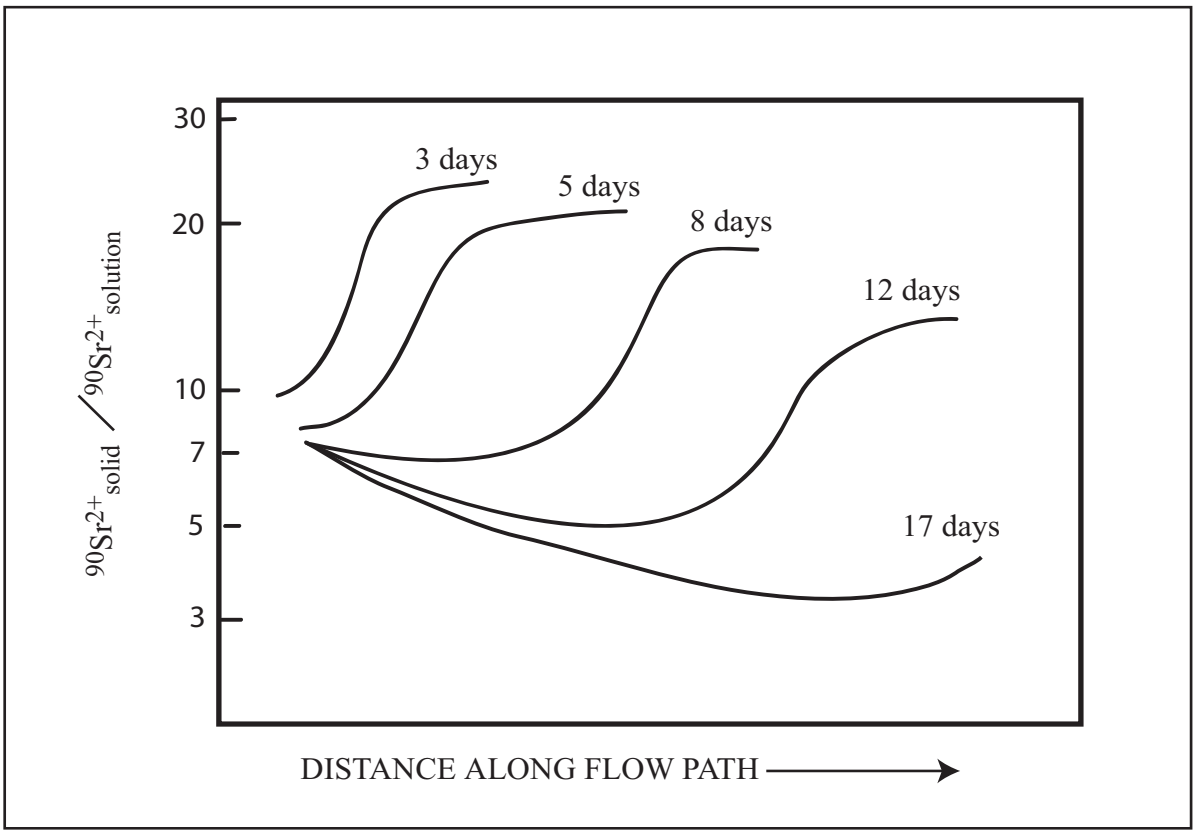

Figure 5-14. Temporal and spatial changes in ^{90}Sr partitioning (K_d) between the solution and an ion-exchange phase in a dynamically evolving system. After 17 days of transport time, the system is near chemical steady state (from Reardon, 1981).

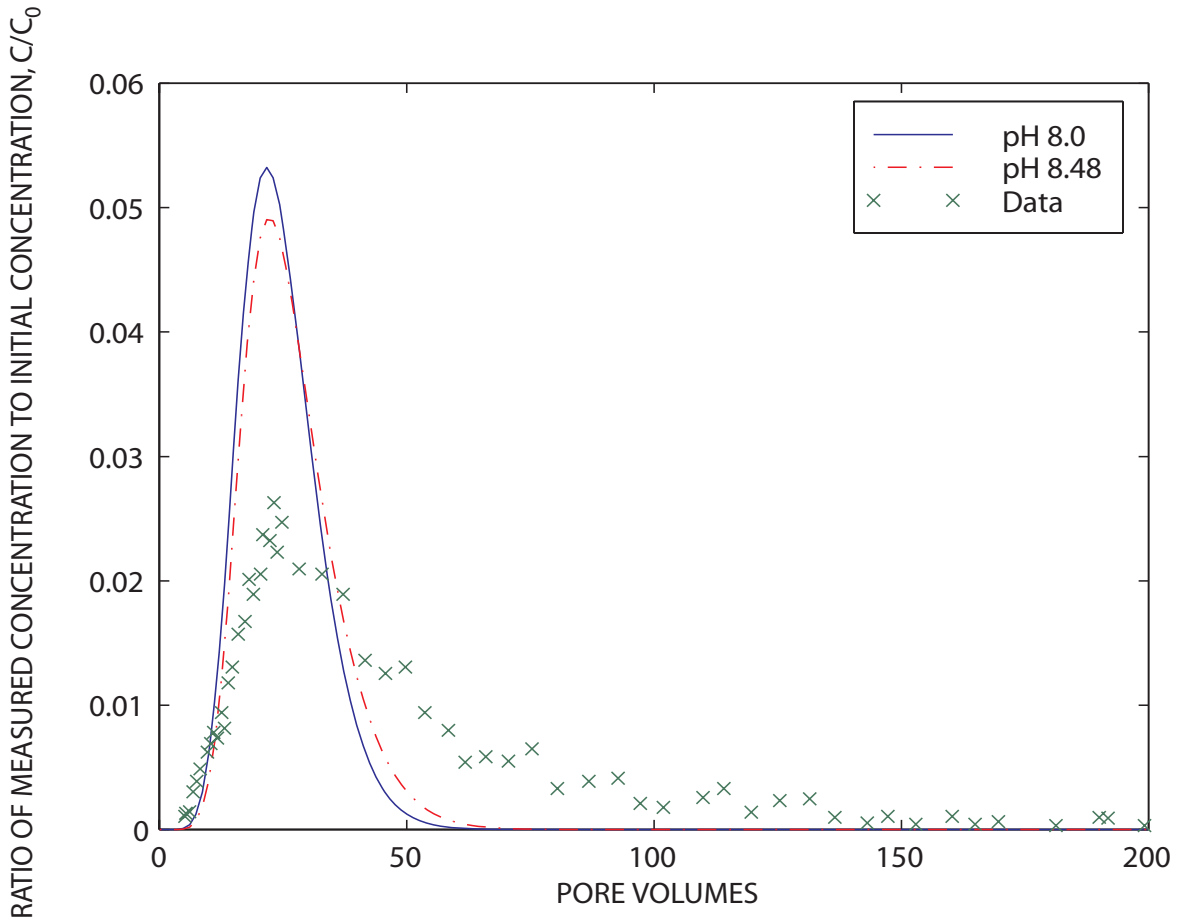

Figure 5-15. Fitted reactive transport simulations and experimental breakthrough curves for U(VI) in columns packed with sedimentary interbed materials.

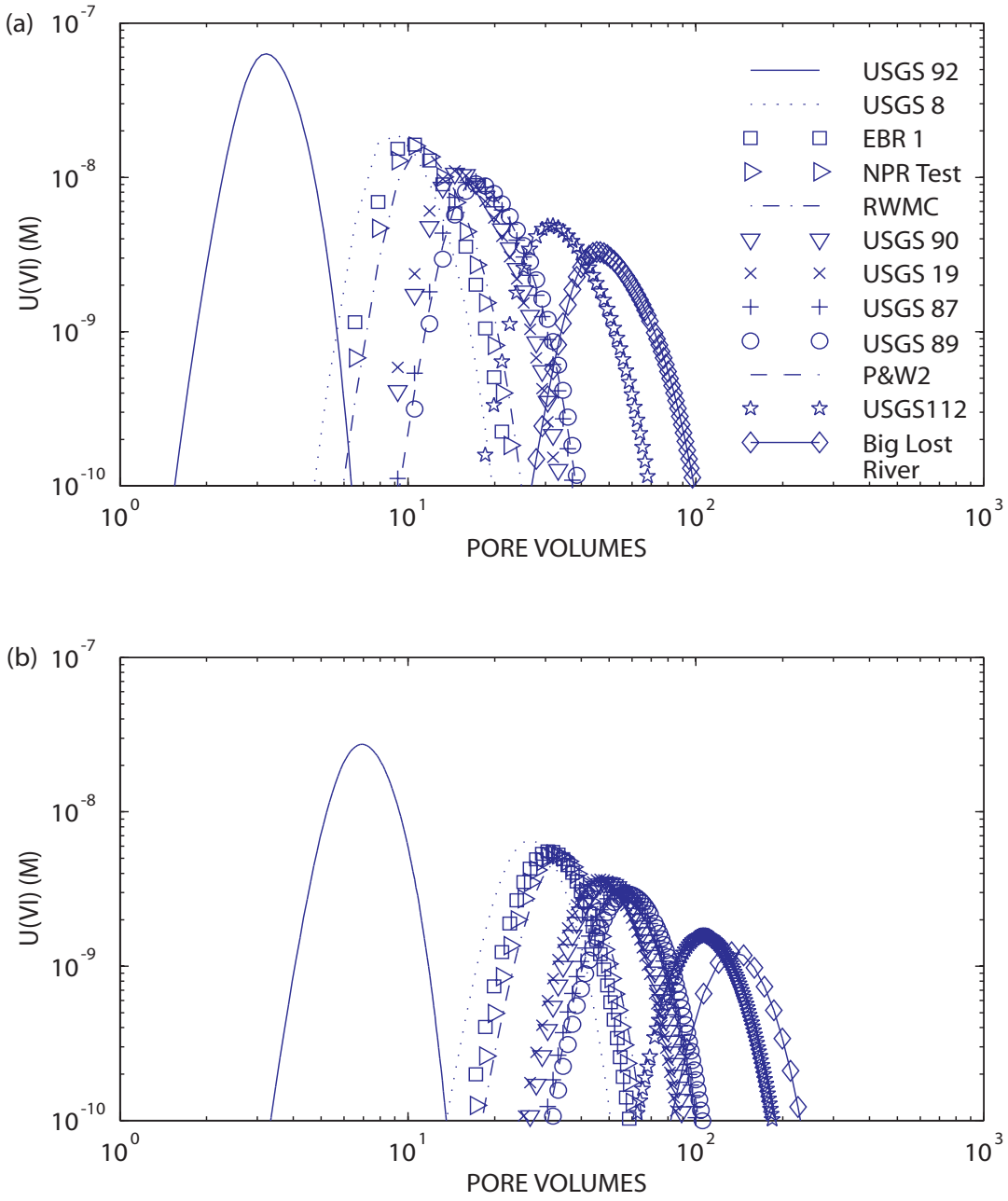

Figure 5-16. Simulated breakthrough curves for the transport of one pore volume of 10^{-7} M U(VI) in 12 INEEL surface- and ground-water samples for (a) a total site density assuming a constant pH of 8, and (b) a total site density assuming a constant pH of 8.48 [M, molarity].

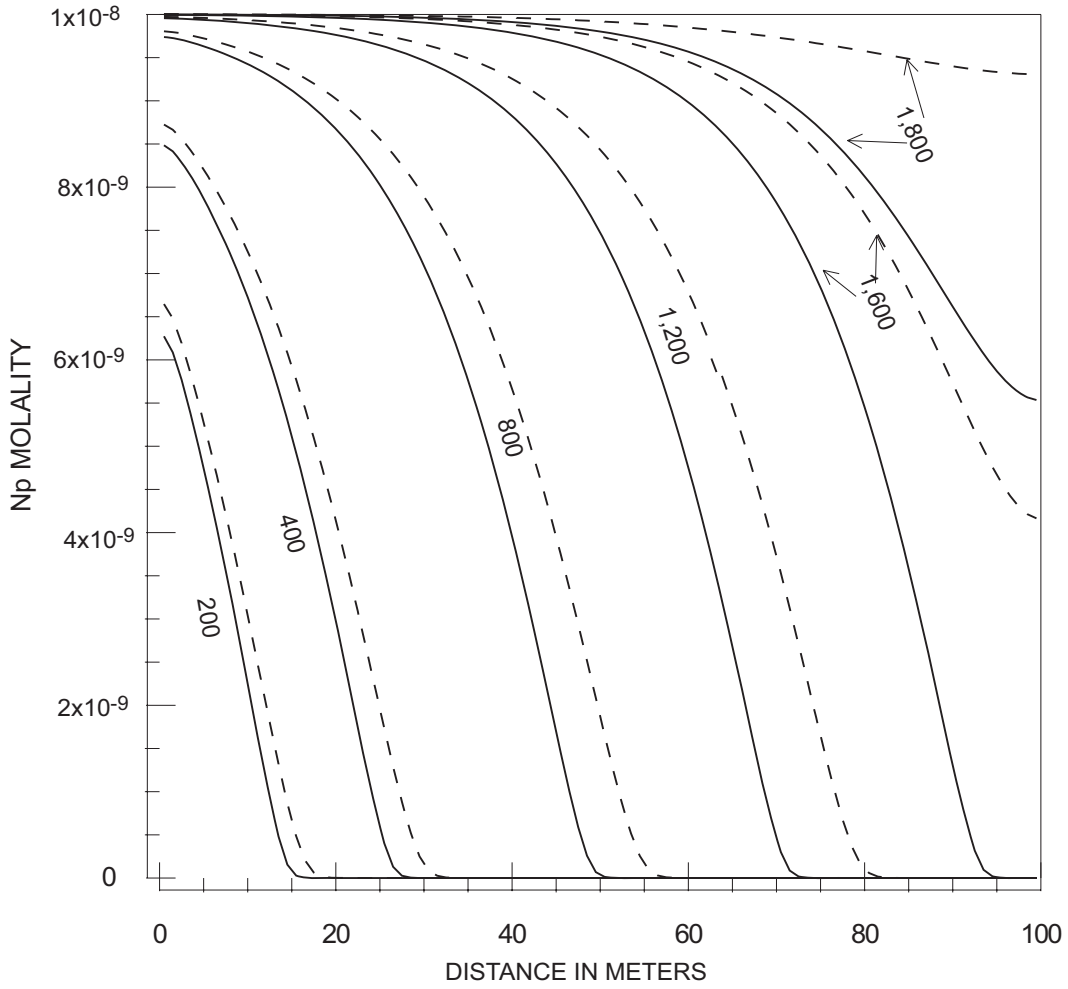

Figure 5-17. Np aqueous concentrations as a function of distance according to PHREEQC simulations of one-dimensional advective-dispersive transport with a surface and aqueous complexation model. Np infiltration results are provided for different timesteps (labels next to curves) and for simulations in which equilibrium with calcite was either specified (dashed line) or not specified (solid line). Simulations used Np aqueous thermodynamic data from the ANSTO data base.

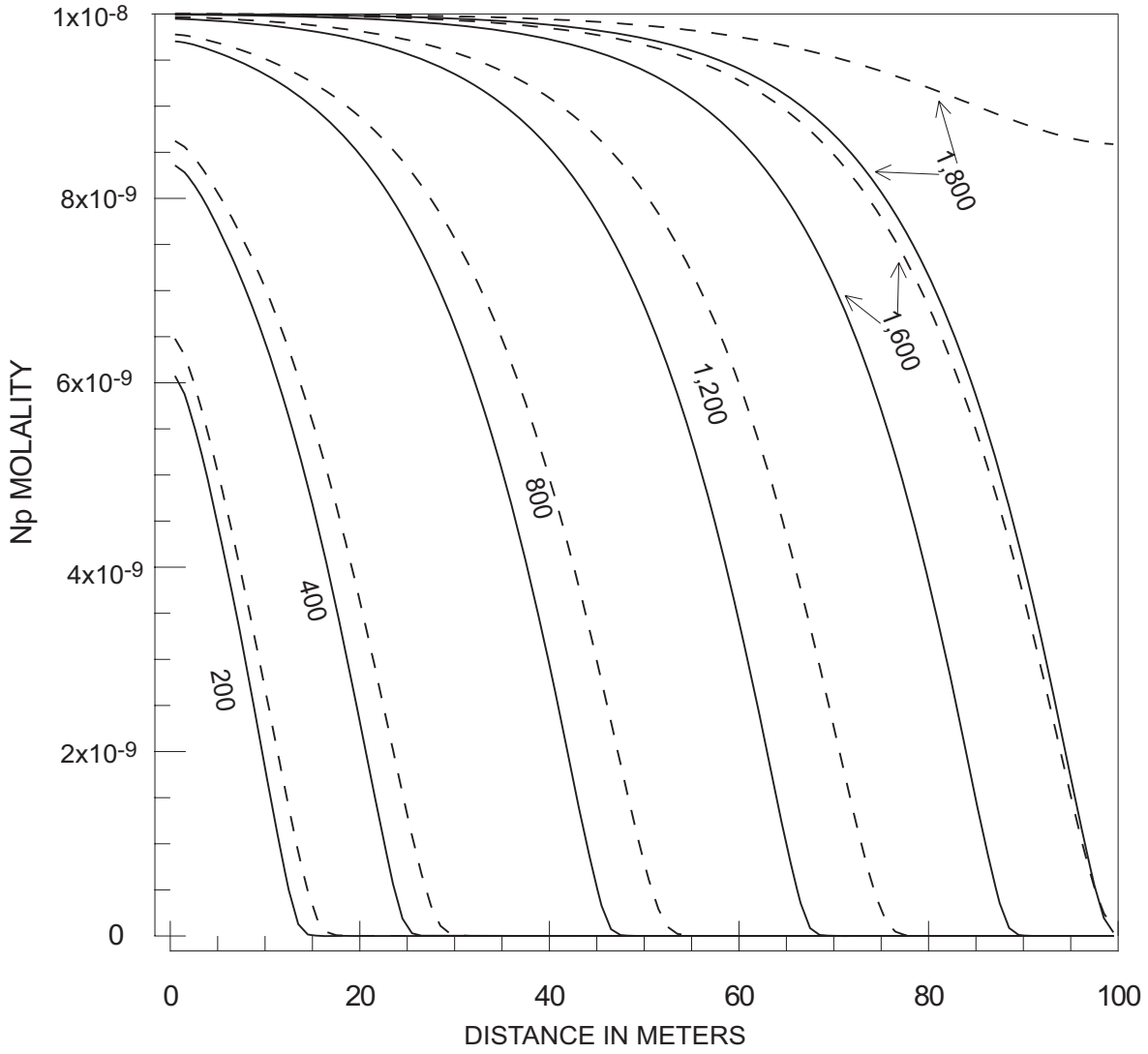

Figure 5-18. Np aqueous concentrations as a function of distance according to PHREEQC simulations of one-dimensional advective-dispersive transport with a surface and aqueous complexation model. Np infiltration results are provided for different timesteps (labels next to curves) and for simulations in which equilibrium with calcite was either specified (dashed line) or not specified (solid line). Simulations used Np aqueous thermodynamic data from the EQ3/6 data base.

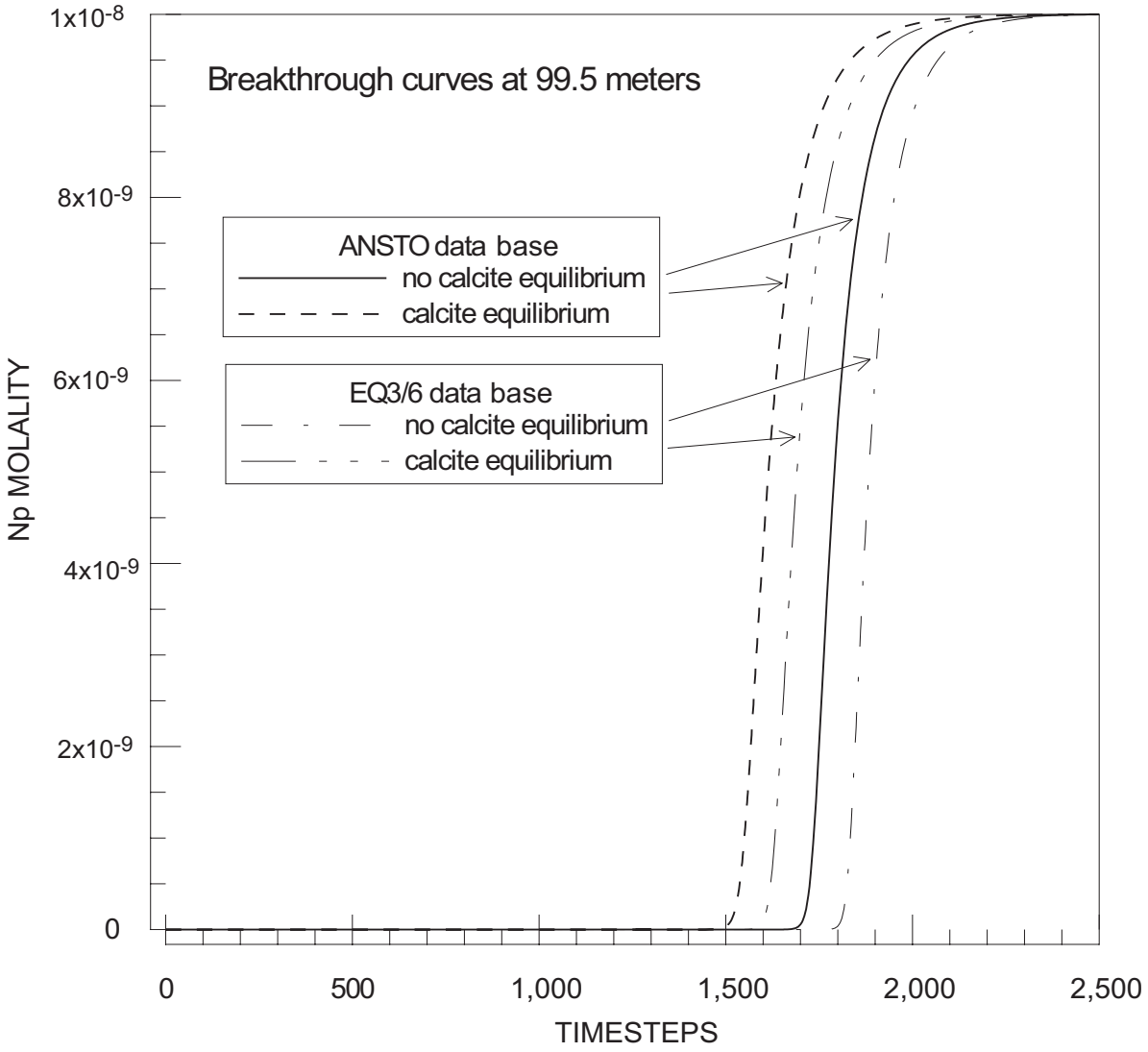

Figure 5-19. Np aqueous concentrations as a function of timestep. Np infiltration results identify the source of Np thermodynamic data used (ANSTO or EQ3/6) and whether calcite equilibrium was specified throughout the one-dimensional column.

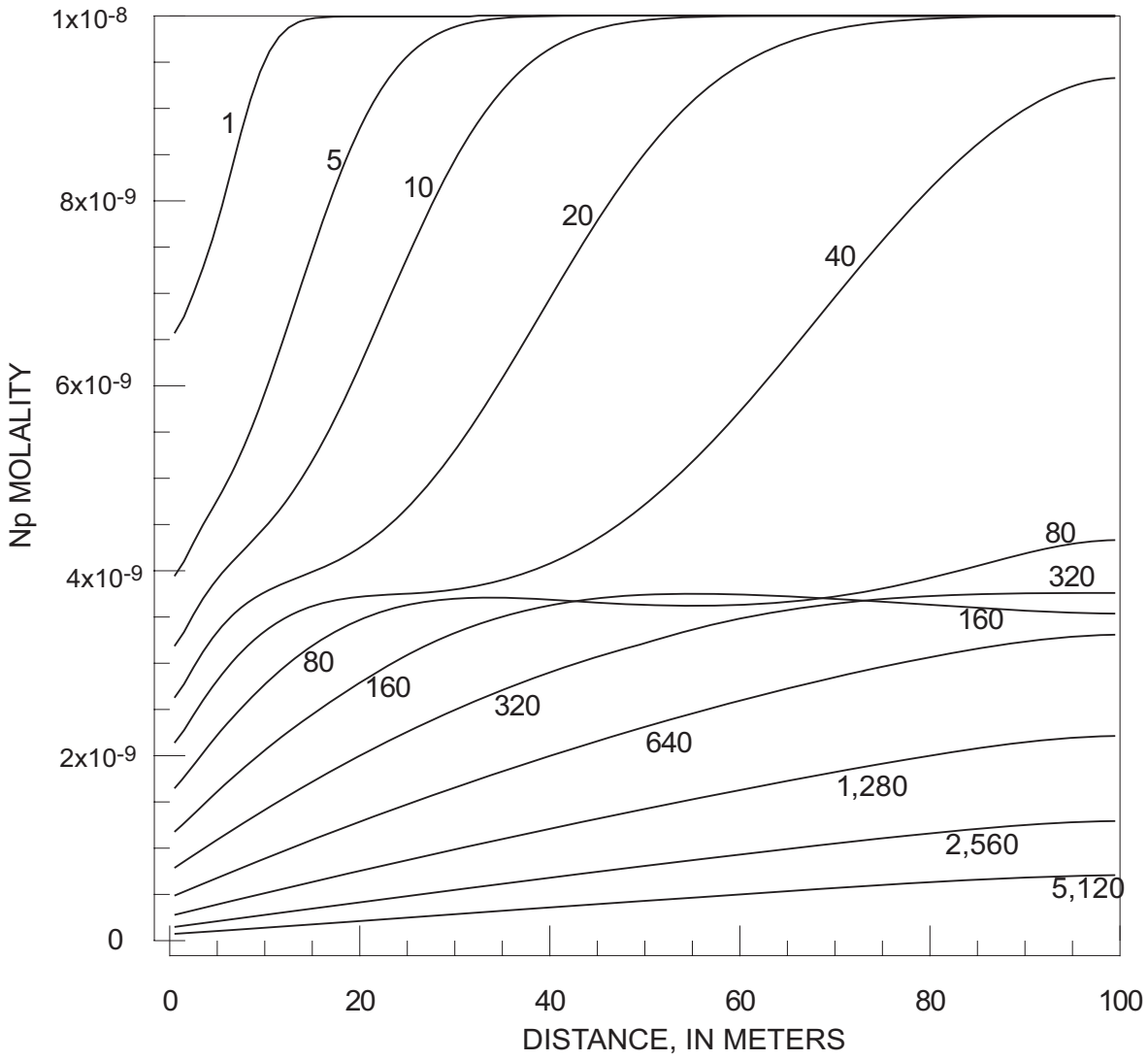

Figure 5-20. Np aqueous concentrations as a function of distance according to PHREEQC reactive transport simulations. Np cleanup results are provided for different timesteps (labels next to curves). Equilibrium with calcite was not specified. Np thermodynamic data were taken from the ANSTO data base.

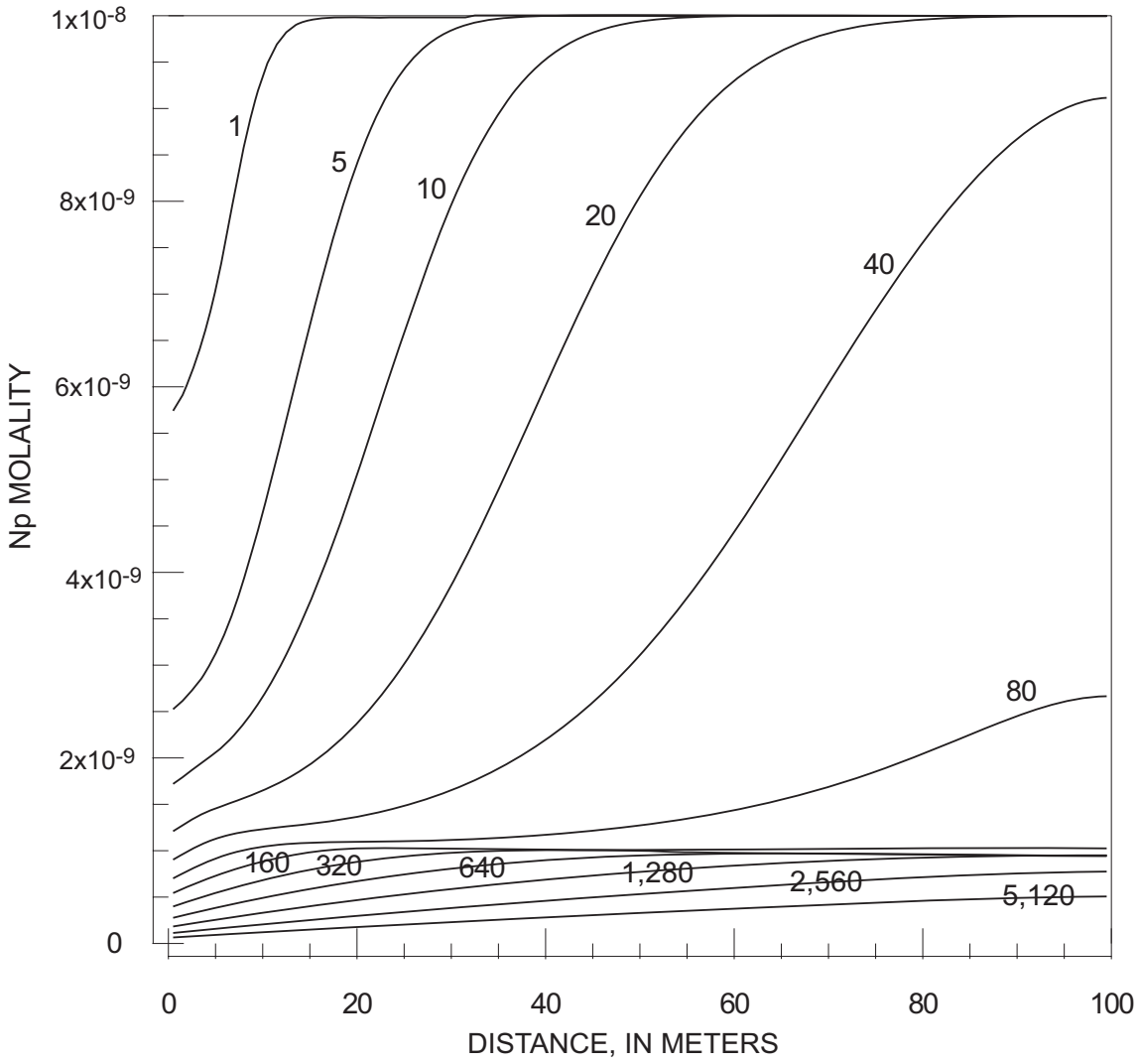

Figure 5-21. Np aqueous concentrations as a function of distance according to PHREEQC reactive transport simulations. Np cleanup results are provided for different timesteps (labels next to curves). Equilibrium with calcite was not specified. Np thermodynamic data were taken from the EQ3/6 data base.

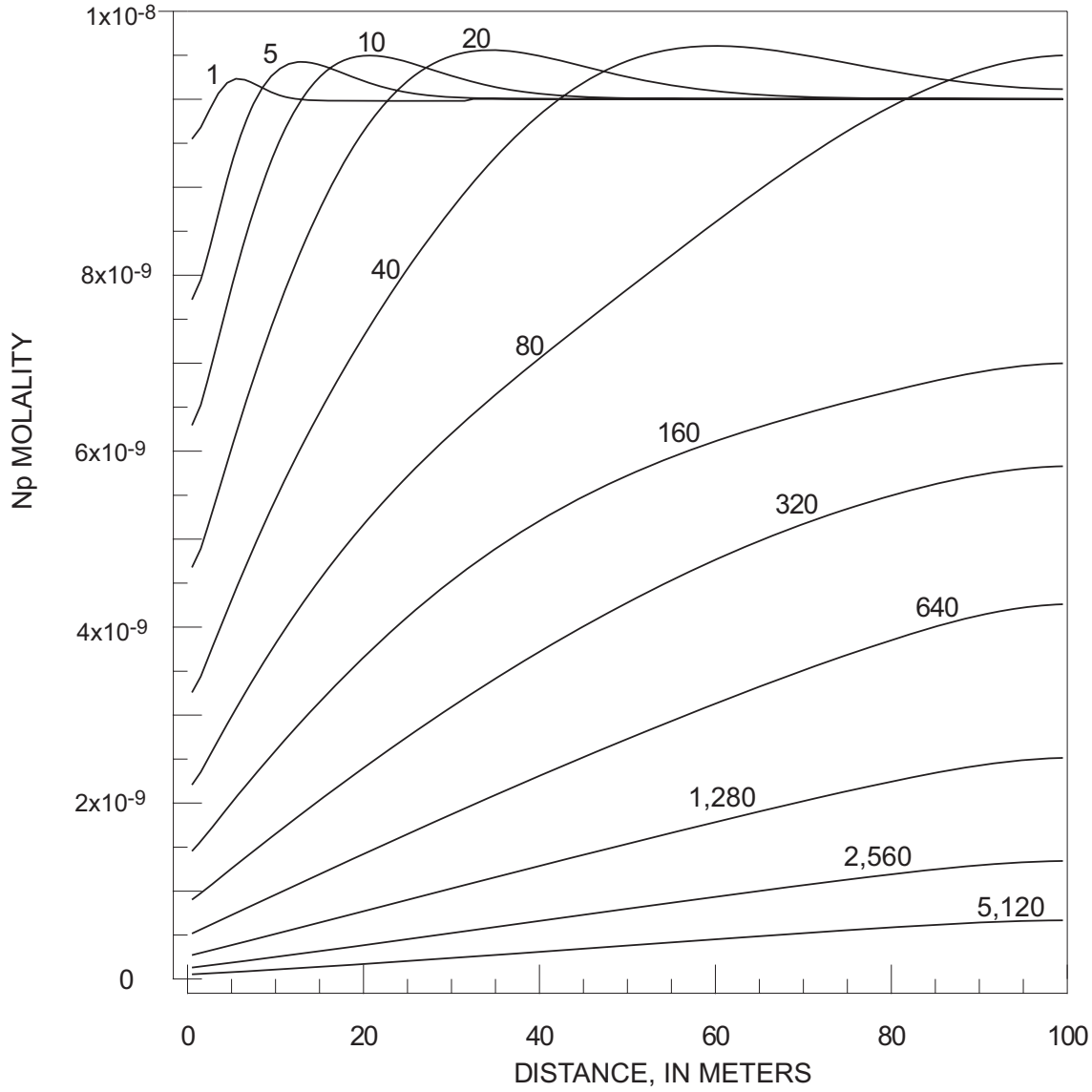

Figure 5-22. Np aqueous concentrations as a function of distance according to PHREEQC reactive transport simulations. Np cleanup results are provided for different timesteps (labels next to curves). Equilibrium with calcite was specified. Np thermodynamic data were taken from the ANSTO data base.

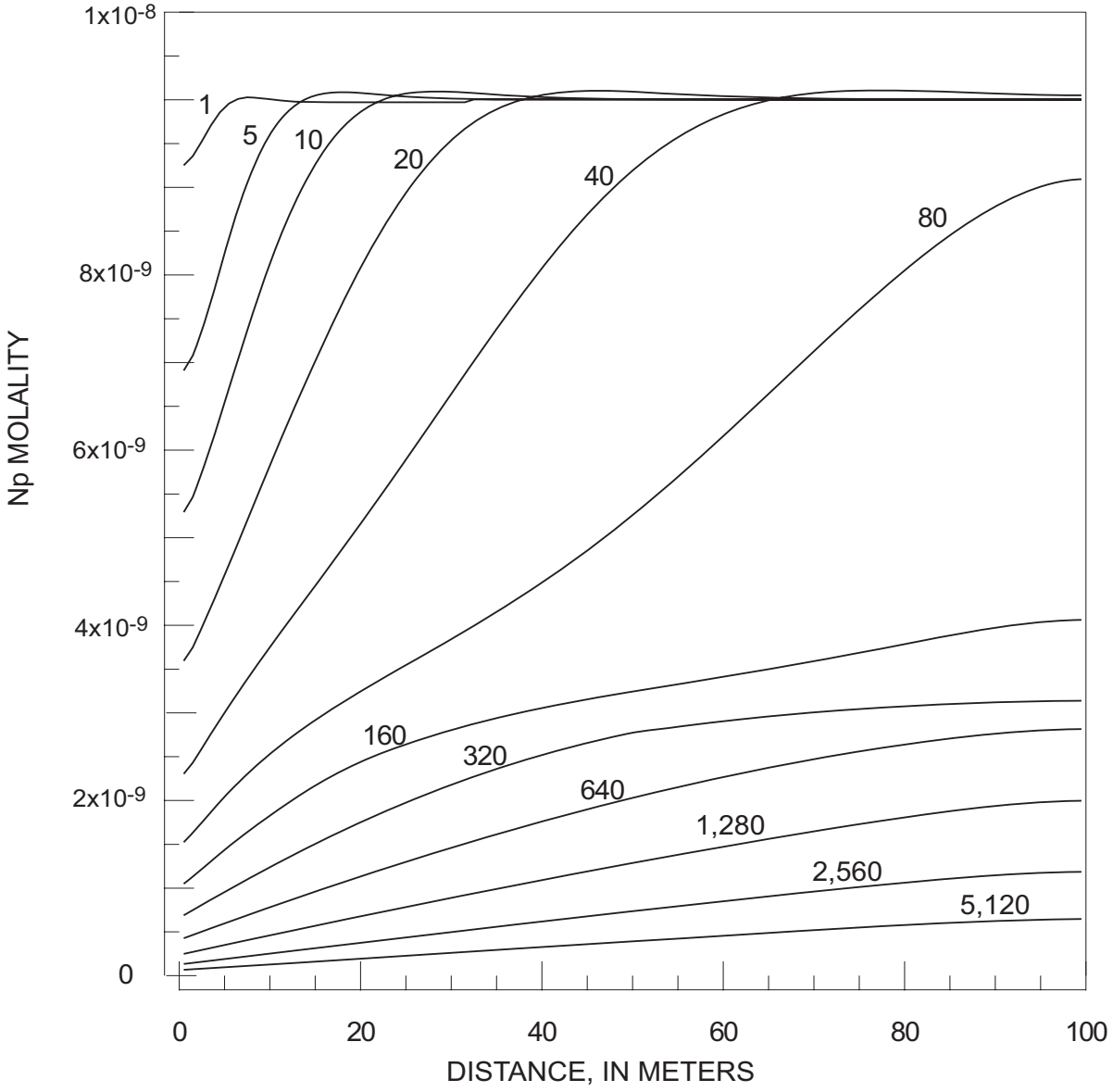

Figure 5-23. Np aqueous concentrations as a function of distance according to PHREEQC reactive transport simulations. Np cleanup results are provided for different timesteps (labels next to curves). Equilibrium with calcite was specified. Np thermodynamic data were taken from the EQ3/6 data base.

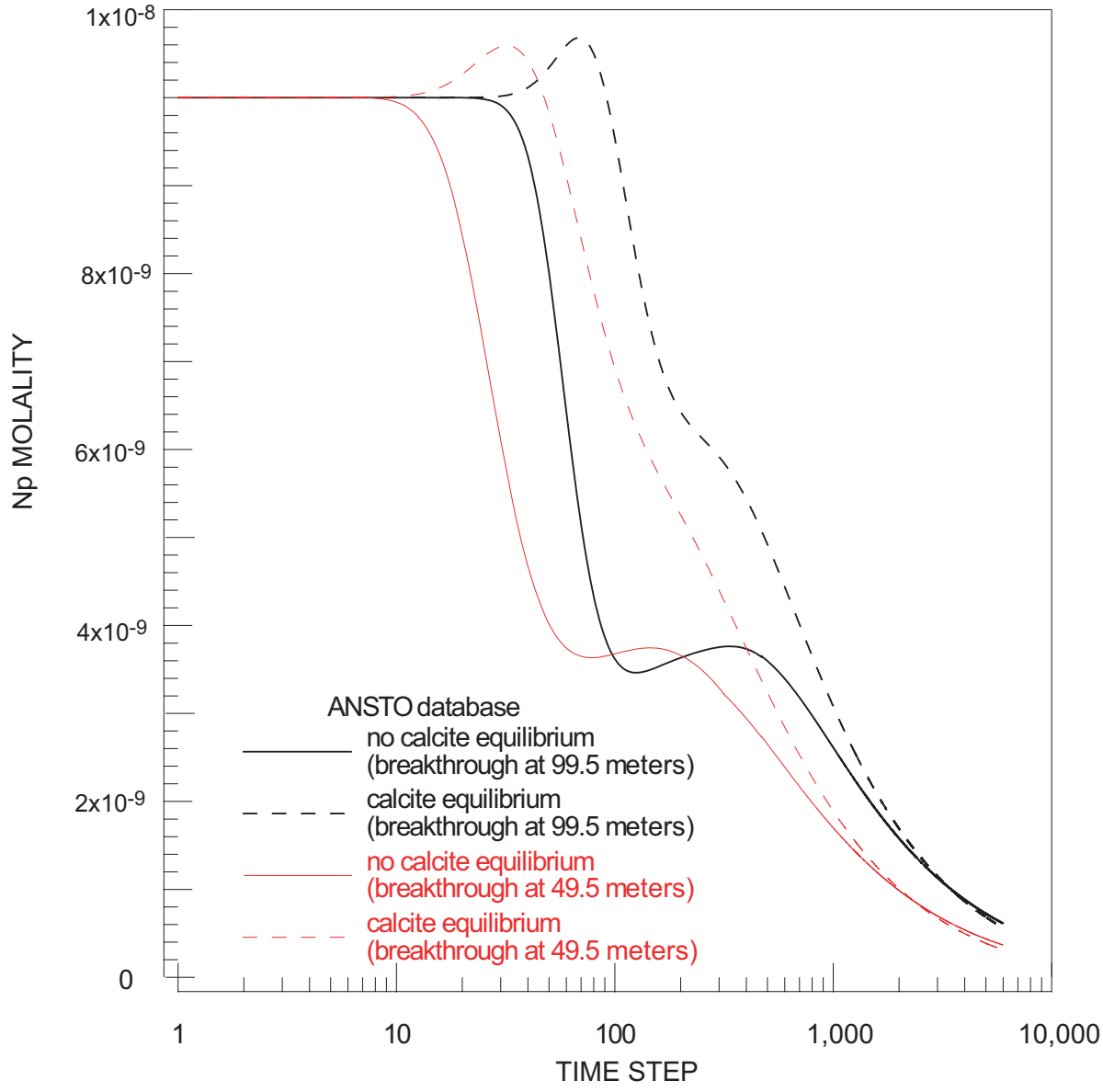

Figure 5-24. Np aqueous concentrations as a function of timestep as simulated by PHREEQC for mid-column and end-of-column sampling points. Np cleanup results identify whether calcite equilibrium was specified throughout the one-dimensional column. Np thermodynamic data were taken from the ANSTO data base.

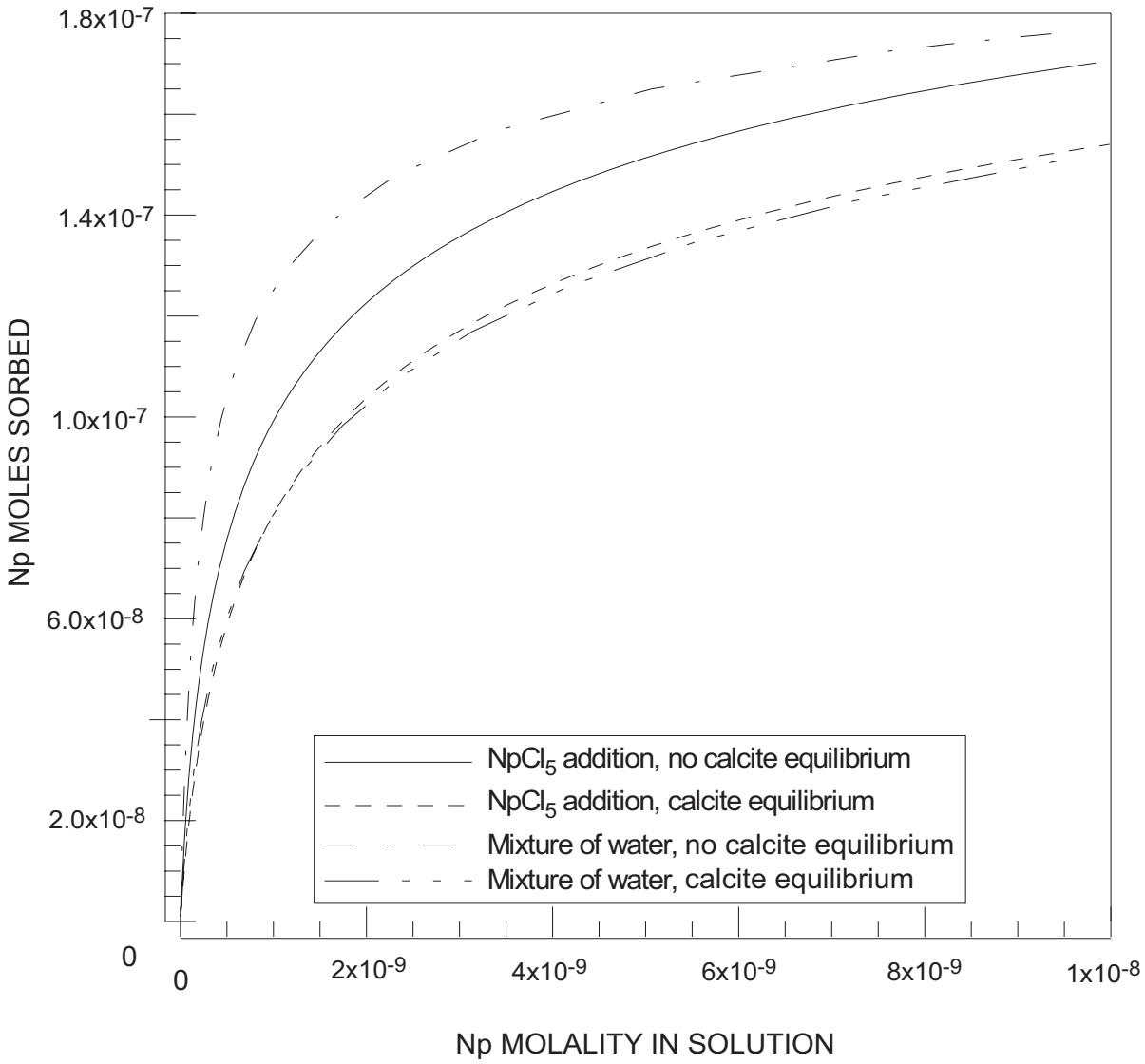

Figure 5-25. Np sorption isotherms calculated from PHREEQC simulations according to various geochemical conditions (specification or lack thereof of calcite equilibrium; presence or absence of water from well USGS 92).

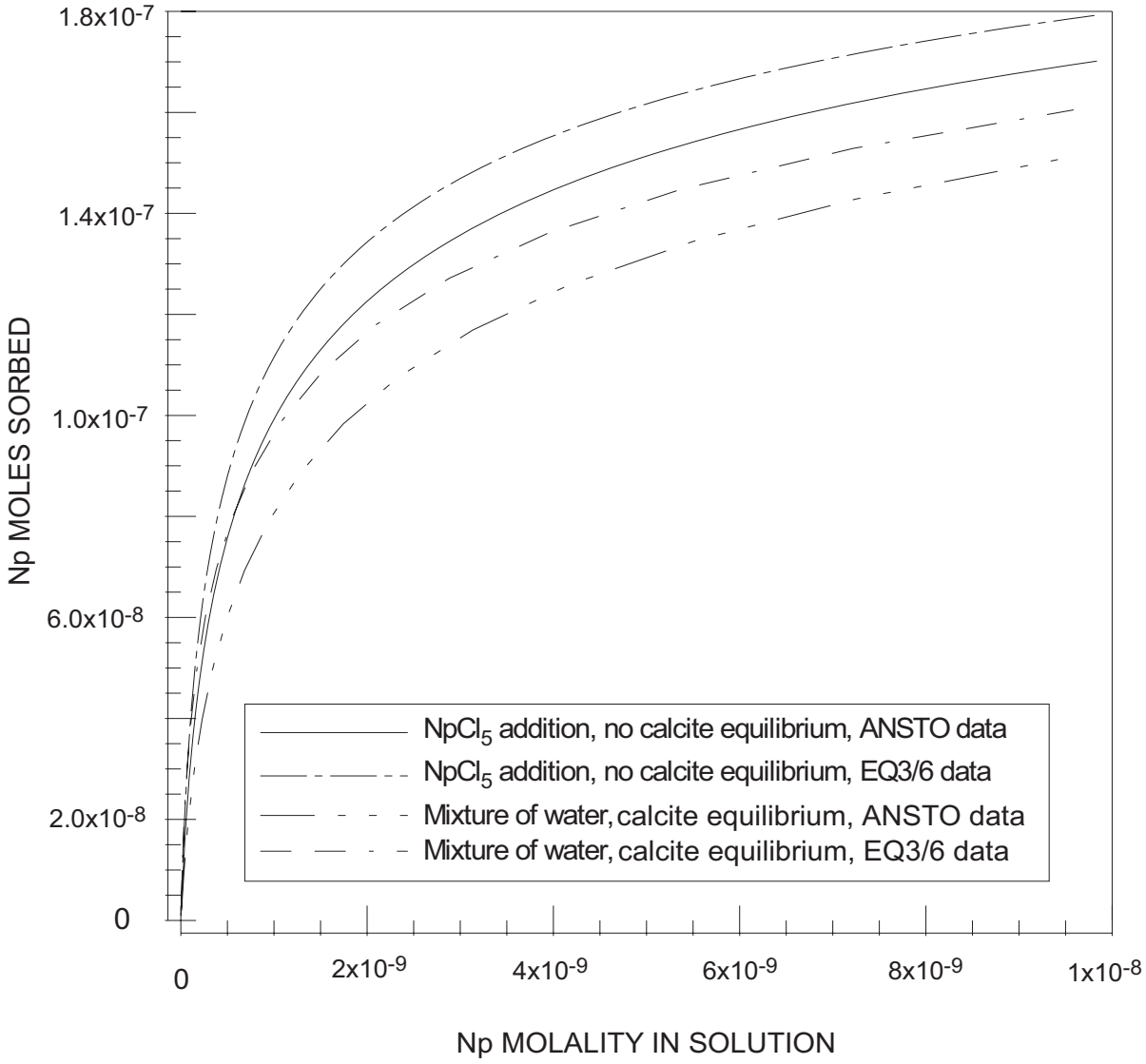

Figure 5-26. Np sorption isotherms calculated from PHREEQC simulations according to various geochemical conditions (specification or lack thereof of calcite equilibrium; presence or absence of water from well USGS 92) and to the source of Np aqueous thermodynamic data (ANSTO or EQ3/6 data base).

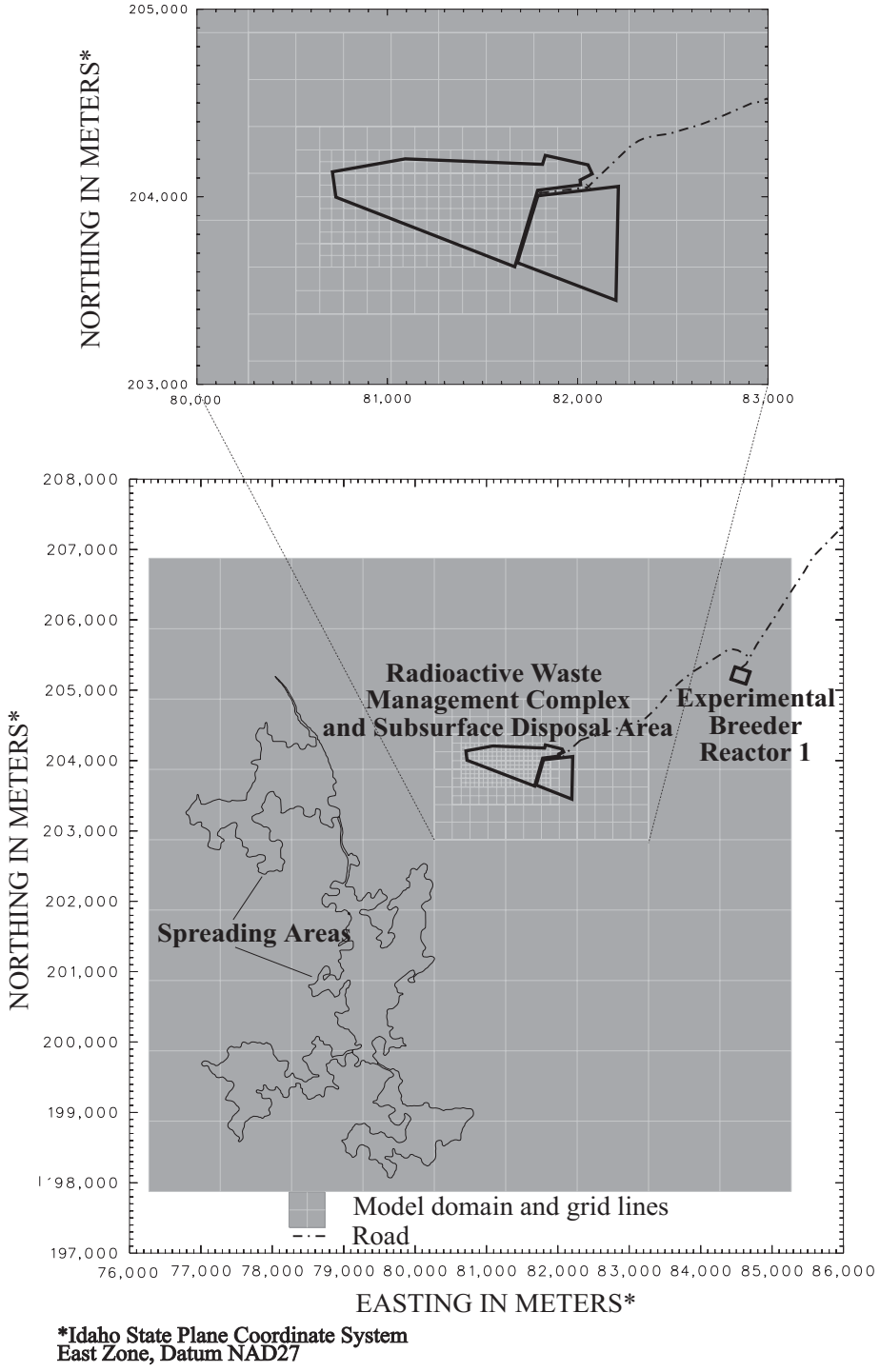

Figure 6-1. Model domain and grid of the Waste Area Group 7 numerical simulator, Radioactive Waste Management Complex and vicinity, Idaho National Engineering and Environmental Laboratory, Idaho.

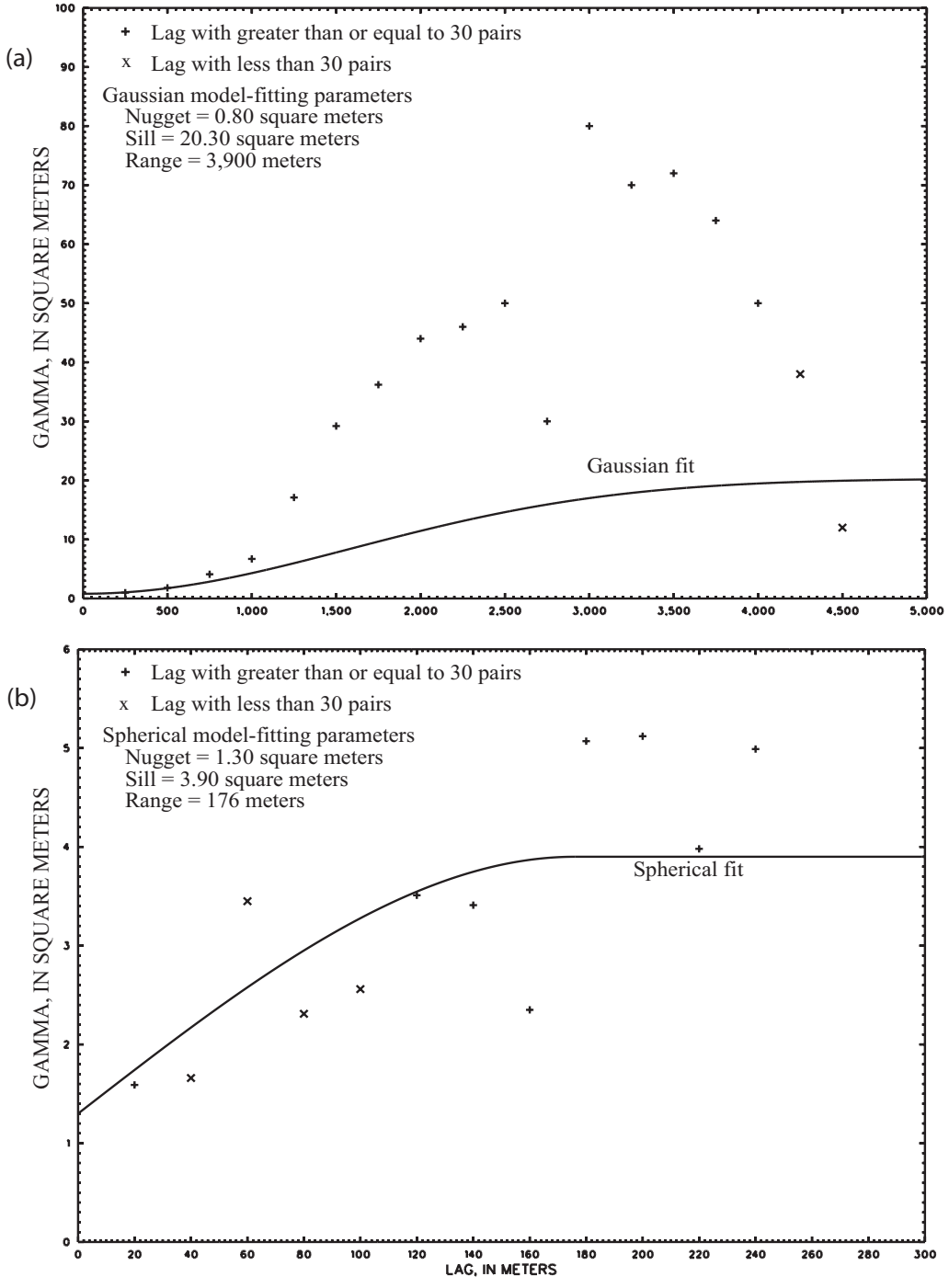

Figure 6-2. Variograms for the top elevation (a) and thickness (b) of surficial sediments in the model domain of the Waste Area Group 7 numerical simulator, Idaho National Engineering and Environmental Laboratory, Idaho.

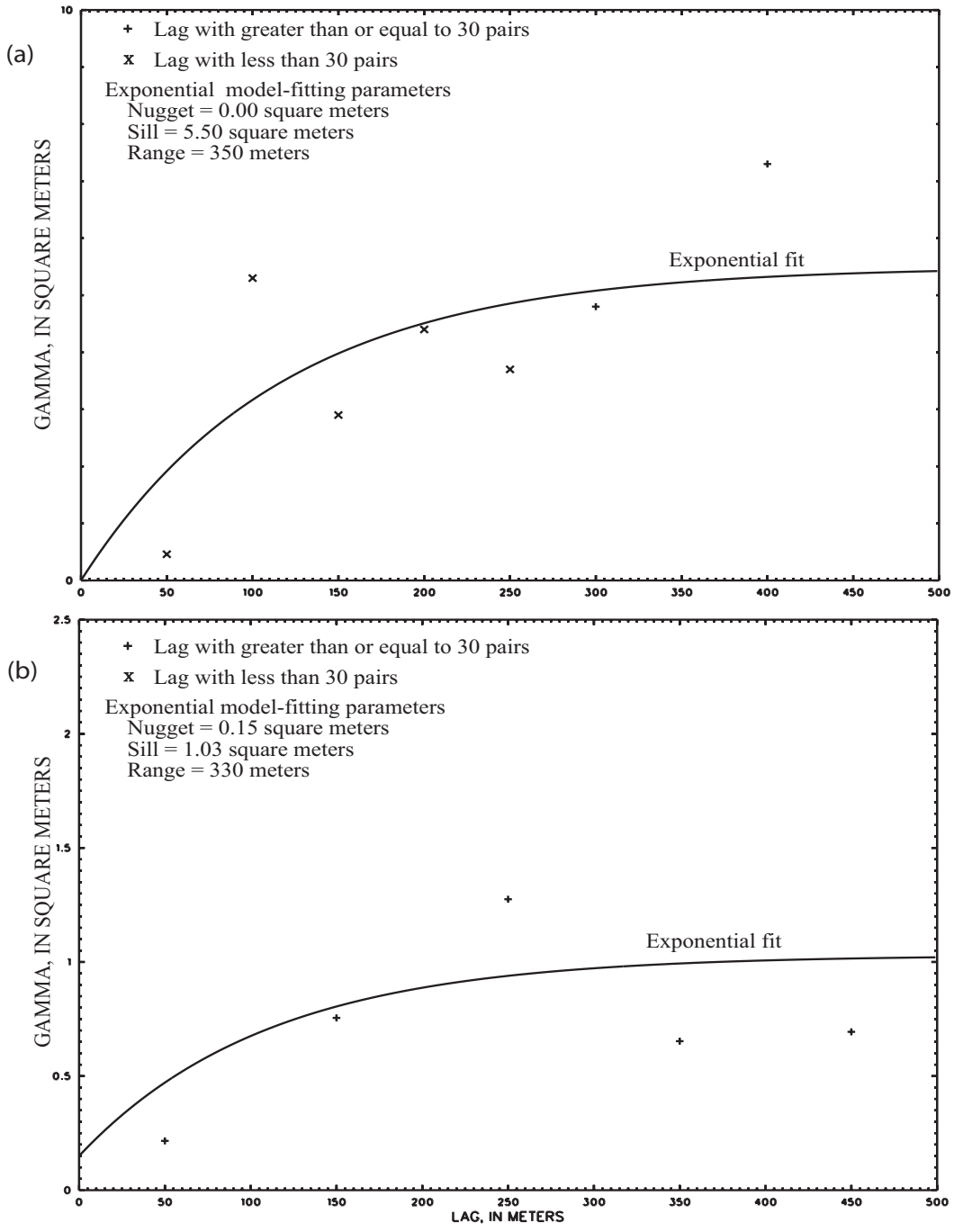

Figure 6-3. Variograms for the top elevation (a) and thickness (b) of the A-B interbed in the model domain of the Waste Area Group 7 numerical simulator, Idaho National Engineering and Environmental Laboratory, Idaho.

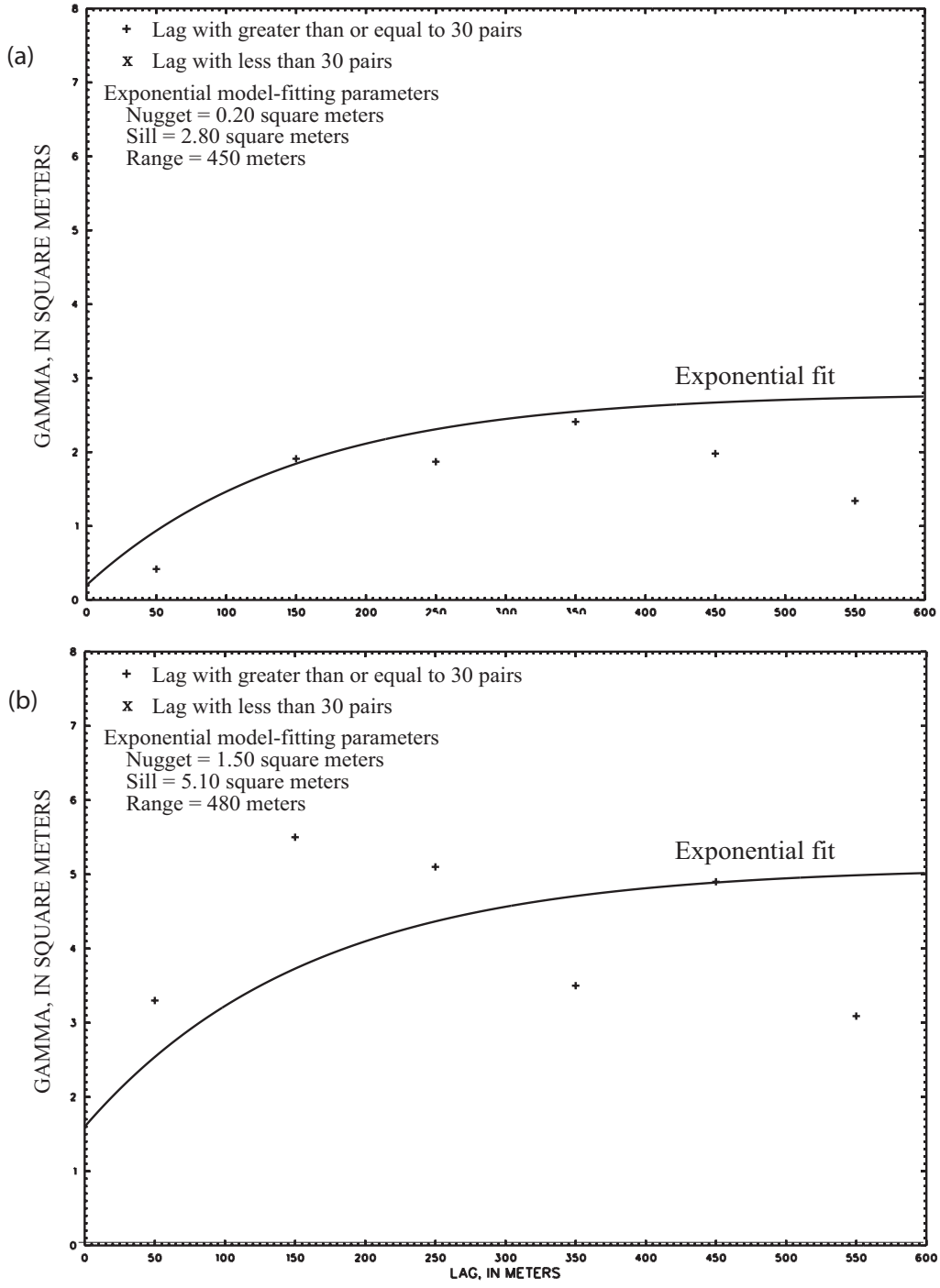

Figure 6-4. Variograms for the top elevation (a) and thickness (b) of the B-C interbed in the model domain of the Waste Area Group 7 numerical simulator, Idaho National Engineering and Environmental Laboratory, Idaho.

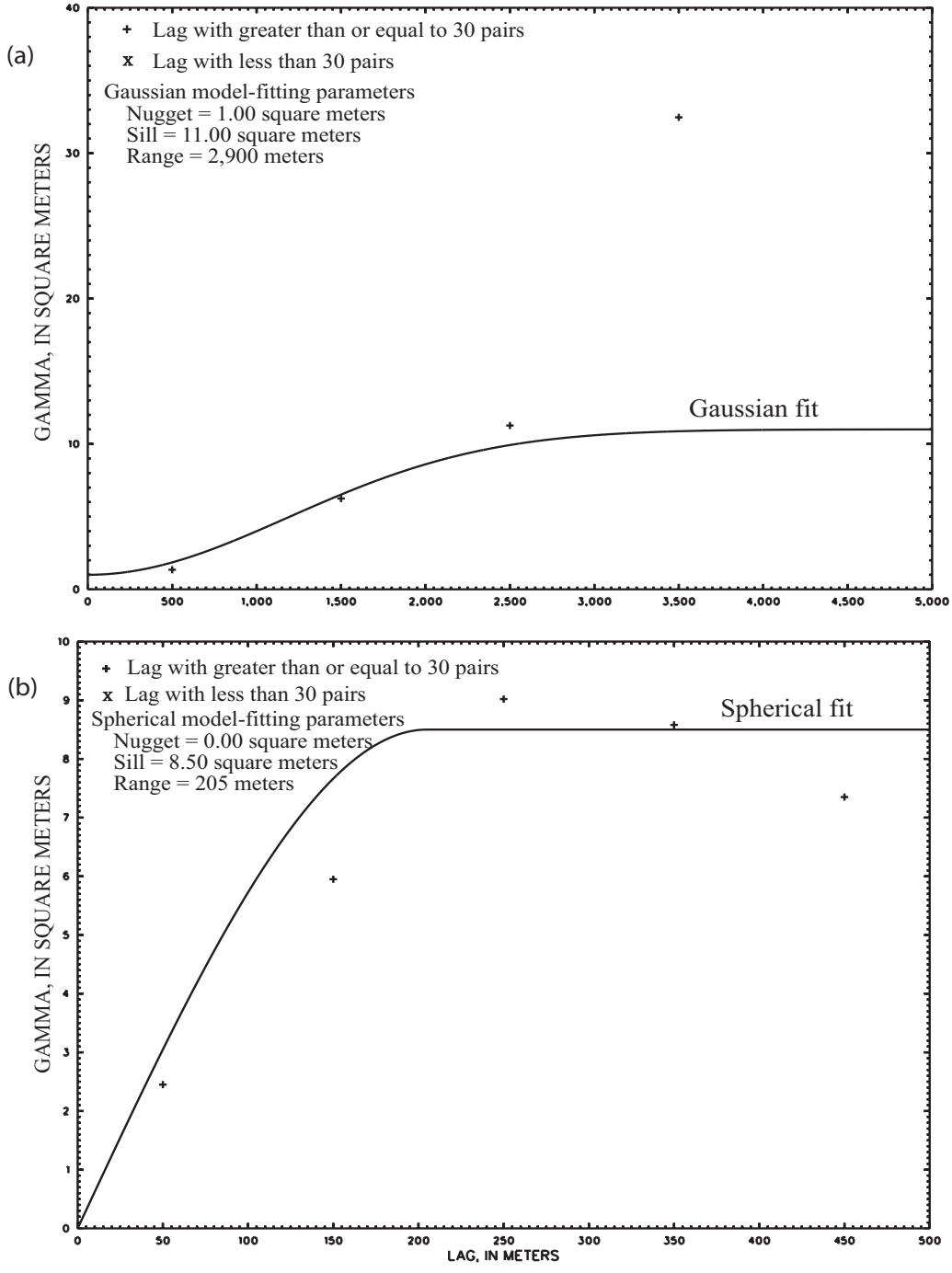

Figure 6-5. Variograms for the top elevation (a) and thickness (b) of the C-D interbed in the model domain of the Waste Area Group 7 numerical simulator, Idaho National Engineering and Environmental Laboratory, Idaho.

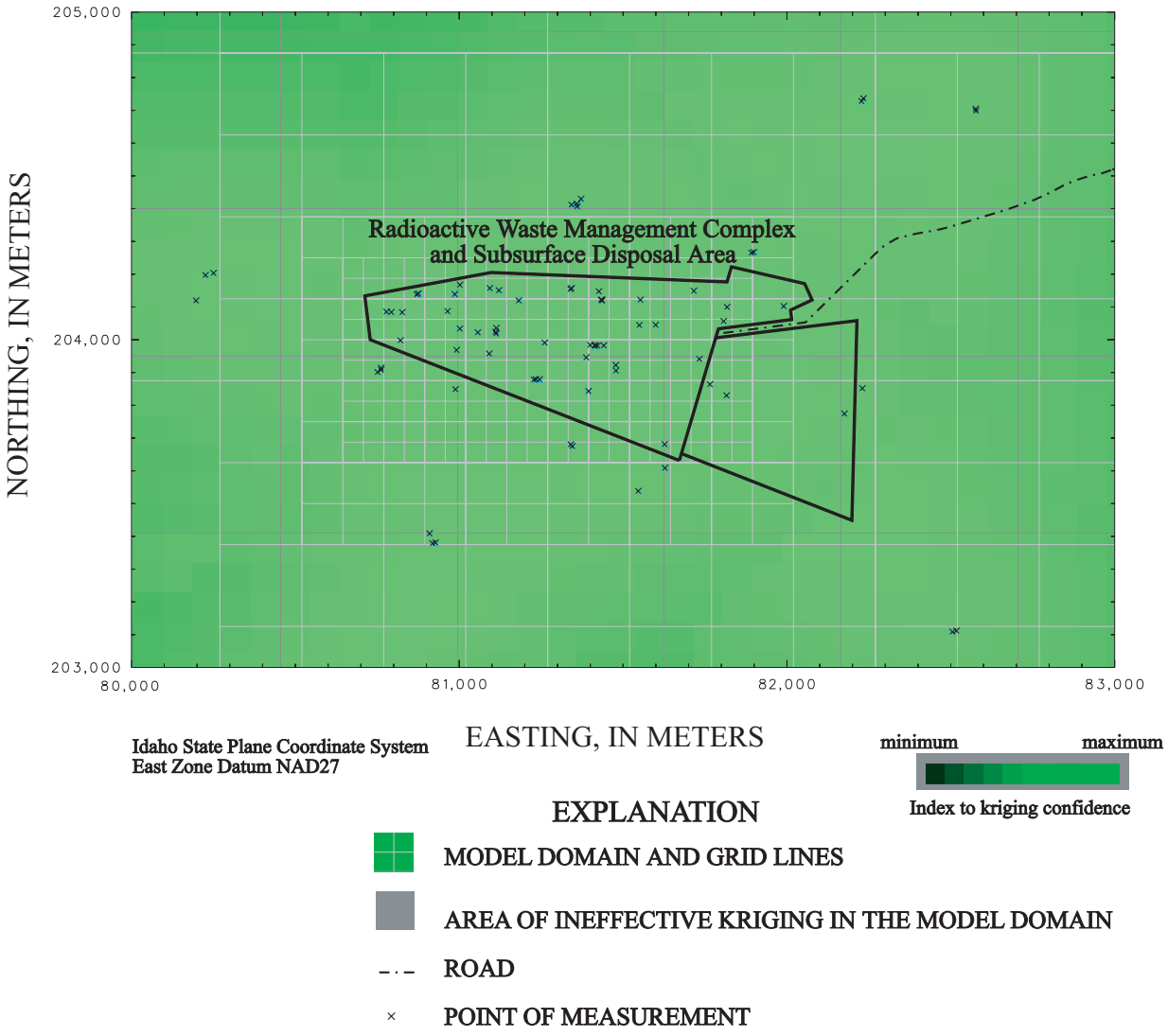

Figure 6-6. Discretization, measured points, and relative confidence in kriged estimates for the top elevation of the surficial sediments in the vicinity of the Radioactive Waste Management Complex, Idaho National Engineering and Environmental Laboratory, Idaho.

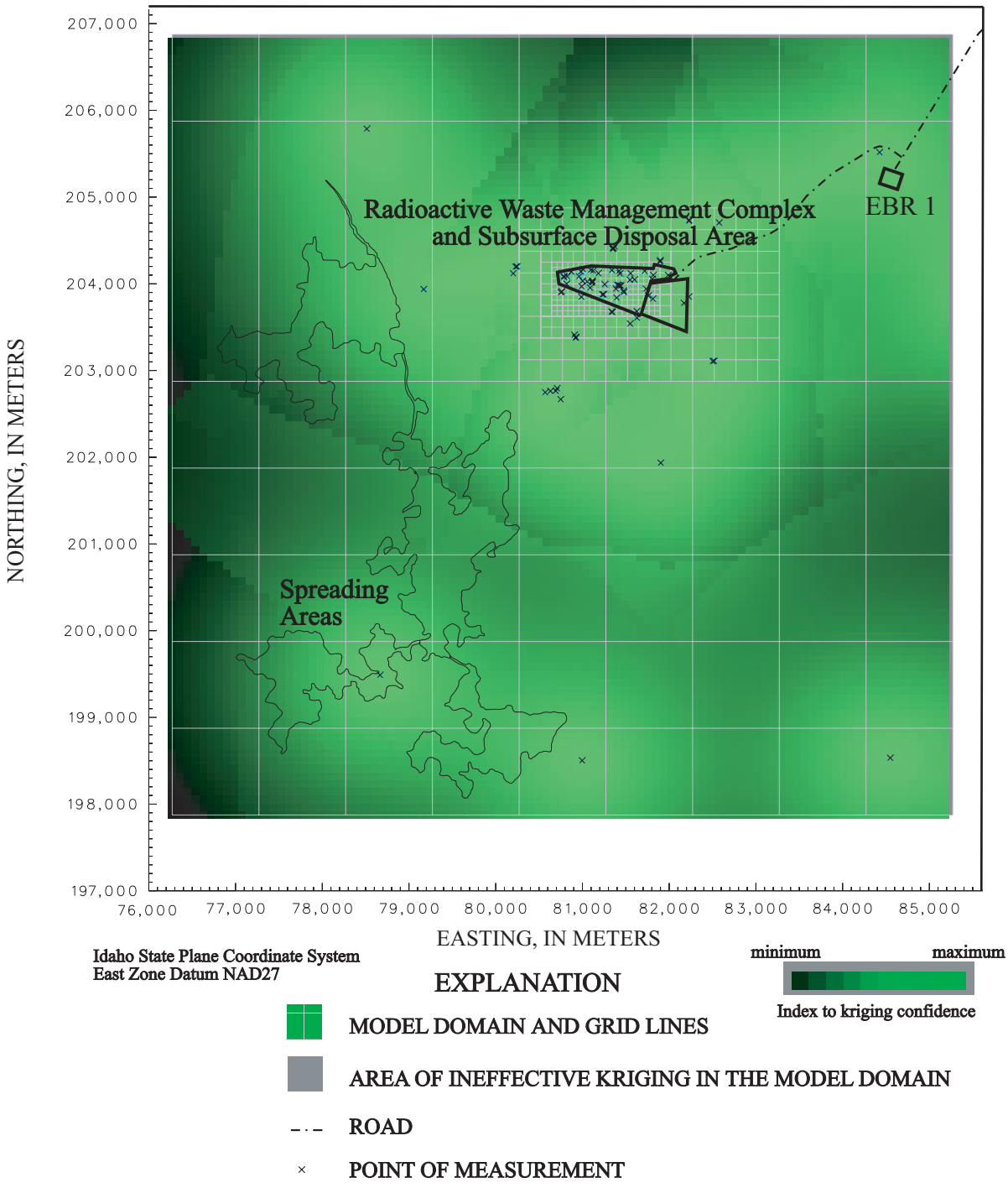

Figure 6-7. Discretization, measured points, and relative confidence in kriged estimates for the top elevation of the surficial sediments in the Waste Area Group 7 model domain, Radioactive Waste Management Complex, Idaho National Engineering and Environmental Laboratory, Idaho.

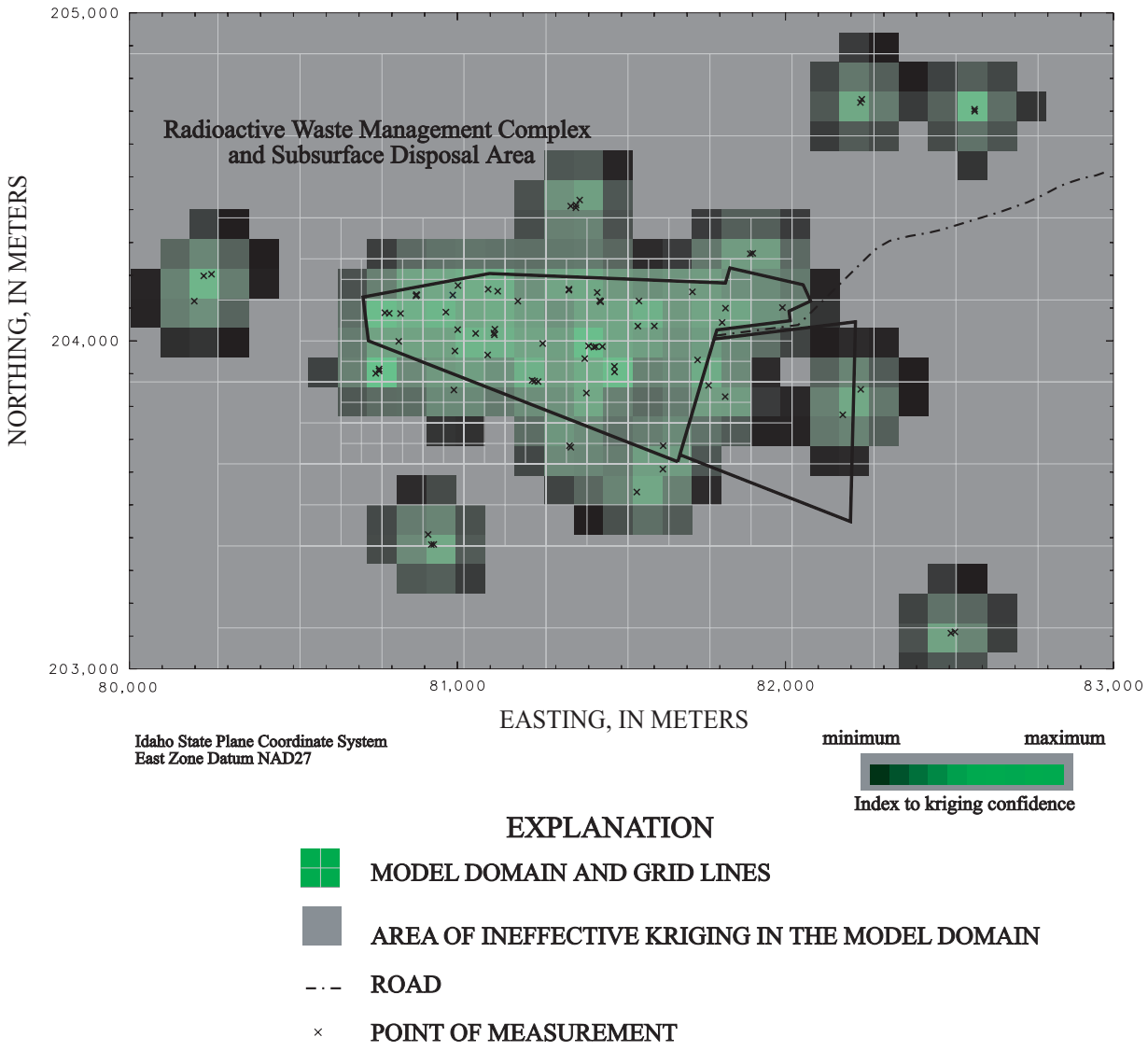

Figure 6-8. Discretization, measured points, and relative confidence in kriged estimates for the thickness of the surficial sediments in vicinity of the Radioactive Waste Management Complex, Idaho National Engineering and Environmental Laboratory, Idaho.

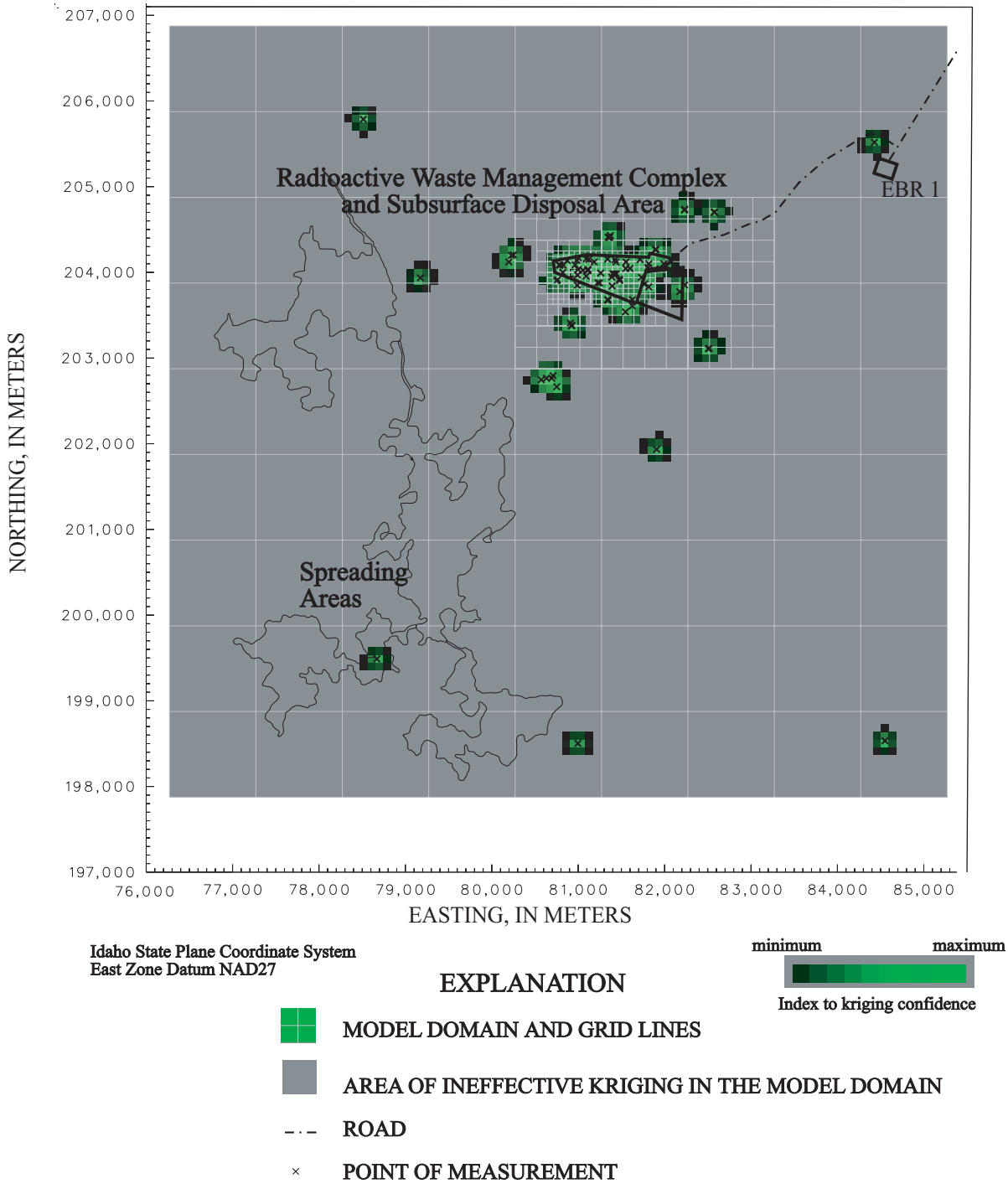

Figure 6-9. Discretization, measured points, and relative confidence in kriged estimates for the thickness of the surficial sediments in the Waste Area Group 7 model domain, Radioactive Waste Management Complex, Idaho National Engineering and Environmental Laboratory, Idaho.

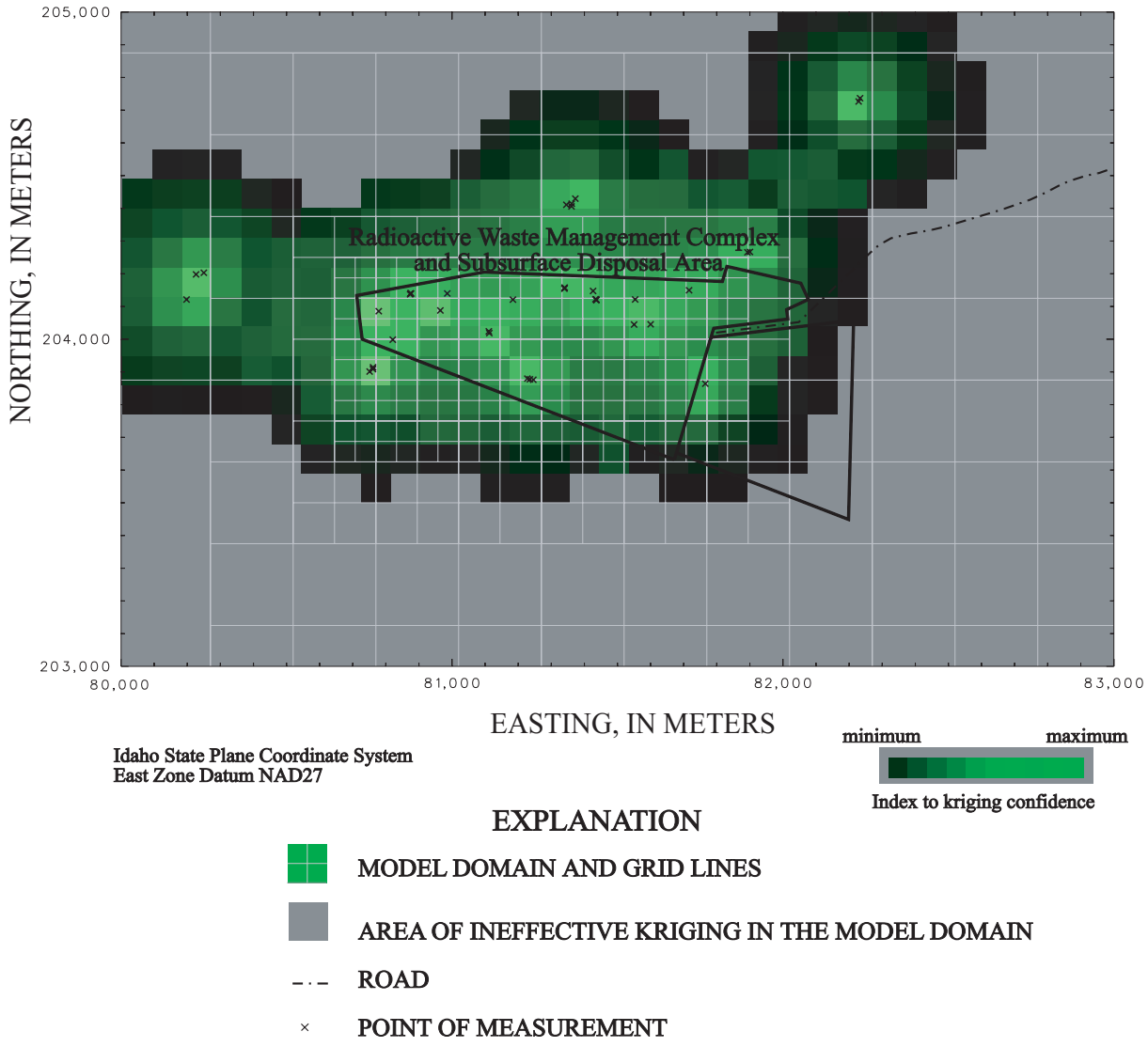

Figure 6-10. Discretization, measured points, and relative confidence in kriged estimates for the top elevation of the A-B sedimentary interbed in the vicinity of the Radioactive Waste Management Complex, Idaho National Engineering and Environmental Laboratory, Idaho.

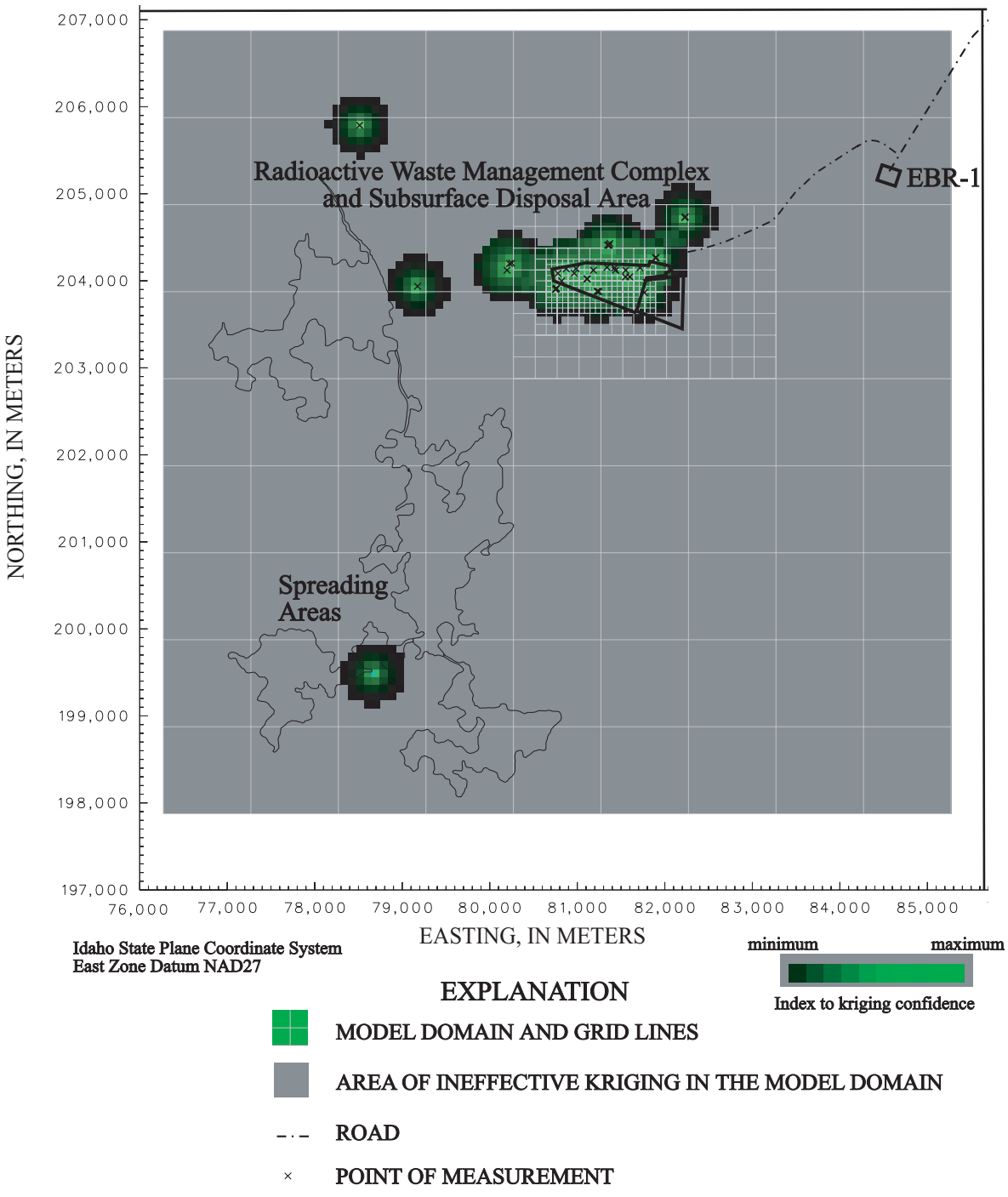

Figure 6-11. Discretization, measured points, and relative confidence in kriged estimates for the top elevation of the A-B sedimentary interbed in the Waste Area Group 7 model domain, Radioactive Waste Management Complex, Idaho National Engineering and Environmental Laboratory, Idaho.

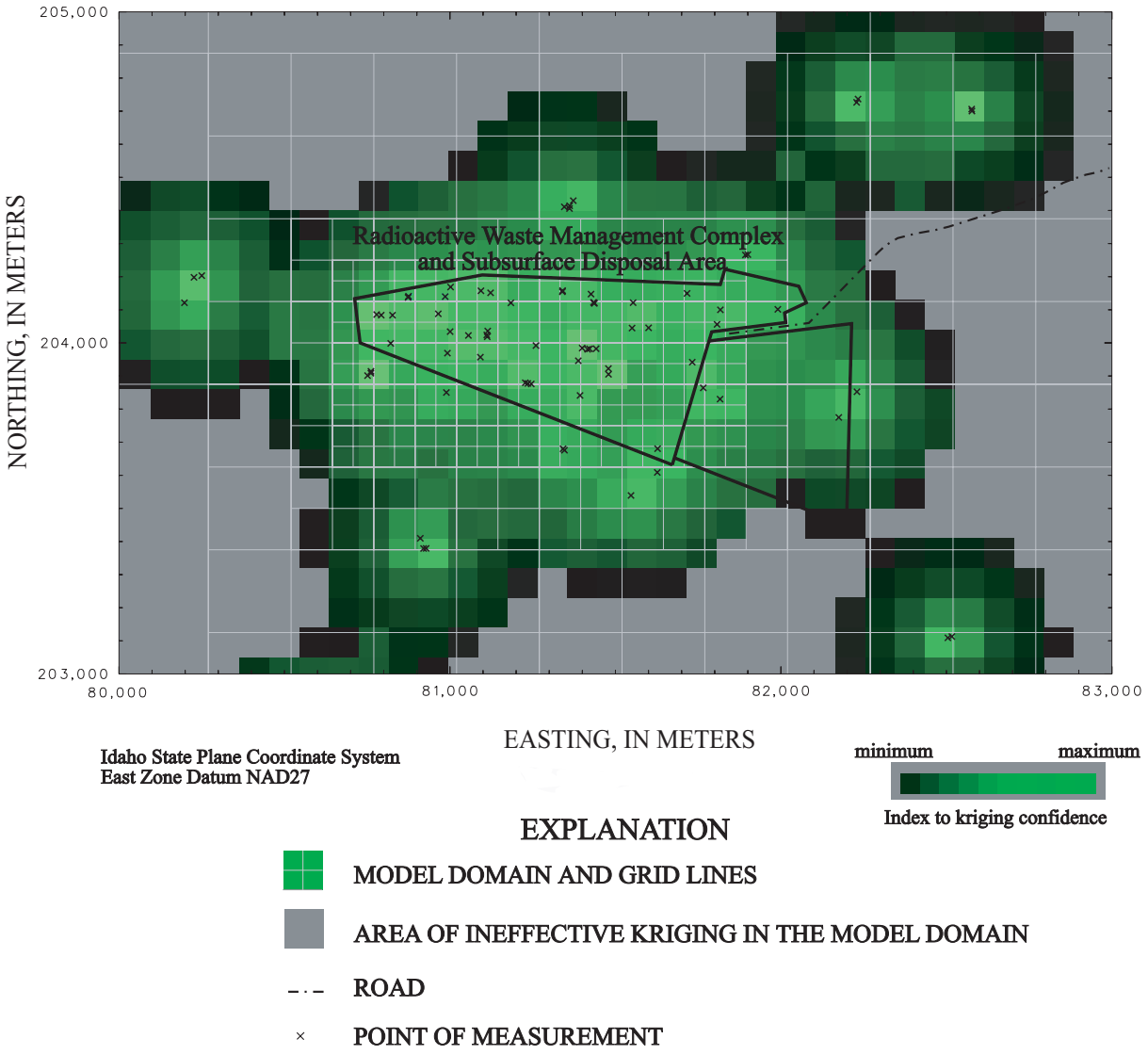

Figure 6-12. Discretization, measured points, and relative confidence in kriged estimates for the thickness of the A-B sedimentary interbed in the vicinity of the Radioactive Waste Management Complex, Idaho National Engineering and Environmental Laboratory, Idaho.

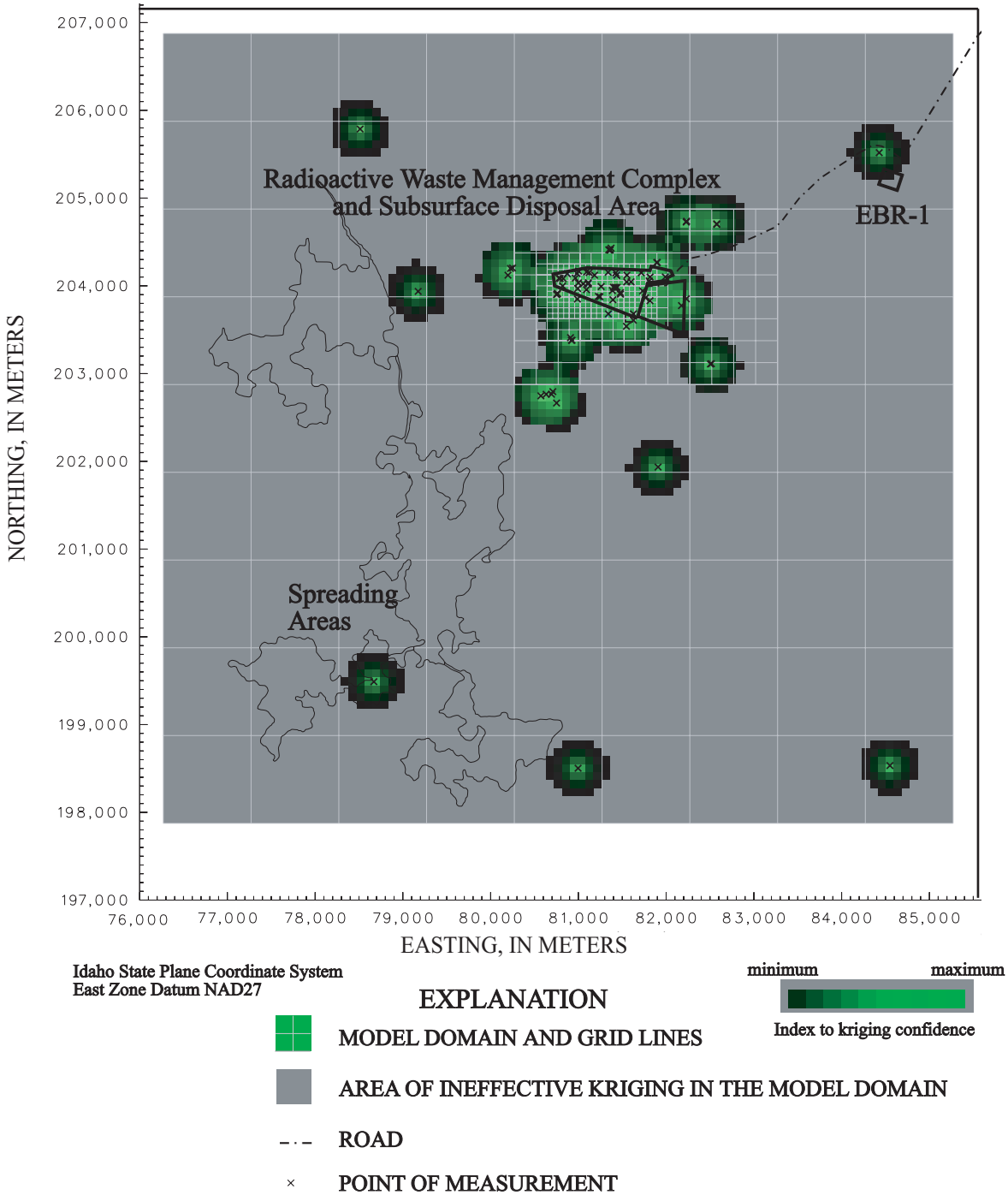

Figure 6-13. Discretization, measured points, and relative confidence in kriged estimates for the thickness of the A-B sedimentary interbed in the Waste Area Group 7 model domain, Radioactive Waste Management Complex, Idaho National Engineering and Environmental Laboratory, Idaho.

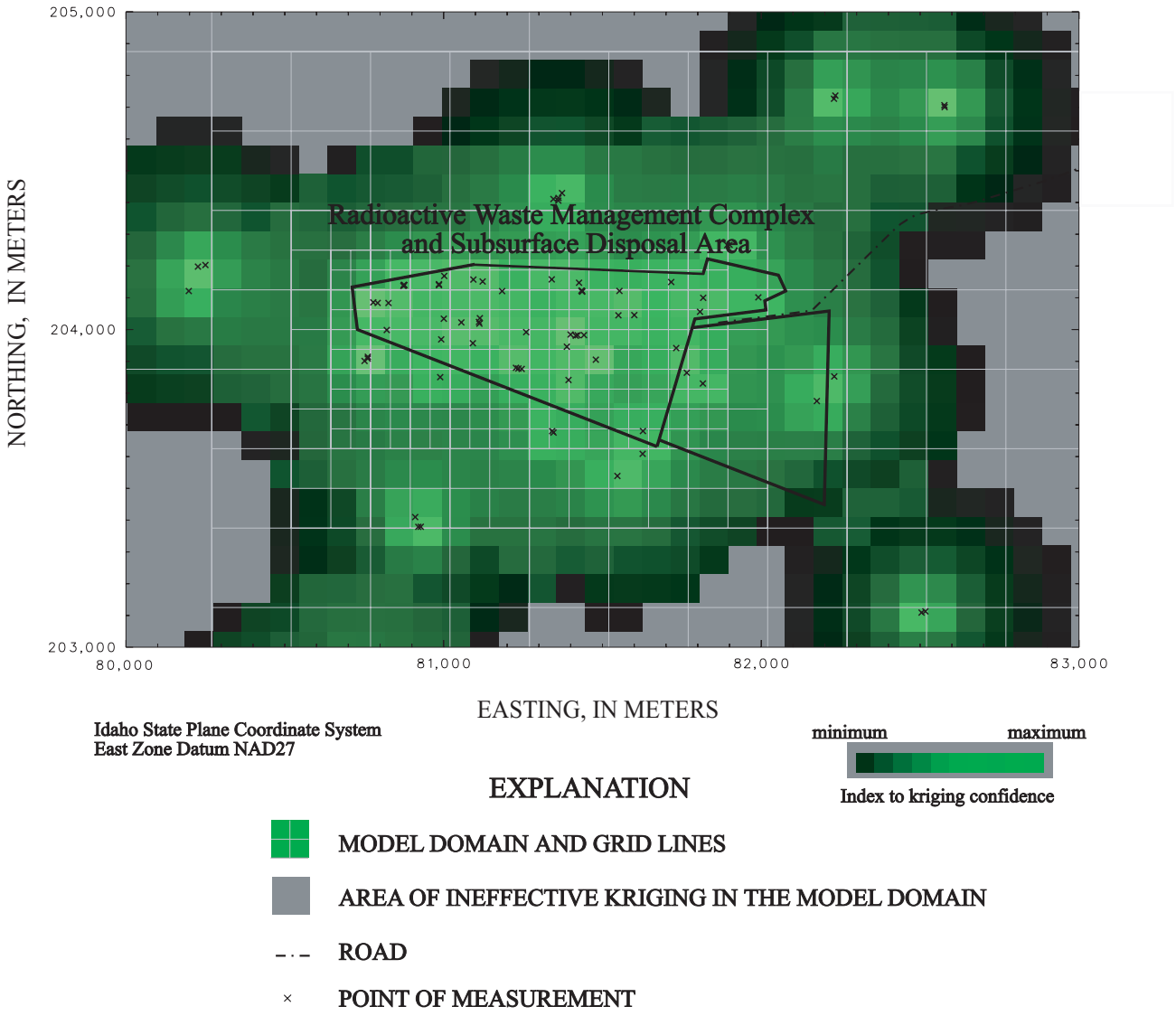

Figure 6-14. Discretization, measured points, and relative confidence in kriged estimates for the top elevation of the B-C sedimentary interbed in the vicinity of the Radioactive Waste Management Complex, Idaho National Engineering and Environmental Laboratory, Idaho.

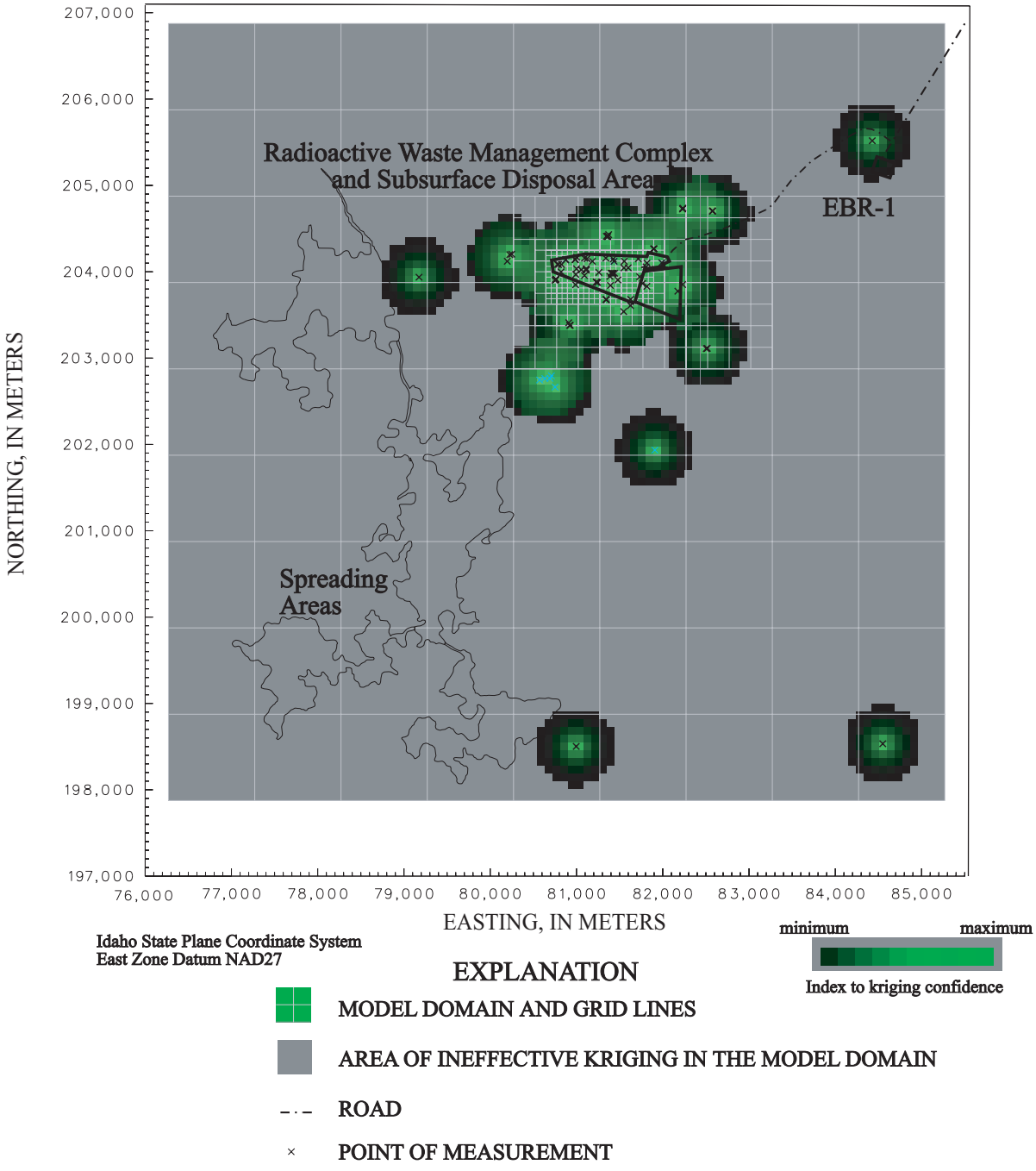

Figure 6-15. Discretization, measured points, and relative confidence in kriged estimates for the top elevation of the B-C sedimentary interbed in the Waste Area Group 7 model domain, Radioactive Waste Management Complex, Idaho National Engineering and Environmental Laboratory, Idaho.

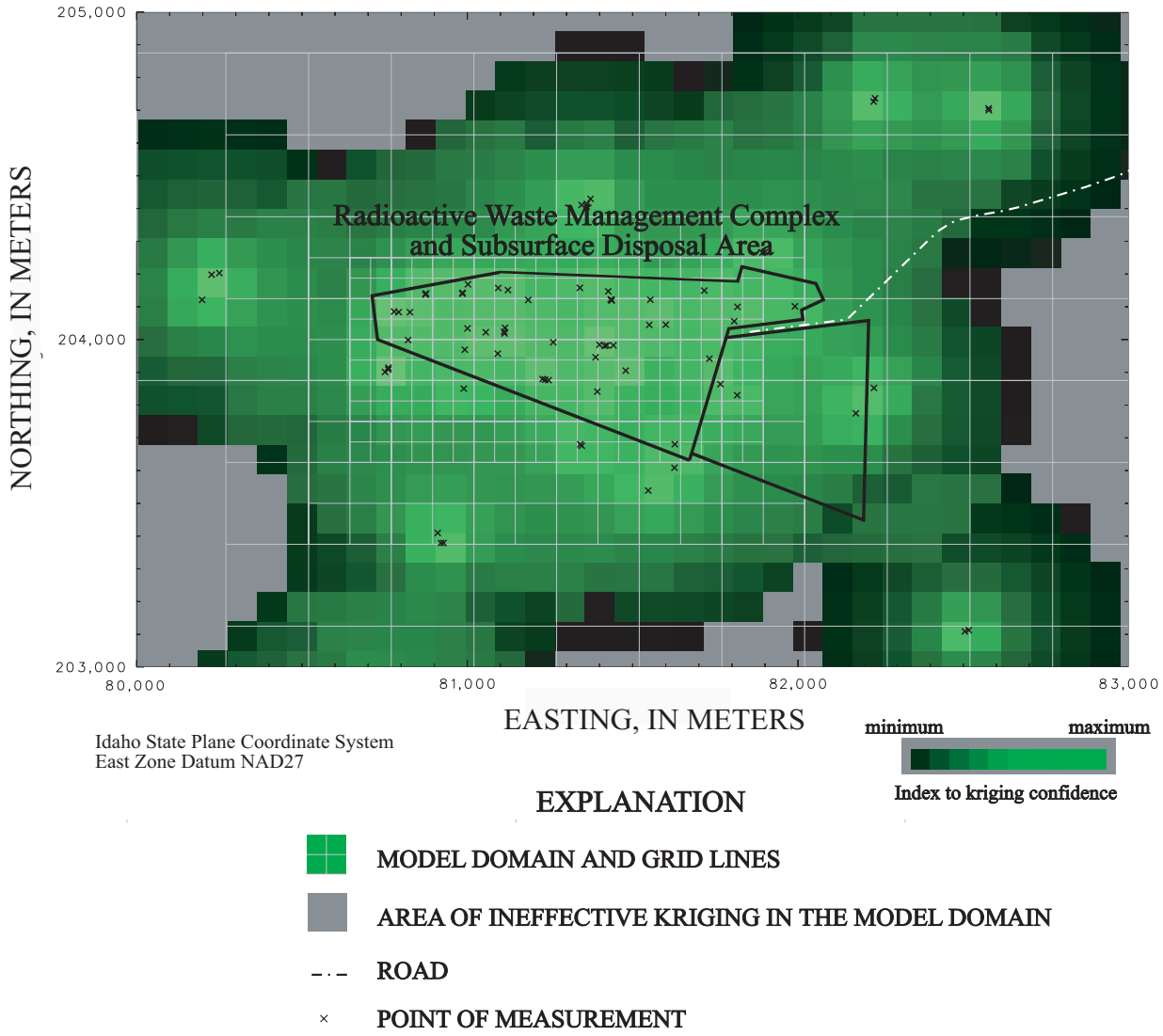

Figure 6-16. Discretization, measured points, and relative confidence in kriged estimates for the thickness of the B-C sedimentary interbed in the vicinity of the Radioactive Waste Management Complex, Idaho National Engineering and Environmental Laboratory, Idaho.

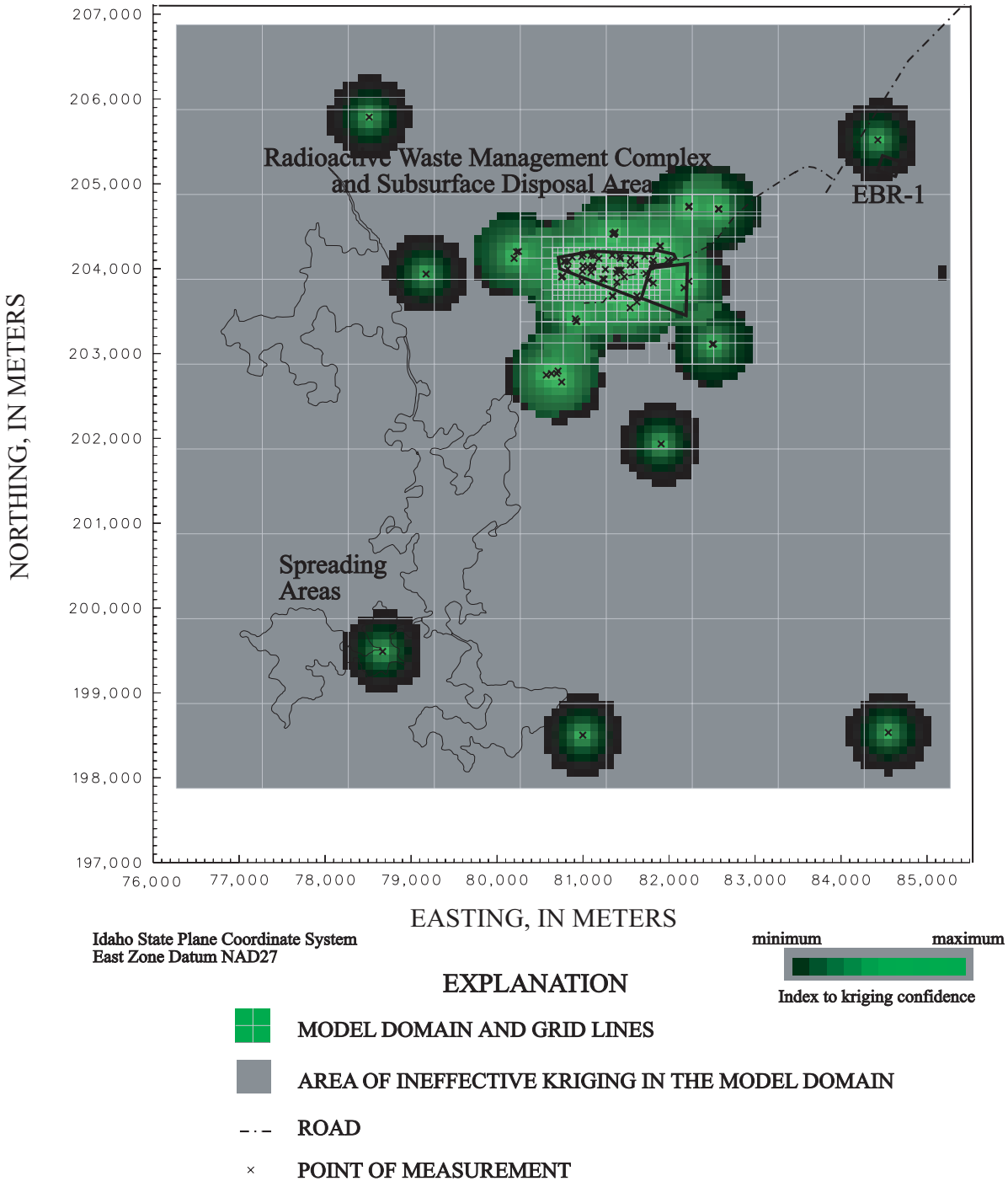

Figure 6-17. Discretization, measured points, and relative confidence in kriged estimates for the thickness of the B-C sedimentary interbed in the Waste Area Group 7 model domain, Radioactive Waste Management Complex, Idaho National Engineering and Environmental Laboratory, Idaho.

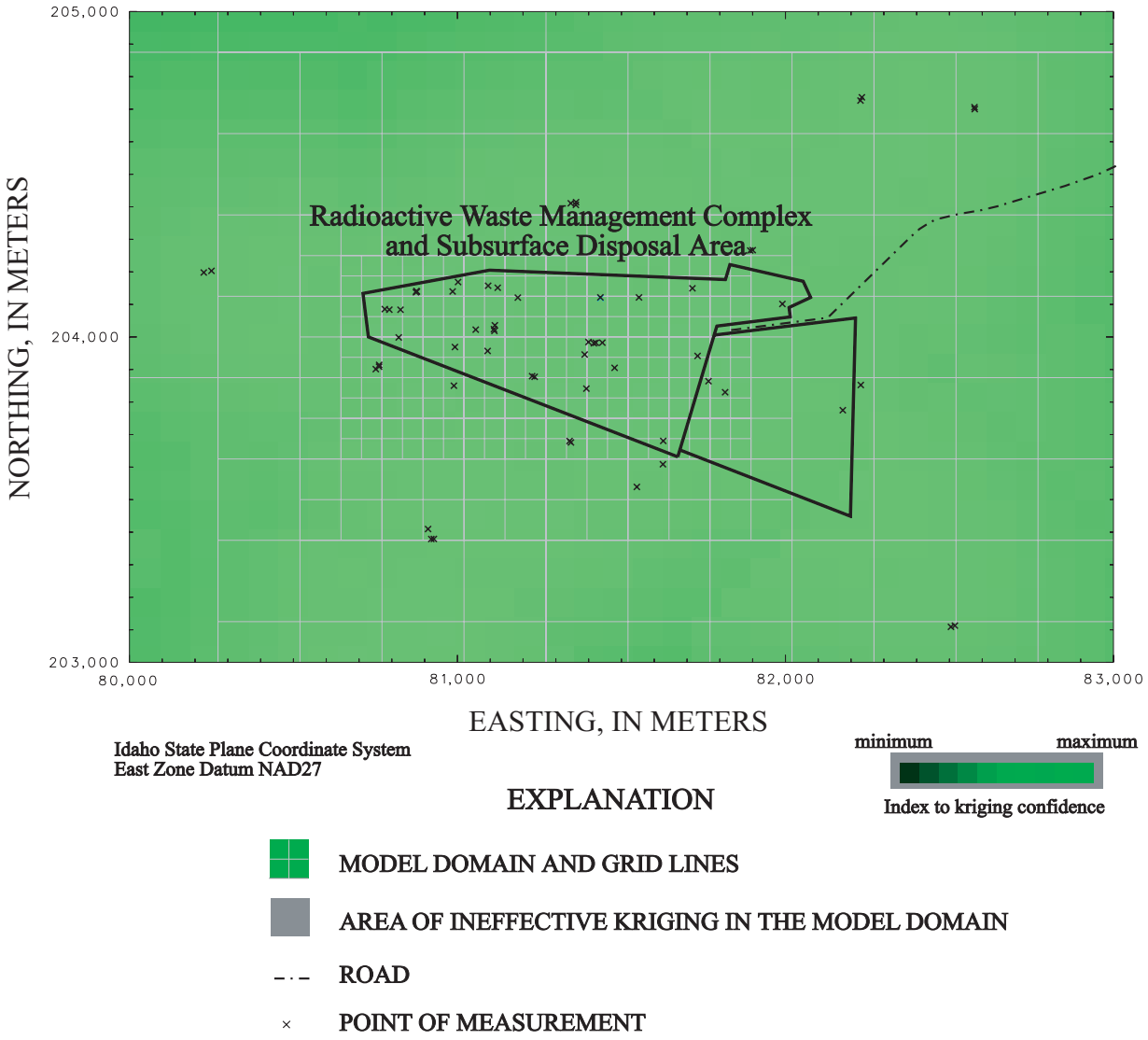

Figure 6-18. Discretization, measured points, and relative confidence in kriged estimates for the top elevation of the C-D sedimentary interbed in the vicinity of the Radioactive Waste Management Complex, Idaho National Engineering and Environmental Laboratory, Idaho.

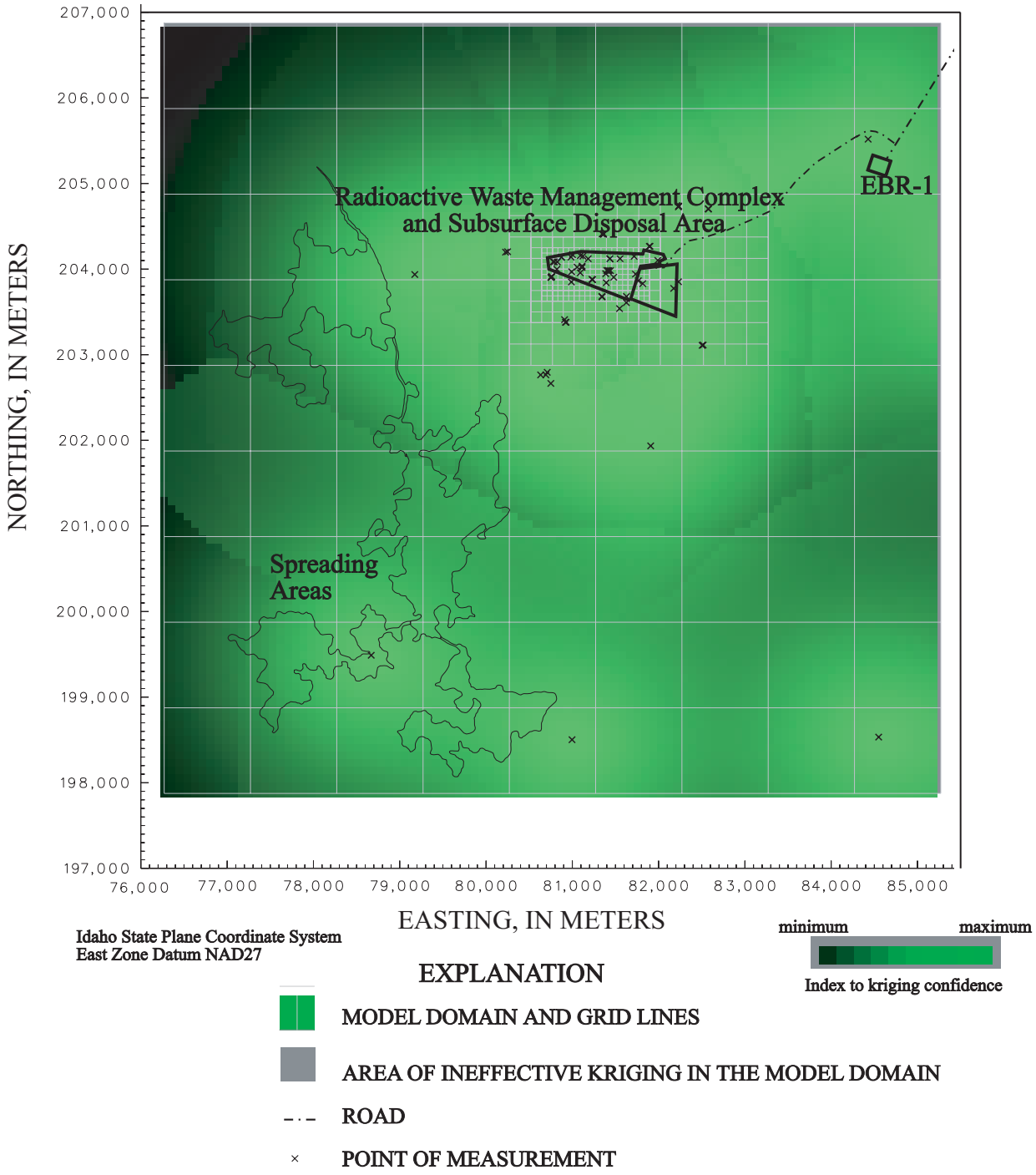

Figure 6-19. Discretization, measured points, and relative confidence in kriged estimates for the top elevation of the C-D sedimentary interbed in the Waste Area Group 7 model domain, Radioactive Waste Management Complex, Idaho National Engineering and Environmental Laboratory, Idaho.

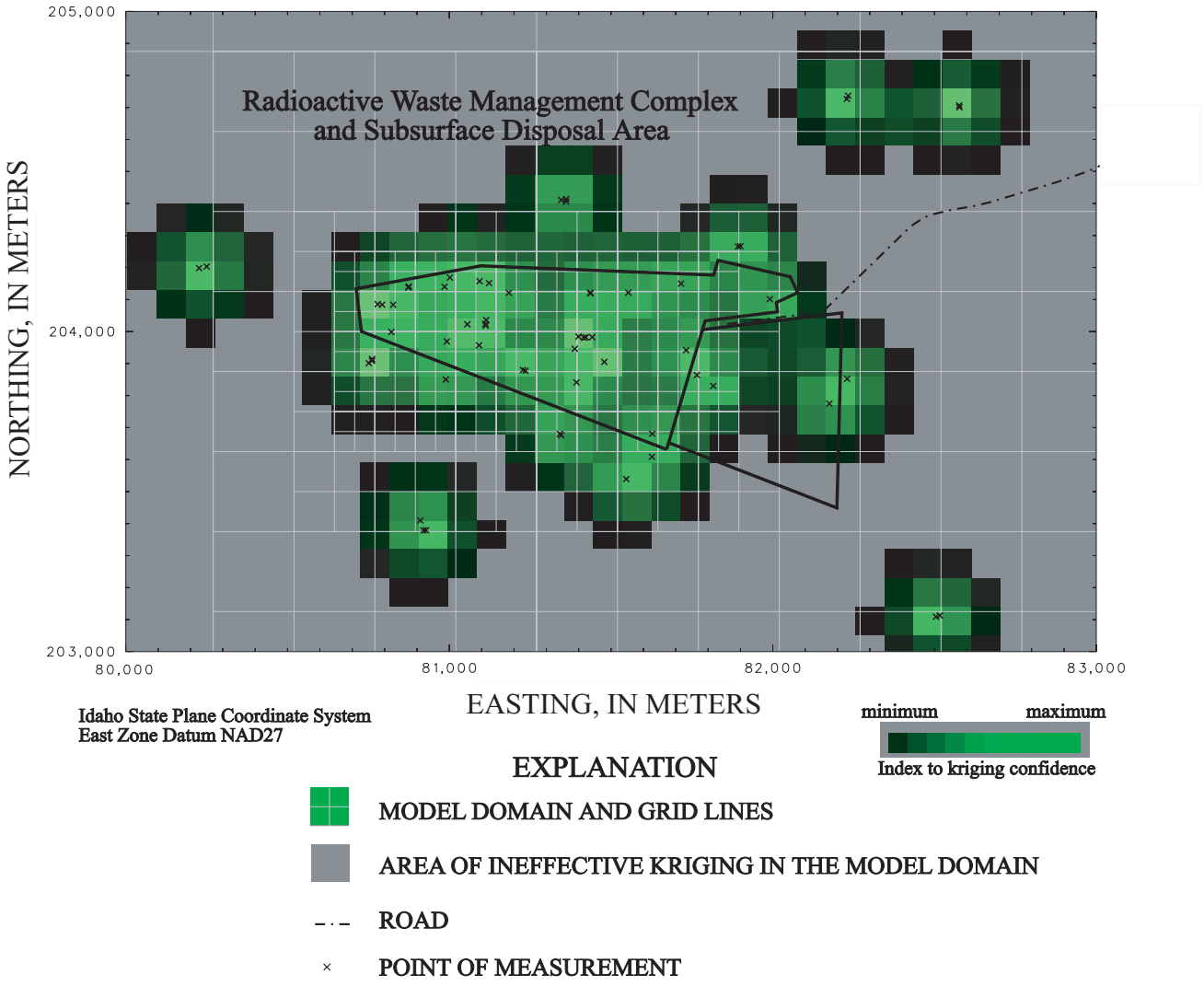

Figure 6-20. Discretization, measured points, and relative confidence in kriged estimates for the thickness of the C-D sedimentary interbed in the vicinity of the Radioactive Waste Management Complex, Idaho National Engineering and Environmental Laboratory, Idaho.

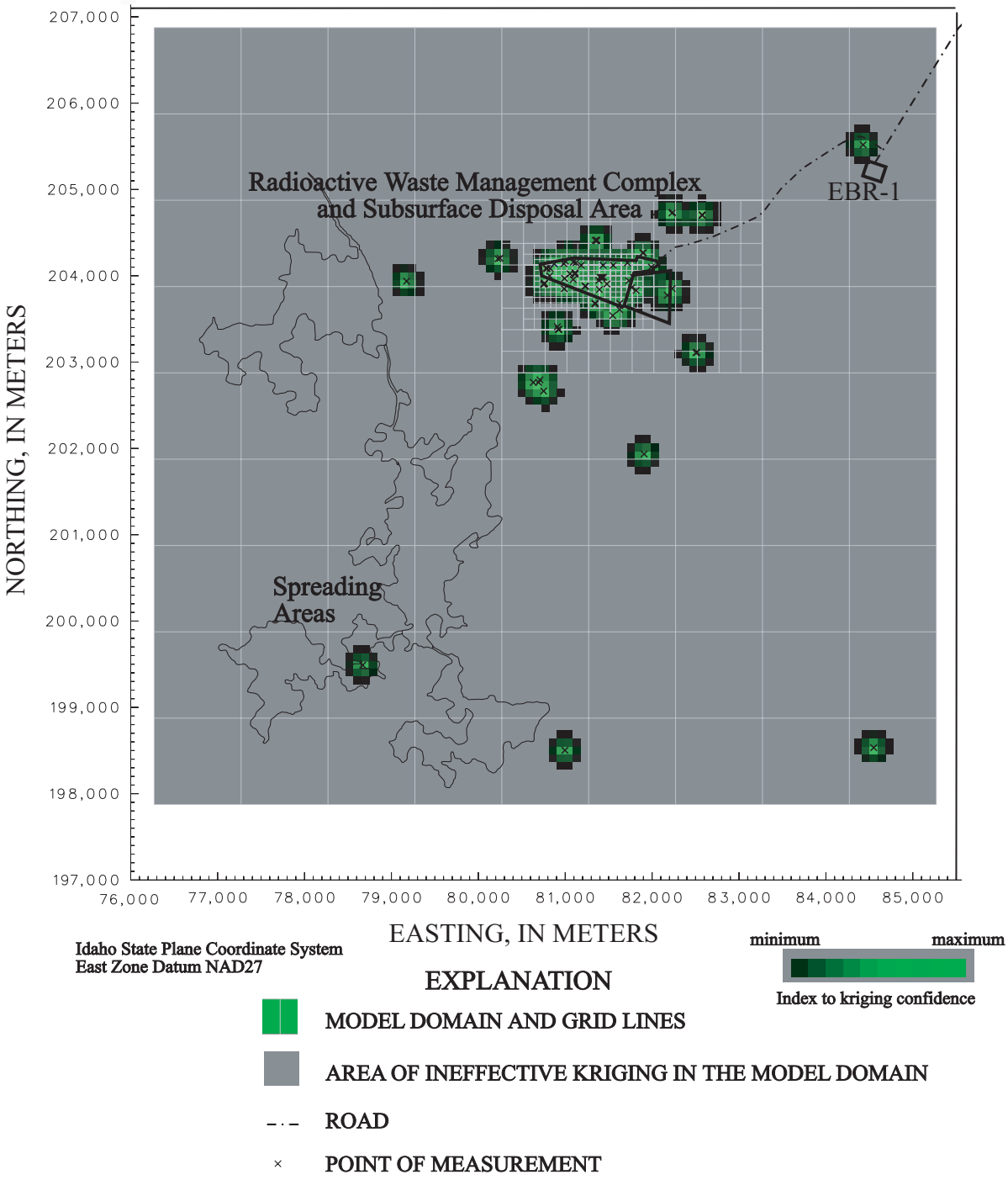

Figure 6-21. Discretization, measured points, and relative confidence in kriged estimates for the thickness of the C-D sedimentary interbed in the Waste Area Group 7 model domain, Radioactive Waste Management Complex, Idaho National Engineering and Environmental Laboratory, Idaho.

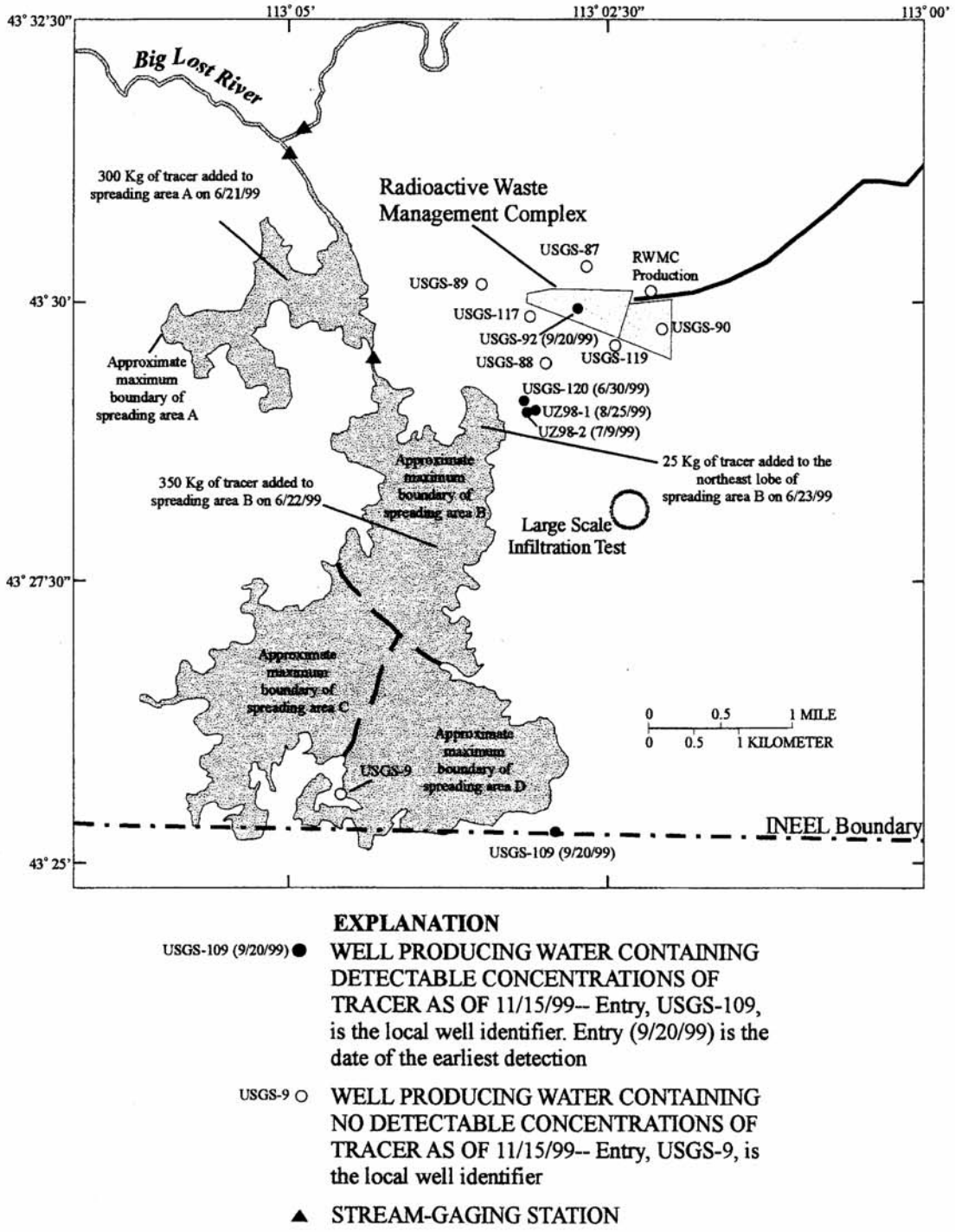

Figure 6-22. Location of spreading areas, Radioactive Waste Management Complex, and selected boreholes used in the 1999 tracer monitoring program, Idaho National Engineering and Environmental Laboratory, Idaho.

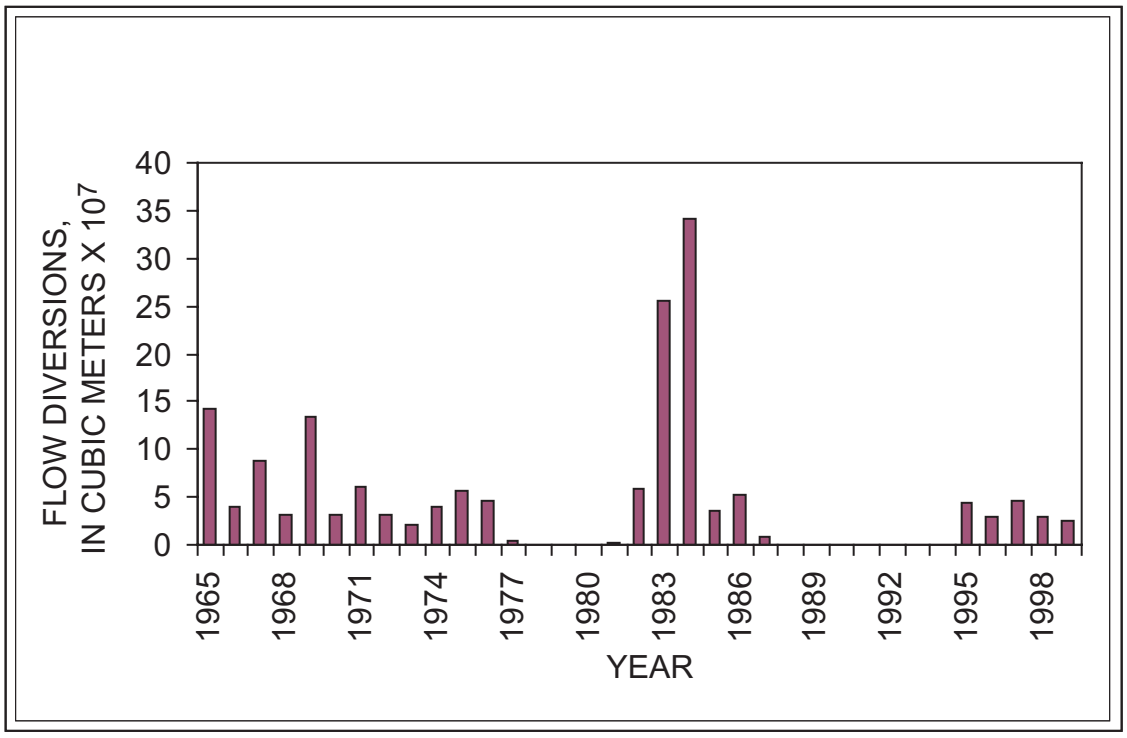

Figure 6-23. Flow diversions to the spreading areas from January 1965 to January 2000, Idaho National Engineering and Environmental Laboratory, Idaho.

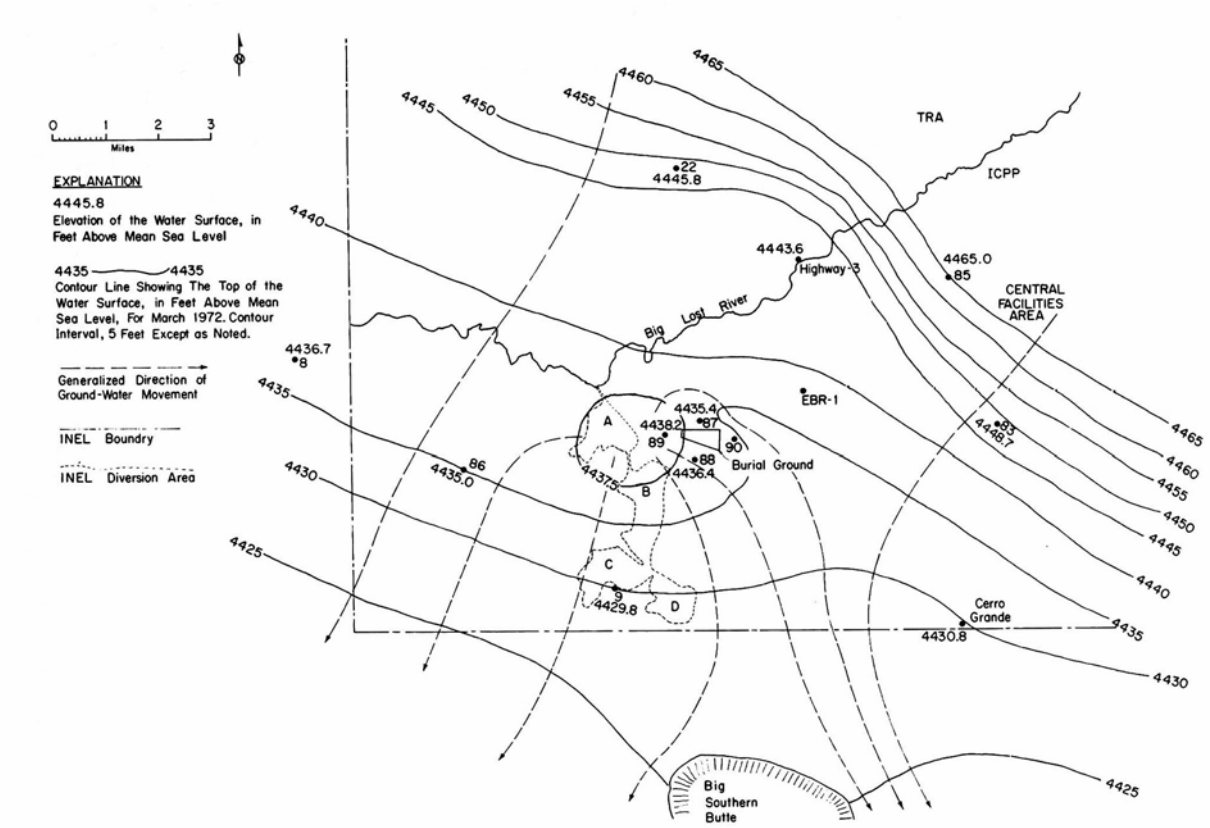

Figure 6-24. Southwestern portion of the Idaho National Engineering and Environmental Laboratory showing contours on the water table of the Snake River Plain aquifer and inferred directions of ground-water movement, March 1972 (modified from Barraclough and others, 1976, fig. 33).

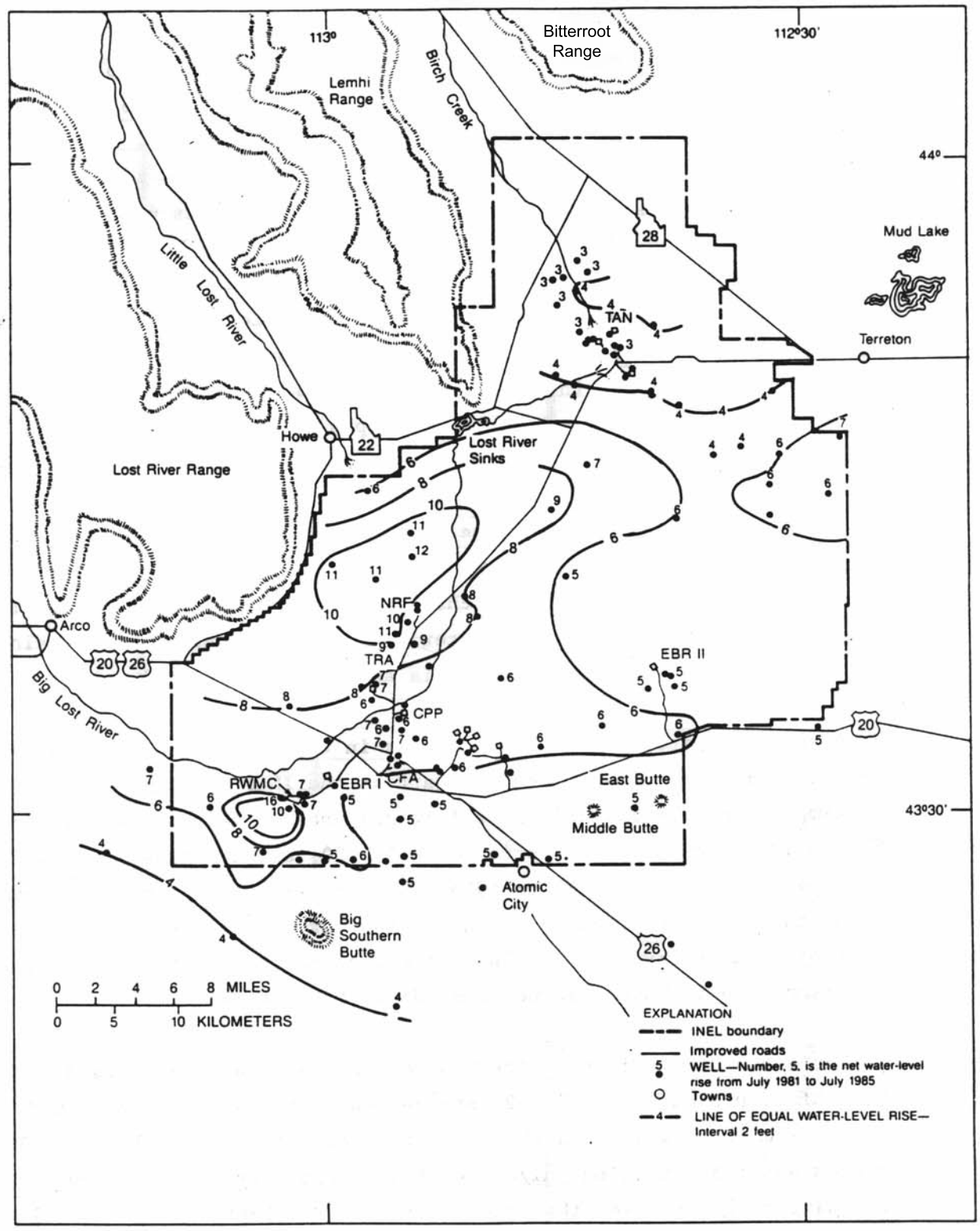

Figure 6-25. Generalized net increase of the regional water table July 1981 to July 1985 (from Pittman and others, 1988, fig. 10), Snake River Plain aquifer, Idaho National Engineering and Environmental Laboratory, Idaho.

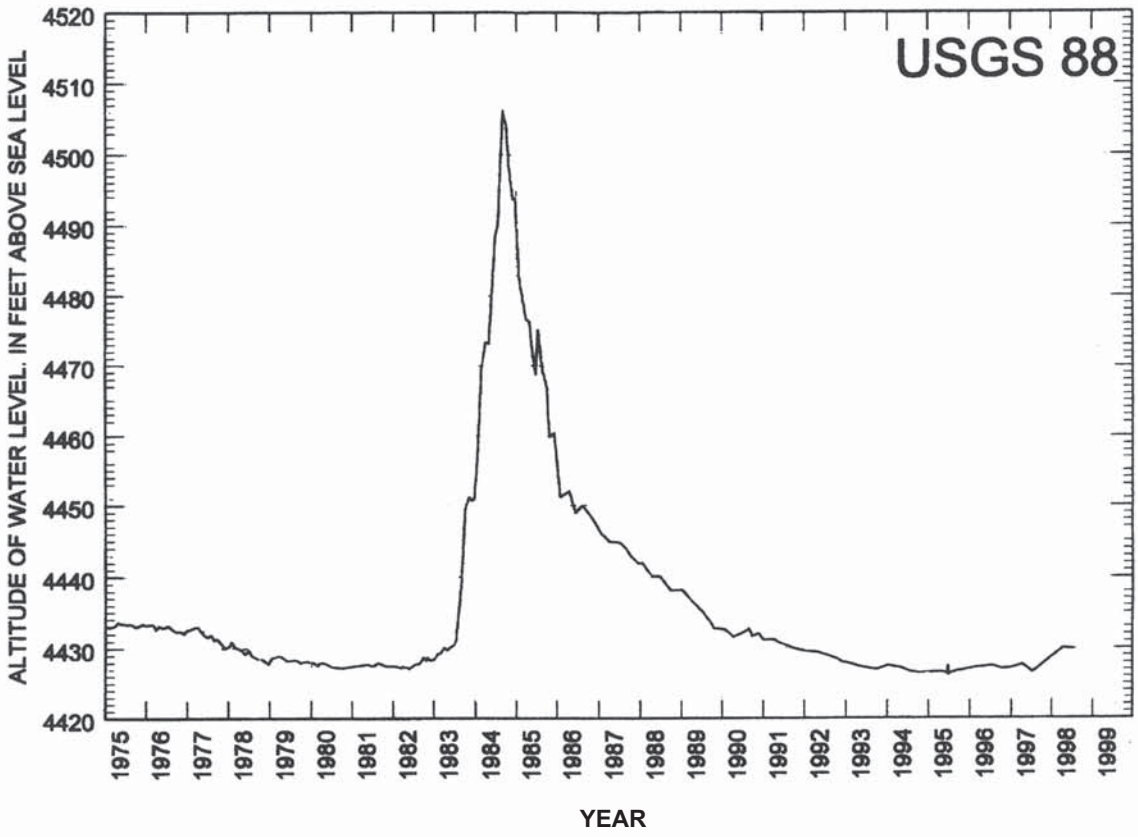

Figure 6-26. Water levels in borehole USGS 88 from January 1975 to July 1998, Idaho National Engineering and Environmental Laboratory, Idaho.